Development of experimental gas electron diffraction technique

Stuart A. Hayes

A thesis presented for the degree of
Doctor of Philosophy
at the University of Edinburgh
2008

Declaration

This thesis has not been previously submitted, in whole or in part, for any degree at this or any other university. The work is original and my own, carried out under the supervision of Prof. David W. H. Rankin; where this is not so, credit has been duly given.

Stuart A. Hayes

Acknowledgements

First of all I would like to thank David Rankin for the opportunity to study in his group and for an interesting project that provided a great balance of practical and theoretical work. I would also like to thank all the members of the Rankin group and those whom I have shared the office with as they have especially made the time enjoyable and have all helped me with my work in some way or another.

There are a number of people who have contributed directly to the work described in this thesis and therefore deserve special mention. As I began my PhD Sarah Masters taught me all of the basics of how to perform refinements and run calculations using the Gaussian software. Also in my first year, Thomas Foerster spent a lot of time reassembling the machine and chasing up plumbers etc. Heather Robertson let me help collect data on the old GED machine and, probably without realising, taught me a lot of practical things that were essential for making progress with the SSED apparatus. Derek Wann has encouraged me to get things written, has helped a lot proof reading this thesis and helping to write journal articles. He has also often helped me to focus by listening to my thoughts on the SSED apparatus. Richard Mawhorter provided a great deal of advice and his help was especially important in the design of the camera mount and the beam stop. Stuart Mains and Davy Paden in the mechanical workshops also deserve a mention as they were the ones who made the various components we designed in order to install the CCD camera. Finally, I would like to thank Malcolm Fluendy for sharing his concerns and memories of working on the SSED apparatus.

Abstract

A state-of-the-art gas electron diffraction (GED) apparatus has been reassembled in the school of chemistry at the University of Edinburgh. This combines molecular-beam and telefocus-electron-gun technologies and the alignment of the electron beam produced by the latter has been discussed. A new custom-made CCD detector has also been installed and electron diffraction patterns for a few small molecules have been recorded. In analogy to the rotating sector in a conventional GED apparatus, the new camera contains an optical filter and a procedure for its calibration is outlined and followed step by step to produce an estimate of the filter transmittance. The data have been shown to be of less than ideal quality and the probable root of the problem is discussed.

GED refinements of two pairs of compounds (*arachno*-6,9-decaboranes, and a covalent sulfonate and thiosulfonate) are presented, using data collected with the conventional Edinburgh GED apparatus.

Contents

Chapter 1

Introduction to gas electron diffraction and background theory

1.1. The role of Gas Electron Diffraction (GED)

Molecular structure is of fundamental importance as its study propelled chemistry from being an intellectual curiosity to a rigorous science. Clearly topology defines both the chemical and physical properties of molecules and it is this side of molecular structure determination that has contributed most to the development of chemistry. However, molecular geometry also provides information about more subtle properties such as the relative strength of chemical bonds and can provide clues relating to the limitations of chemical understanding, usually expressed within the confines of simplified models such as those of Lewis[1] or Hückel.[2] The gas phase is ideal for studying such subtle effects, as the molecules are effectively independent of one another and any deviations in the molecular geometry from that predicted by theoretical methods can be attributed to either inadequacy in the theory adopted or poor experimental technique, without the complication of packing or solvation effects that are present in the solid and liquid phases.

Despite the fundamental importance of gas-phase structures, there are only two general experimental techniques available for their study, namely microwave spectroscopy and GED. Microwave spectroscopy is capable of yielding highly accurate structures, but it has two inherent problems that greatly limit its applicability. First, only three rotation constants can be determined, so a maximum of only three independent geometric parameters can be refined. By performing isotopic substitutions more rotational constants can be observed, but this is far from trivial experimentally, and can also be prohibitively expensive. Effects of isotopic substitution also reduce the accuracy of the technique. In contrast to microwave spectroscopy, seven to ten or more pieces of information are available in a typical GED experiment (observable as peaks in the radial-distribution curve, a Fourier transform of the intensity data – see **Section 1.4.3**). Therefore, the amount of structural information available from gas electron diffraction patterns is significantly greater than that obtained from a microwave spectrum. The second limitation

imposed on microwave spectroscopy, which does not impede GED, is that the molecule of interest must normally have a permanent dipole moment. A number of symmetric molecules that could be described by only three geometrical parameters are, therefore, not accessible. The combination of these two factors means that GED is the most powerful experimental technique for determining the gas-phase geometries of molecules.

1.2. Overview of GED

1.2.1. Basic experiment and principles

The basic GED experiment is shown in **Figure 1.1** and consists of intersecting a monochromatic electron beam of a known wavelength with a gaseous sample and recording the pattern of scattered electrons at a known distance using an electron-sensitive detector. The background pressure inside the chamber must be kept low to avoid scattering of the electrons at points other than at the nozzle tip, so the beam of gas is usually trapped by a cold finger cooled with liquid nitrogen.

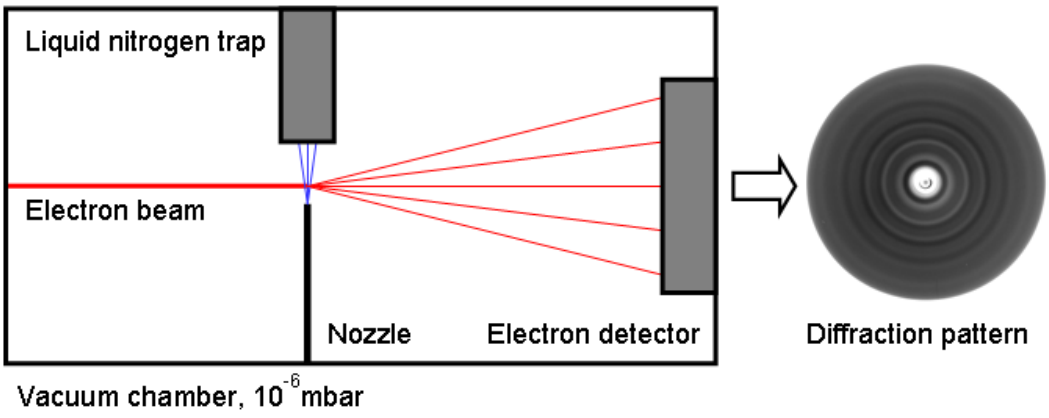

Figure 1.1 – Schematic diagram of the electron diffraction experiment.

The information about the molecular geometry is contained in the period and amplitude of the oscillations in the diffraction pattern. Theoretical intensity curves (**Section 1.4.2**) are calculated for model structures and the experimental structure is

obtained by minimising the difference between the theoretical and experimental diffraction intensities.

1.2.2. Historical development of GED

The first GED experiment was performed by Mark and Wierl[3] shortly after Debye had shown that X-ray diffraction patterns could be obtained for molecules in the gas phase.[4] The shorter exposure times required for acquisition of electron-diffraction patterns resulted in electrons being the preferred gas-phase diffraction probe. However, as the accuracy of the technique has improved over the years a second advantage of using electrons over X-rays has emerged. As X-rays are scattered by the low-energy electrons within the molecule they reveal centres of electron density, which are close to, but not necessarily coincident with the nuclear positions. In contrast, incident high-energy electrons are scattered by the electric potential gradient, which is only significantly large at the edge of the nuclei, therefore probing the nuclear positions much more directly.

The data for the first molecular structure refinements were obtained by the so-called 'visual method', whereby the positions and intensities of the observed maxima and minima of interference fringes were estimated by eye. Theoretical scattering intensity curves were then calculated for a handful of model structures and the model that produced the closest match between the theoretical and estimated intensities was presented as correct. It was quickly pointed out by Wierl that the observed maxima and minima were not in fact real but were clearly visible because our eyes compensate for the steeply falling background, so the theoretical intensities had to be altered accordingly. A more objective approach was proposed by Pauling and Brockway,[5] who realised that the estimation of scattered intensities could be eliminated in favour of recording the optical density of the photographic plate using a photometer. Owing to the form of the electron scattering equations, a Fourier transformation of the optical density data obtained from the photometer would provide a distribution of inter-nuclear distances, known as a radial-distribution curve.

At that time, however, the quality of the photometer data was poor and the visual method remained the predominant interpretive method.

The next stage in the development of GED occurred as a result of the introduction of the rotating sector and an improvement in the photometer technique. The rotating sector was independently suggested by Finback[6] and Debye[7] and is simply a rotating metal disk that is shaped so that it has an opening angle of a known smooth function of its radius, *R*, typically about R^3 or R^4 (**Figure 1.2**). This is placed in front of the photographic plate in order to compensate for the steeply falling intensities. The improvement in the photometer method was pioneered by Jerome and Isabella Karle,[8] who built a device to spin photographic plates[9] whilst recording the optical density, dramatically improving the quality of the data at the wider angles. Although the rotating sector was developed a number of years before the Karles' photometer method, problems putting the rotating sector into practice[10] meant that the two methods were adopted more widely by gas electron diffractionists at around the same time. The combination of these two technologies became known as the sector-photometer method and by the early 1950's this was the state of the art.[11]

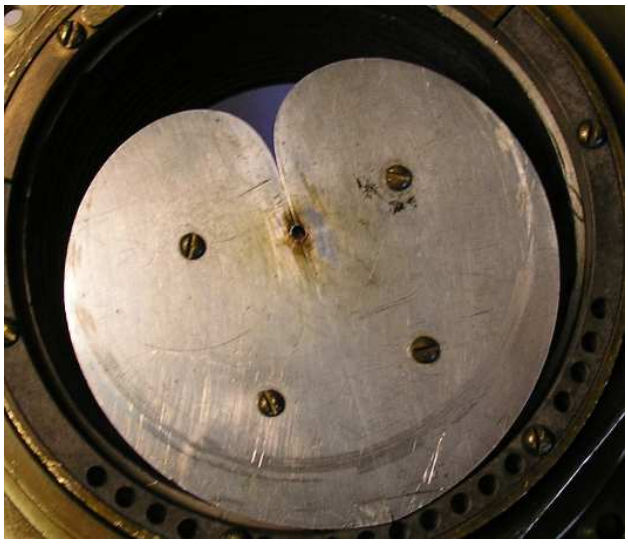

Figure 1.2 – The Edinburgh rotating sector.

In addition to these experimental improvements, the use of computers has made a big impact on the analysis of electron diffraction data. Initially their use was limited to the calculation of molecular-intensity and radial-distribution curves,[12,13] but in the late 1950's least-squares refinement methods began to be applied to the refinement process,[14] eliminating the subjective step of deciding which model produced the best fit between theoretical and experimental intensity curves. More recently, the steady increase in computational power has allowed more reliable electronic structure calculations to be performed. These were initially incorporated into electron diffraction refinements by the MOCED (Molecular Orbital Constrained Electron Diffraction) method[15] in which poorly defined structural parameters were fixed to those predicted by theoretical methods. This allowed a much greater range of molecules to be studied, but had the drawbacks that any parameters that were correlated to those that were fixed would have underestimated uncertainties and, as the theoretical values would not necessarily be correct, fixing these parameters could yield an incorrect structure. Both of these problems were resolved by the SARACEN (Structural Analysis Restrained by *Ab initio* Calculations for Electron diffractioN) method[16] by introducing the calculated parameters as if they were additional experimental data. In this method the calculated parameters are treated as flexible restraints, with an uncertainty derived from the degree of convergence of the calculations.

As the SARACEN method has increased the size of molecules that are investigated by GED, the limiting factor has become the volatility of the prospective compound. As long as the compound is suitably stable, this can be circumvented by heating the sample, and apparatus for electron diffraction almost invariably incorporates a heated nozzle. For compounds that decompose at elevated temperatures this is not an option and so longer exposure times, higher beam currents or more sensitive detection methods are required.

The current standard for routine, accurate structure determination (as used for the determination of carborane and sulfonate structures in **Chapters 6** and **7**,

respectively) is an apparatus equipped with a rotating sector, heated nozzle and detection using either photographic film or electron image plates. Data extraction is now more conveniently performed using high-resolution scanners and an appropriate program to extract the data from the resulting image file, rather than using a densitometer. Refinements are performed using least-squares procedures, often making use of the SARACEN method, although the MOCED method is sometimes still adopted.

1.3. Alternative experimental setups and extensions of GED

Since the establishment of the sector-photometer method, a number of alternative experimental setups have been investigated, varying the electron gun type, the gas delivery system, the detector or a combination of these. This was usually done with some specific goal in mind, which has generally fallen into one of three main categories:

1. To test the limitations of the independent atom model (IAM) that is employed universally in electron scattering theory and to investigate related properties such as the chemical binding energy.

2. To observe the structures of clusters in the gas phase.

3. To perform time-resolved or ultra-fast electron diffraction (UED) in order to observe the progress of chemical reactions or characterise species that are stable for only a fraction of a second.

1.3.1. High accuracy GED

For the first of these applications the total scattered electron intensity at small angles must be known very accurately, more so than for a molecular structure determination. An apparatus was designed and built by Fink and Bonham[17] (**Figure 1.3**) for this purpose, incorporating an electron-counting detection method using a plastic scintillator mounted on top of a photomultiplier. Measurements were taken at a single scattering angle at a time, with a second detector mounted at a fixed scattering angle to monitor variations in the count rate due to fluctuations in electron beam intensity and the gas flow rate.

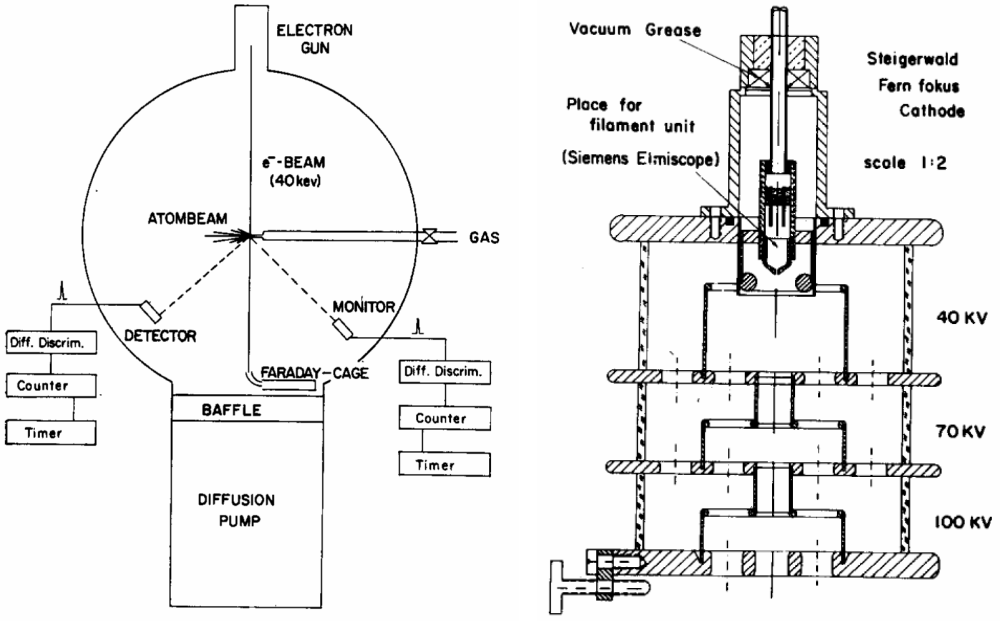

Figure 1.3 – Schematic of Fink and Bonham's apparatus and a technical drawing of their electron gun (Ref. 17).

This was initially used to estimate the molecular binding energies of N_2O and CO_2 by examining the differences between the experimental and theoretical (as assumed by the IAM) electron scattering intensities, but the uncertainties were large and a study of the contributory errors indicated that the largest errors were introduced during measurement of the scattering angle.[17] Inspired by this work, Konaka built a

similar apparatus[18] with an improved method of measuring the scattering angle and restricting the noise due to light from the electron gun filament by placing a thin layer of aluminium over the scintillator. In this case the electron beam was produced by a commercial electron microscope gun rather than a telefocus gun as used by Fink and Bonham. However, despite the lower electron beam intensities, data for H_2O were obtained and a chemical binding energy consistent with thermochemical data was estimated.

1.3.2. GED of clusters

The application of GED to the study of clusters in the gas phase was begun by a group from Orsay in France, who built an apparatus[19,20] (**Figure 1.4**) that utilised a supersonic nozzle[21,22] (see also **Chapter 2**) in place of an ordinary effusive nozzle. Using this apparatus they were able to obtain argon clusters in the gas phase and determine their size and crystallinity.

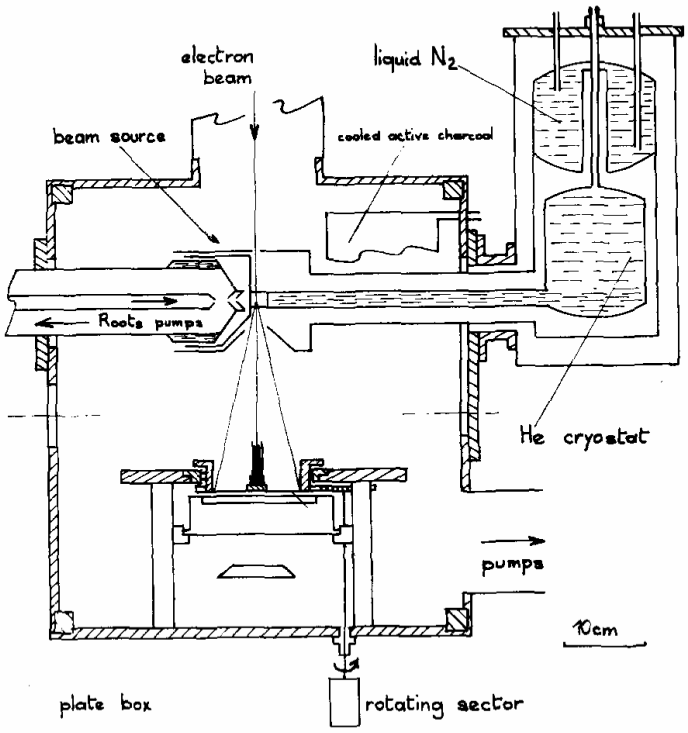

Figure 1.4 – Scale drawing of the Orsay apparatus (Ref. 20).

A handful of groups have since followed in their footsteps and have applied this technology to the study of clusters of various small molecules such as N_2, H_2O and SF_6. Stein's group were the first to follow suit[23] and initially employed the same experimental setup as the French group, with a rotating sector and photographic detection, but later modified the apparatus to use an electron-counting detection system.[24] This was similar to that of Fink, making use of a plastic scintillator mounted on a photomultiplier, but incorporated a more sophisticated method of correcting for background scattering of electrons, whereby a molecular beam chopper was synchronised with the counting electronics. Bartell was the next to enter the field in the early 1980s,[25] again basing his apparatus on the Orsay design, although he was content to use the traditional rotating sector and photographic plate detection method. He chose instead to concentrate his efforts on optimising the gas delivery method and was the first to show that pulsed supersonic jets could be used in conjunction with electron diffraction,[26] despite the inevitable local magnetic fields produced by such a source. Another group to combine a supersonic nozzle with electron diffraction in the pursuit of cluster structures was that led by Monot.[27] In contrast to the other three groups, Monot's apparatus was designed to investigate metal clusters and was equipped with an electron gun capable of producing 100 kV electrons, rather than settling for the more usual 40 kV. As a detection method Monot incorporated a pair of linear CCD imagers that were exposed directly to the incident electrons, enabling individual electrons to be counted, but with much reduced data acquisition times compared to the counting methods adopted by Fink and Stein.

The main drawback of using supersonic beams to obtain structures of clusters is that a range of cluster sizes and shapes are produced in a supersonic expansion. This range of cluster sizes can be adjusted by carefully controlling various parameters such as the nozzle pressure and orifice diameter. However, a more elegant solution was found by Parks *et al.*[28] who, rather than intersecting the electron beam with a supersonic molecular beam, used a radio-frequency (RF) Paul trap[29] to hold clusters in the electron beam (**Figure 1.5**). As the density of target clusters in the RF Paul

trap is even lower than in the supersonic beam, the background gas pressure had to be reduced from around 10^{-6} Torr to less than 10^{-8} Torr, presumably by baking the walls of the diffraction chamber. The electron detection in Park's apparatus was performed by mounting a microchannel plate, which acts as an electron multiplier, onto a phosphor screen, producing a diffraction pattern that is then imaged using an external CCD camera. Recently, Schooss has built a similar apparatus in Karlsruhe[30] and these two groups have characterised a number of gold and silver clusters ranging in size from 11 to 79 atoms.[31,32]

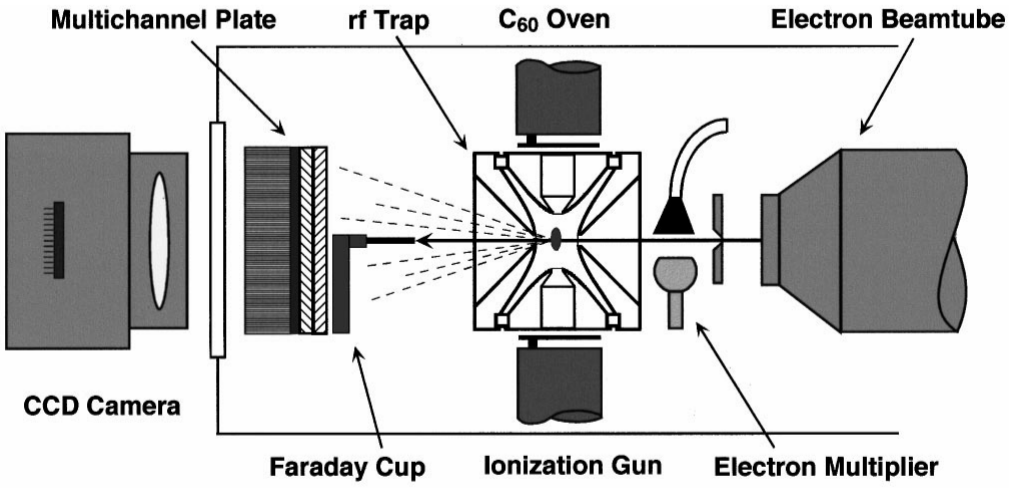

Figure 1.5 – Park's original trapped-ion electron diffraction apparatus (Ref. 28).

1.3.3. Time-resolved and ultrafast electron diffraction (TRED, UED)

The attempt to observe structural change and to measure the timescales of chemical reactions is probably the most ambitious application of electron diffraction. This endeavour grew out of attempts by Ischenko *et al.* to observe short-lived species by a stroboscopical GED method, whereby diffraction patterns were generated using a pulsed electron source and the short-lived species of interest were generated by photolysis using a high-intensity pulsed laser. Using this method they were able to demonstrate changes in the diffraction pattern for the dissociation of CF_3I into CF_3

and I radicals, but were unable to extract any corresponding quantitative changes in structure.[33]

In Ischenko's apparatus the electron pulses were created by deflecting the electron beam between pulses, whilst the detector employed was based on the scanning type of method, where the electron intensity at a given scattering angle was measured against a reference. Over the next few years Ewbank and Schäfer improved upon both the detection method[34] and also the electron pulse generation,[35] eventually allowing quantitative interpretation of pulsed GED data for the photodissociation of CS_2 and chlorine-substituted ethenes in the nanosecond time domain.[36] Their novel detector allowed a whole intensity curve to be captured in 16 ms and was based on a phosphor screen that was optically coupled to a linear photodiode array, whilst their improvement in the electron pulse generation was based on the use of a photocathode in place of beam deflection. This differs from a conventional gun (see **Chapter 3**) in the way in which electrons are released from the cathode. Rather than creating a continuous source of electrons by thermionic emission from a filament cathode, the electrons are released in a short pulse from the cathode using an even shorter light pulse *via* the photoelectric effect, after which they are accelerated towards the anode in the usual way.

Ahmed Zewail is another significant contributor to this field and has tried three generations of experimental setup (UED-1, -2 and -3) in pursuit of improving the temporal resolution from the nanosecond to femtosecond domain.[37-41] All three made use of an electron gun with a photocathode, but these varied in their operating voltages and focusing methods. In terms of the vacuum chamber design, in UED-1 the electron gun, the diffraction point and the detector were all housed in a single chamber. However, it was found that increases in the background pressure as the molecular beam was turned on caused the electron gun to arc. Therefore in UED-2 a differential pumping scheme was adopted with three chambers: one for the electron gun, one for the scattering zone and one to house the detector. In UED-3 (**Figure 1.6**) a similar approach was adopted, but the apparatus incorporated a fourth

chamber, into which the molecular beam was directed, and which contained a time-of-flight mass spectrometer. The final feature in each of these cases is the detector itself. In all three the detection was performed using a 2D CCD detector. In UED-1 this was operated by direct bombardment, but in order to increase the CCD lifetime, in UED-2 a dual-mode detector was used. This consisted of a cover onto which a small CCD was mounted to work by direct bombardment, in order to calibrate the zero of time. Behind the cover was a phosphor screen coupled via a fibre optic taper to an image intensifier, which was then fed by a second fibre optic taper to the CCD. The detector in UED-3 then followed a similar design, but included a 500 nm aluminium coating on the phosphor screen to exclude scattered light and a graded optical filter to prevent saturation of the CCD at small angles.

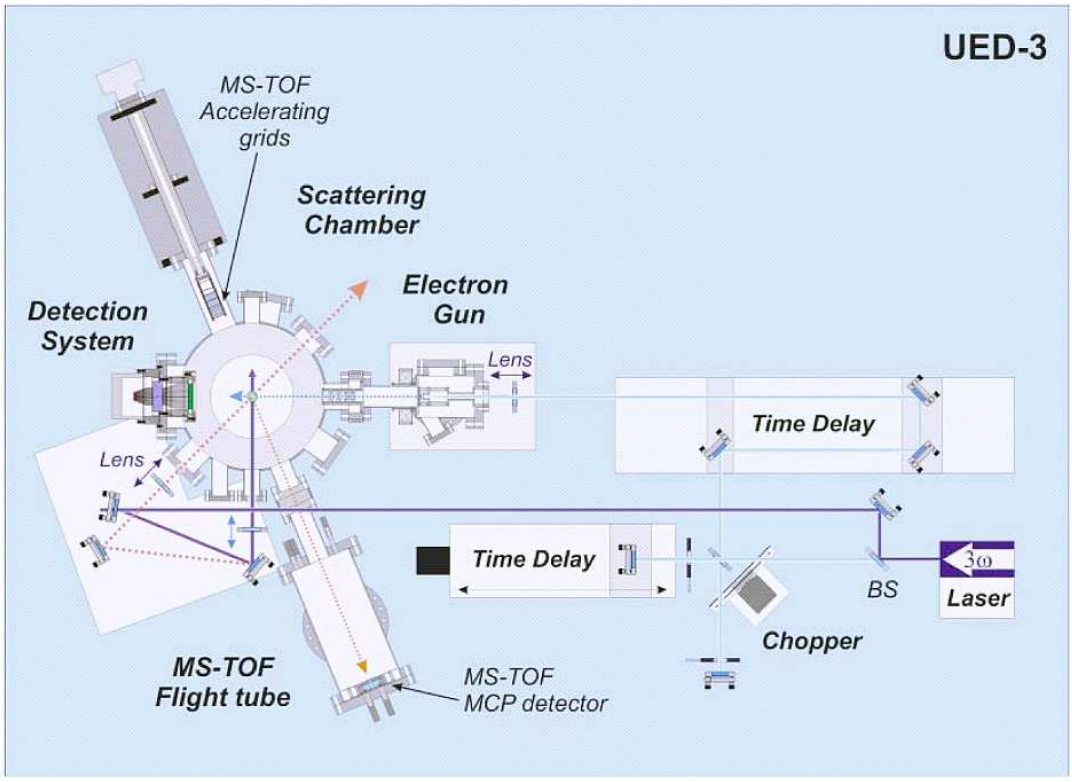

Figure 1.6 – Zewail's UED-3 apparatus (Ref. 41).

1.4. Theoretical background

1.4.1. Fundamental expressions

As for any diffraction technique, the wavelength, λ, of the radiation used is of fundamental importance to electron diffraction. This of course comes from de Broglie's famous relationship (**Equation 1.1**) for the wavelength of a particle with a mass, m, moving at a speed, v. In GED, however, the scattered electrons are travelling close to the speed of light so the mass of the electron is not the same as its rest mass, m_e, and the momentum, mv, must be found using relativistic mechanics. The actual wavelength of the particle is therefore provided by **Equation 1.2**, where V is the accelerating voltage.

$$\lambda = \frac{h}{mv} \tag{1.1}$$

$$\lambda = \frac{h}{\sqrt{2m_e Ve\left(1 + Ve/2m_e c^2\right)}} \tag{1.2}$$

The second important quantity in GED is the scattering vector, **s** (magnitude, s), which is a measure of the momentum transfer during the scattering event and is defined in **Figure 1.7**. This is a useful quantity to define as it simplifies the scattering equations so that they can be written in terms of s rather than λ and the scattering angle, θ, and therefore allows intensity data from different experiments, in which different accelerating voltages may have been used, to be easily compared.

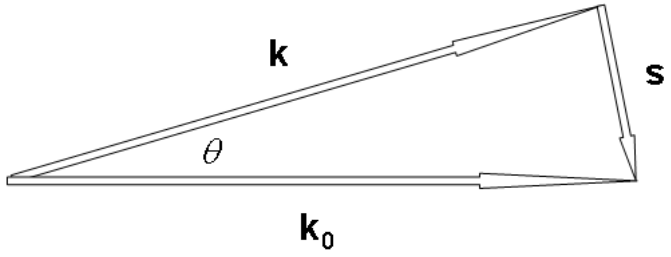

Figure 1.7 – The definition of the scattering vector, **s**. $\mathbf{k}_0$ is the wavevector for an electron in the incoming electron beam and **k** is the wavevector for the scattered electron. If the electron is scattered elastically (an assumption generally applied in conventional GED) the magnitudes of $\mathbf{k}_0$ and **k** are equal to k (= $2\pi/\lambda$), so the magnitude of **s** is given by $s = 4\pi \sin(\theta/2) / \lambda$.

1.4.2. GED electron scattering equations

As with the GED experiment, the theory behind GED has evolved over the years and was born out of Mark and Wierl's attempt to interpret the first GED photographs. Their approach was a simplified adaptation of the method developed by Debye[42] and Ehrenfest[43] for X-ray scattering and to some extent the scattering equations used today still resemble the original "Wierl equation" (**Equation 1.3**), which was derived as follows. The molecule scattering the electrons was assumed to be static with a set of fixed interatomic distances, where r_{ij} is the distance between atoms i and j and the total scatting intensity is given by **Equation 1.4**, where F_i, the scattering function for atom i, is simply its atomic number, Z_i, minus its scattering factor for X-rays, f_i.

$$I(s)_{\text{apparent}} \approx \frac{I(s)_{\text{molecular}}}{I(s)_{\text{atomic}}} \approx \sum_{\text{i}}^{N} \sum_{j \neq i}^{N} Z_i Z_j \frac{\sin sr_{ij}}{sr_{ij}} \qquad (1.3)$$

$$I(s) = \sum_{i}^{N} \sum_{j}^{N} F_i(s) F_j(s) \frac{\sin sr_{ij}}{sr_{ij}} \qquad F_i(s) = \frac{Z_i - f_i}{s^2} \qquad (1.4)$$

The case where $i = j$ is the scattering from a single atom, so the total scattering can be written as sum of atomic and molecular contributions (**Equation 1.5**).

$$I(s) = I(s)_{\text{atomic}} + I(s)_{\text{molecular}} \tag{1.5}$$

Wierl recognised that the observed maxima and minima on the photographic plates were not real, however, but just appeared so because the eye corrects for the steeply falling background caused by the atomic scattering. He therefore modified the theoretical molecular scattering curves by dividing them by the atomic scattering so that they approximately reproduced the observed scattering pattern. In addition, Wierl simplified the equations by assuming that the $Z - f$ terms roughly cancel to give the Wierl equation, **Equation 1.3**.

This treatment was generally satisfactory for the visual interpretation of diffraction patterns, but as the use of the sector-photometer method became widespread it was clear that the current theory was insufficient. First, a molecule is not static but is constantly vibrating. Therefore **Equation 1.4** has to be modified to include the probability of the distance between atoms i and j being equal to r, $P_{ij}(r)$ (**Equation 1.6**). If we assume the interatomic potential to be a harmonic oscillator, both a classical Boltzmann population and a quantum-mechanical ground-state wavefunction yield a Gaussian distribution for $P_{ij}(r)$. **Equation 1.6** can then be simplified to give **Equation 1.7**, where u_{ij} is the root-mean-squared amplitude of vibration for the pair of atoms i and j.

$$I(s)_{\text{molecular}} = \sum_i \sum_j F_i(s) F_j(s) \int P_{ij}(r) \frac{\sin sr}{sr} \mathrm{d}r \tag{1.6}$$

$$I(s)_{\text{molecular}} = \sum_i \sum_j F_i(s) F_j(s) \exp(-u_{ij}^2 s^2/2) \frac{\sin sr_{ij}}{sr_{ij}} \tag{1.7}$$

A second problem was encountered when atoms of very different atomic numbers were present in the molecule, such as in UF_6, for which a structure including two different U–F distances was wrongly proposed. This was found by Schomaker and

Glauber[44] to be due to breakdown of the first Born approximation, which manifests itself in contraction of the electron wavelength as it approaches the heavier atom, resulting in a phase shift in the electron wavefunction. This problem was solved by using complex electron scattering factors, so that **Equation 1.7** is modified to give **Equation 1.8**, where η_i is the phase shift induced by atom *i*.

$$I(s)_{\text{molecular}} = \sum_i \sum_j \left|F_i(s)\right| \left|F_j(s)\right| \cos(\eta_i - \eta_j) \exp(-u_{ij}^2 s^2/2) \frac{\sin sr_{ij}}{sr_{ij}} \qquad (1.8)$$

This equation is sufficiently accurate to calculate theoretical intensity curves for most routine electron diffraction refinements, but there is still room for improvement. In particular, the assumption of a harmonic potential is not always good enough, especially for bonded distances. However, if the ground state of a Morse oscillator is used for $P_{ij}(r)$ rather than that of the harmonic oscillator, it has been shown[45] that the integral in **Equation 1.6** can be approximated by **Equation 1.9**, where the asymmetry constant, κ_{ij}, is given by **Equation 1.10**. For the structure investigations in **Chapters 6** and **7** the asymmetry coefficient, *a*, in **Equation 1.10** was assumed to be 2 Å^{-1} for bonded distances, whilst a harmonic approximation ($a = 0$) was used for non-bonded distances.

$$\int P_{ij}(r) \frac{\sin sr}{sr} \mathrm{d}r \approx \exp\left(-u_{ij}^2 s^2/2\right) \frac{\sin\left[s\left(r_{ij} - \kappa_{ij} s^2\right)\right]}{sr_{ij}} \qquad (1.9)$$

$$\kappa_{ij} \approx \frac{a u_{ij}^4}{6} \qquad (1.10)$$

1.4.3. Radial-distribution curves

The radial-distribution curve (RDC) is a powerful visualisation tool that helps to interpret the molecular intensity curves in a more intuitive way. It was introduced by

Pauling and Brockway in 1935[5] as an alternative method for obtaining internuclear distances, whereby a maximum in this function could correspond to a specific distance. At that time, however, high-quality intensity data was lacking so it assumed the role of providing starting geometries for further refinement. As the quality of intensity data and the accuracy of the technique improved with introduction of the sector-photometer method, theoretical advances had also been made and it was clear that vibrational averaging resulted in a maximum in the RDC which was sufficiently different to the weighted average, r_a, for its role to remain an interpretive tool. In modern structure refinements the RDC is still as powerful as it shows which distances in the molecule are responsible for discrepancies between the theoretical and experimental intensities.

In order to understand where the RDC comes from it is helpful to compare the molecular scattering equation (**Equation 1.6**) with those for a Fourier transform, $f(x)$, and an inverse Fourier transform, $F(\theta)$ (**Equation 1.11**). If the molecule to be studied contained only one type of atom, **Equation 1.12** (A is a constant) would give the radial-distribution function exactly.

$$f(x) = \int_{-\infty}^{\infty} F(\theta)\exp(\mathrm{i}\theta x)\mathrm{d}\theta \qquad F(\theta) = \frac{1}{2\pi}\int_{-\infty}^{\infty} f(x)\exp(-\mathrm{i}\theta x)\mathrm{d}x \tag{1.11}$$

$$\frac{P(r)}{r} = A\int_{0}^{\infty} \frac{sI(s)_{\text{molecular}}}{\left|F(s)\right|^2}\sin(sr)\mathrm{d}s \tag{1.12}$$

In practice the exact radial-distribution function cannot be found as there are usually a number of atom types, so the data are divided by the modulus of the scattering factors of the pair of atoms that contribute the most to the scattering pattern. The resulting RDC is therefore weighted by the scattering power of the different atom types, and the phase shift, which is accounted for by using complex scattering factors, can give rise to splitting of the corresponding peaks. In addition, the data are

collected over a finite s range from s_{min} to s_{max}. The lack of data from zero to s_{min} can result in a shift of the zero line in $P(r)/r$ and termination of the data at s_{max} induces a ripple in the RDC. Theoretical data is therefore introduced between $s = 0$ to s_{min} and from s_{max} to some chosen limit, in our case 36 $Å^{-1}$. This upper limit still affects the RDC, but can be compensated for by multiplying the data by a damping factor, $\exp(-as^2)$, where a is of the order of 10^{-5} $Å^2$. Finally, the data also have a finite interval so the integral is replaced by a summation.

1.4.4. Distance corrections due to vibrational motion

As was hinted at in the previous two sections, there are various types of distances quoted in GED literature. The distance obtained from electron diffraction data, r_a, is the reciprocal of averaged reciprocal distances, as expressed in **Equation 13**. The average internuclear separation, r_g, can be approximated as in **Equation 14**.

$$r_a = \left\langle \frac{1}{r} \right\rangle^{-1} \tag{1.13}$$

$$r_g = \langle r \rangle \approx r_a + \frac{u^2}{r} \tag{1.14}$$

Ideally, a structural chemist would like to know the equilibrium structure, as obtained in *ab initio* calculations, and a few methods have been developed to try to extrapolate back from the r_a distances to the equilibrium distances, r_e. Indeed, a new EXPRESS method[46] has recently been developed to enable the recovery of equilibrium distances, but requires the calculation of the potential-energy surface so is computationally expensive for reasonably large molecules. However, careful selection and modelling of the critical anharmonic normal modes by this method combined with a traditional approach for the remaining normal modes may prove to be a practical implementation of this method. The method used throughout this thesis

is the SHRINK method[47] which uses a harmonic force field derived from a minimum in the potential-energy surface and corrects for curvilinear motion, perpendicular to the internuclear axis, yielding k_{h1} distance corrections that relate the subsequent r_{h1} distances to the experimental r_a distances by **Equation 1.15**.

$$r_{h1} = r_a + \frac{u^2}{r} - k_{h1} \tag{1.15}$$

1.4.5. The SARACEN method and *ab initio* structure calculations

The SARACEN method[16] was developed as a way to refine structures that would require to be defined by more parameters than there were useful data for. Previously the GED model would have to have been supplemented by other experimental data, assumptions of local symmetry would have to have been made, or parameters fixed to assumed values. It works by including calculated parameters as if they were experimental data, by using flexible restraints with uncertainties based on the degree of convergence of the calculations. In order to apply appropriate restraints some level of understanding of molecular structure calculations is therefore required and a brief explanation of the Hartree-Fock (HF) and Møller-Plesset (MP*x*) methods, and the basis sets used in **Chapters 6** and **7** now follows. (Numerous texts have been devoted to electronic structure calculations and for more detail it is recommended to refer to one of these, *e.g.* reference 48.)

Electronic molecular structure calculations find approximations to solutions of the time-independent Schrödinger equation (**Equation 1.16**), where the Hamiltonian operator, $\hat{H}$, is defined by the nuclear coordinates (**Equation 1.17**) and an equilibrium geometry is obtained when a minimum in *E* has been found with respect to the internal nuclear coordinates.

$$\hat{H}\psi = E\psi \tag{1.16}$$

$$\hat{H} = \hat{T}_e + \hat{V}_{ne} + \hat{V}_{ee} + \hat{V}_{nn} \tag{1.17}$$

$$= -\sum_i^N \frac{1}{2}\nabla_i^2 - \sum_i^N \sum_a \frac{Z_a}{|\mathbf{R}_a - \mathbf{r}_i|} + \sum_i^N \sum_{j>i}^N \frac{1}{|\mathbf{r}_i - \mathbf{r}_j|} + \sum_a \sum_{b>a} \frac{Z_a Z_b}{|\mathbf{R}_a - \mathbf{R}_b|}$$

The HF approximation uses the exact Hamiltonian, but approximates the wavefunction by assuming it to be a Slater determinant composed of single-electron spin orbitals as shown in **Equation 1.18**. As indicated by **Equations 1.19**, the spin orbital for electron j is denoted by $\chi_i^{\alpha}(j)$ [or $\chi_i^{\beta}(j)$] and is the product of the i^{th} molecular orbital (MO_i) and either an α or β spin function.

$$\psi_{SD} = \frac{1}{\sqrt{n!}} \begin{vmatrix} \chi_1^{\alpha}(1) & \chi_1^{\beta}(1) & \chi_2^{\alpha}(1) & \chi_2^{\beta}(1) & \cdot & \chi_{n/2}^{\beta}(1) \\ \chi_1^{\alpha}(2) & \chi_1^{\beta}(2) & \chi_2^{\alpha}(2) & \chi_2^{\beta}(2) & \cdot & \chi_{n/2}^{\beta}(2) \\ \cdot & \cdot & \cdot & \cdot & \cdot & \cdot \\ \chi_1^{\alpha}(n) & \chi_1^{\beta}(n) & \chi_2^{\alpha}(n) & \chi_2^{\beta}(n) & \cdot & \chi_{n/2}^{\beta}(n) \end{vmatrix} \tag{1.18}$$

$$\chi_i^{\alpha} = MO_i\alpha \quad \text{and} \quad \chi_i^{\beta} = MO_i\beta \tag{1.19}$$

Both the molecular orbitals and the spin functions are orthonormal so the spin orbitals are also orthonormal. The molecular orbitals are constructed using the Linear Combination of Atomic Orbitals approach as shown in **Equation 1.20**, where c_{ij} is the weighting of the j^{th} atomic orbital in the i^{th} molecular orbital.

$$MO_i = \sum_j c_{ij} AO_j \tag{1.20}$$

The atomic orbitals used to construct the molecular orbitals are known as basis functions and there are numerous ways to construct these. All of the calculations reported in later chapters have used Gaussian-type orbitals, which (expressed in polar coordinates) have the form shown in **Equation 1.21**, where $Y_{l,ml}(\theta,\varphi)$ is the spherical

harmonic function for the quantum numbers *l and* m_l, and a_i is the weighting of a Gaussian function with exponent b_i.

$$AO_{n,l,m_l}(r,\theta,\varphi) = Y_{l,m_l}(\theta,\varphi) r^{(2n-2-l)} \sum_i a_i \mathrm{e}^{-b_i r^2} \tag{1.21}$$

The summation in (1.21) is required as more than one Gaussian is needed to describe each atomic wavefunction adequately. However, a number of these are often grouped together with values of a_i fixed relative to one another and likewise for b_i, so that only two parameters have to be optimised, one exponent and a normalisation coefficient. As an example, the Pople-style basis set, 6-31G uses six Gaussians with fixed relative exponents to describe the core electrons and for the valence electrons uses three Gaussians with fixed relative exponents and one that is unconstrained.

The general procedure by which the energy of the system, *E*, in (1.16) is minimised is therefore to vary the values of *a*, *b* and *c* for each MO (within certain constraints such as orthonormality of AOs and MOs) until a minimum in *E* is found for the initial Hamiltonian. The process is then repeated for a new set of nuclear coordinates (and therefore a new Hamiltonian) until a minimum in the potential-energy landscape is found. The minimised energy obtained using the HF method typically represents 99% of the true energy and the difference between the HF limit (HF energy using an infinitely large basis set) and the true energy is called the correlation energy.

There are various methods available to account for the correlation energy in the calculation, the most straightforward being to approximate the electronic wavefunction better by using more Slater determinants. A less computationally expensive method, however, is that proposed by Møller and Plesset, whereby the correlation energy is obtained by defining the Hamiltonian as a sum of a reference, $\hat{H}_0$, and a perturbation, $\hat{H}'$, multiplied by a variable perturbation parameter, λ (**Equation 1.22**). The wavefunction is then expanded in terms of λ as a Taylor series

(**Equation 1.23**) and the energy calculated when this series is terminated at the x^{th} term is the MP*x* energy. It can be shown that the MP1 energy is the same as the HF energy and restraints used in the SARACEN refinements in **Chapters 6** and **7** were determined from geometry optimisations using the MP2 level of theory.

$$\hat{H} = \hat{H}_0 + \lambda\hat{H}' \tag{1.22}$$

$$\psi = \lambda^0\psi_0 + \lambda^1\psi_1 + \lambda^2\psi_2 + ... + \lambda^x\psi_x \tag{1.23}$$

1.5. References

1. G. N. Lewis, *J. Am. Chem. Soc.* (1916), **38**, 762.
2. E. Hückel, *Z. Phys.* (1931), **70**, 204.
3. (a) H. Mark and R. Wierl, *Naturwiss.* (1930), **18**, 205. (b) H. Mark and R. Wierl, *Z. Phys.* (1930), **60**, 741.
4. P. Debye, *Phys. Zeits.*, (1929), **30**, 524.
5. L. Pauling and L. O. Brockway, *J. Am. Chem. Soc.* (1935), **57**, 2684.
6. C. Finback, *Avh. Norsk Vidensk.-Acad., Oslo, M.-N. Kl*, No.13 (1937).
7. P. P. Debye, *Physik* (1939), **40**, 404.
8. J. Karle and I. L. Karle, *J. Chem. Phys.* (1947), 764.
9. I. L. Karle, D. Hoober and J. Karle, *J. Chem. Phys.* (1947), 765.
10. C. Finback, O. Hassel and B. Ottar, *Arch. f. Math. Og Nat., Oslo, No. 13* (1941), B44.
11. L. O. Brockway and L. S. Bartell, *Rev. Sci. Instrum.* (1954), **25**, 569.
12. P. A. Shaffer, Jr., V. Schomaker and L. Pauling, *J. Chem. Phys.* (1946), **14**, 659.
13. J. Karle and I. L. Karle, *J. Chem. Phys.* (1950), **18**, 957.
14. R. A. Bonham and L. S. Bartell, *J. Chem. Phys.* (1959), **31**, 702.
15. V. J. Klimkowski, J. D. Ewbank, C. van Alsenoy and L. Schäfer, *J. Am. Chem. Soc.* (1982), **104**, 1476.
16. (a) A. J. Blake, P. T. Brain, H. McNab, J. Miller, C. A. Morrison, S. Parsons, D. W. H. Rankin, H. E. Robertson and B. A. Smart, *J. Phys. Chem.* (1996), **100**, 12280. (b) N. W. Mitzel and D. W. H. Rankin, *J. Chem. Soc., Dalton Trans.* (2003), 3650.
17. M. Fink and R. A. Bonham, *Rev. Sci. Instrum.* (1970), **41**, 389.
18. S. Konaka, *Jpn J. Appl. Phys.* (1972), **11**, 1199.
19. P. Audit, *J. Phys. (Paris)* (1969), **30**, 192.
20. B. Raoult and J. Farges, *Rev. Sci. Instrum.* (1973), **44**, 430.
21. A. Kantrowitz and J. Grey, *Rev. Sci. Instrum.* (1951), **22**, 328.
22. R. Campargue, *Rev. Sci. Instrum.* (1964), **35**, 111.
23. G. Stein and J. A. Armstrong, *J. Chem. Phys.* (1973), **58**, 1999.
24. S. S. Kim and G. Stein, *Rev. Sci. Instrum.* (1982), **53**, 838.

25. L. S. Bartell, R. K. Heenan and M. Nagashima, *J. Chem. Phys.* (1982), **78**, 236.
26. L. S. Bartell and R. J. French, *Rev. Sci. Instrum.* (1989), **60**, 1223.
27. B. D. Hall, D. Reinhard, J.-P. Borel and R. Monot, *Rev. Sci. Instrum.* (1991), **62**, 1481.
28. M. Maier-Borst, D. B. Cameron, M. Rokni and J. Parks, *Phys. Rev. A* (1999), **59**, R3162.
29. J. H. Parks, S. Pollack and W. Hill, *J. Chem. Phys.* (1994), **101**, 6666.
30. D. Schooss, M. N. Blom, J. H. Parks, B. v. Issendorff, H. Haberland and M. M. Kappes, *Nano Lett.* (2005), **5**, 1972.
31. X. Xing, B. Yoon, U. Landman and J. H. Parks, *Phys. Rev. B* (2006), **74**, 165423.
32. M. Blom, D. Schooss and J. Stairs, *J. Chem. Phys.* (2006), **124**, 244308.
33. A. A. Ischenko, V. V. Golubkov, V. P. Spiridonov, A. V. Zgurskii, A. S. Akhmanov and M. G. Vabischvich, *Appl. Phys. B* (1983), **32**, 161.
34. J. D. Ewbank, L. Schäfer, D. W. Paul, O. J. Benston and J. C. Lennox, *Rev. Sci. Instum.* (1984), **55**, 1598.
35. J. D. Ewbank, W. L. Faust, J. Y. Luo, J. T. English. D. L. Monts, D. W. Paul, Q. Dou and L. Schäfer, *Rev. Sci. Instum.* (1992), **63**, 3352.
36. A. A. Ischenko, V. P. Spiridonov, L. Schäfer and J. D. Ewbank, *J. Mol. Struct.* (1993), **300**, 115.
37. J. C. Williamson and A. H. Zewail, *Proc. Nat. Acad. Sci.* (1991), **88**, 5021.
38. J. C. Williamson, M. Dantus, S. B. Kim and A. H. Zewail, *Chem. Phys. Lett.* (1992), **196**, 529.
39. J. C. Williamson, J. Cao, H. Ihee, H. Frey and A. H. Zewail, *Nature* (1997), **386**, 159.
40. H. Ihee, V. A. Lobastov, U. M. Gomez, B. M. Goodson, R. Srinivasan, C. Ruan and A. H. Zewail, *Science* (2001), **291**, 458.
41. R. Srinivasan, V. A. Lobastov, C. Ruan and A. H. Zewail, *Helv. Chim. Acta* (2003), **86**, 1763.
42. P. Debye, *Ann. D. Physik* (1915), **38**, 809.
43. P. Ehrenfest, *Amsterdam Acad.* (1915), **23**, 1132.
44. V. Schomaker and R. Glauber, *Nature* (1952), **170**, 290.

45. Molecular Structure by Diffraction Methods, Volume 1, Chapter 1, pp. 13, *The Chemical Society* (1973).
46. P. D. McCaffrey, R. J. Mawhorter, A. R. Turner, P. T. Brain and D. W. H. Rankin, *J. Phys. Chem. A* (2007), **111**, 6103.
47. V. A. Sipachev, *J. Mol. Struct. (THEOCHEM)* (1985), **121**, 143.
48. Introduction to Computational Chemistry, F. Jensen, *Wiley* (1999).

Chapter 2

Overview of the state-specific electron diffraction apparatus

2.1. Introduction

The State-Specific Electron Diffraction (SSED) apparatus, shown schematically in **Figure 2.1**, was designed to complement the existing GED apparatus in Edinburgh by extending the range of species that can be studied by electron diffraction. This was to be achieved by combining a number of state-of-the-art technologies. The cornerstone of the apparatus, in terms of extending the scope of GED, is the supersonic molecular beam (**Section 2.3**), which will cool the majority of molecules down to their ground vibrational state. Provision has been made for the inclusion of a laser, which could excite molecules to higher vibrational and electronic states. Hence, the name SSED comes from the vision of obtaining the molecular structure of a specific vibronic state, in contrast to conventional GED, where the structure is obtained from the ground electronic state averaged over all populated vibrational states.

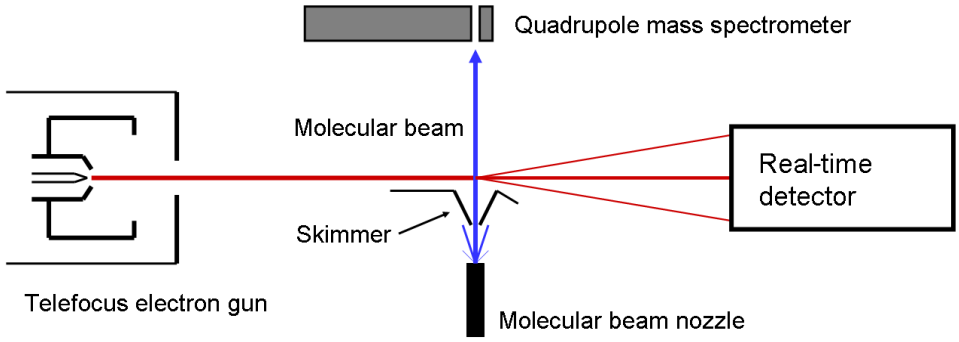

Figure 2.1 – Schematic of the Edinburgh SSED apparatus.

The remaining components are, to some extent, included in order to facilitate the goal of observing specific vibronic states, although the range of potential applications (**Section 2.5**) is much broader. The inclusion of a mass spectrometer is crucial as it will enable the components of the molecular beam to be observed and tuned during the course of an experiment. The species observed in the beam may include dimers and other clusters, which may or may not be desirable depending on the specific experiment. The electron beam (**Chapter 3**) is produced using a

telefocus electron gun that is capable of providing electron-beam intensities of up to 100 μA, which should help to compensate for the lower molecule densities expected in the molecular beam. The electron detection (**Section 2.3**) is performed online, which will enable the experiment to be optimised far more easily as the apparatus need not be opened in order to view results. In addition, it bypasses the time-consuming step of developing film.

2.2. Layout of the apparatus and differential pumping scheme

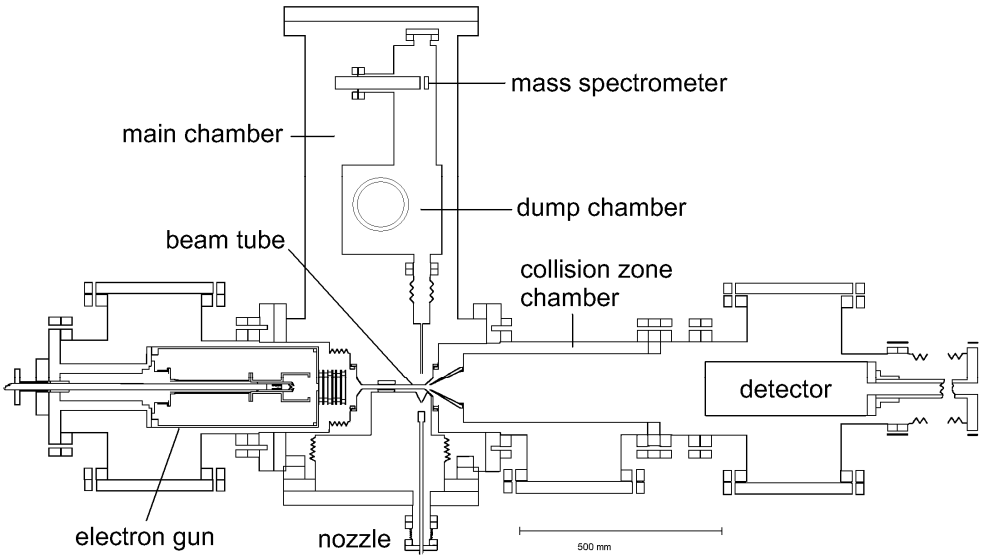

Figure 2.2 – Scale drawing of the SSED apparatus.

The SSED apparatus is divided into six chambers, as can be seen in **Figure 2.2**. The electron beam passes through the electron gun chamber, the collision zone and the detector chamber, each of which is pumped by an oil diffusion pump with a liquid nitrogen baffle to prevent oil coating surfaces near the electron beam. The main chamber and the dump tank (containing the mass spectrometer and into which the molecular beam is directed) are also individually pumped by oil diffusion pumps, but do not require liquid nitrogen baffles as they are separated from the electron beam path. Finally, the nozzle chamber (which can be removed if the supersonic beam is not in use) is pumped by a Roots blower, backed by a large rotary pump, which can

provide high pumping speeds required for the large volumes of gas produced during the operation of the molecular beam.

The chambers are not completely separated, but are joined by small openings at or near the beam tube (a selection of which are shown in **Figure 2.3**), as shown by the dotted lines in **Figure 2.4**. The sizes of the openings mostly depend on the beam tube in use and, with the exception of the skimmer aperture, range from a couple of square-millimetres to a few square-centimetres.

Figure 2.3 – Beam tubes (left) and skimmer box (right) used in the SSED apparatus. The beam tubes are (from left to right) one containing two copper collars for centring the electron beam, one with an open collision zone and one made of mu-metal with an attachment used to fasten it to the skimmer box

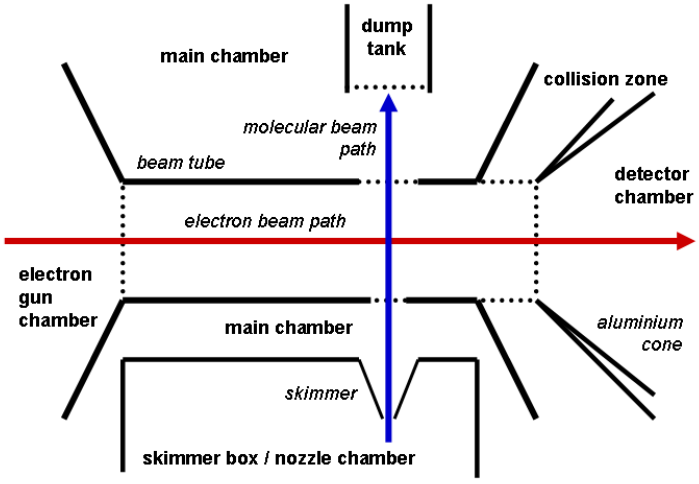

Figure 2.4 – Hypothetical boundaries (dotted lines) of the six chambers (bold text).

2.3. Online electron detection

2.3.1. Previous detection systems

So far the Achilles heel of the set-up has been the electron detection method. The original system was built by Integrated Sensors Limited (ISL) and was tested by Robert Fender.[1] The detector consisted of a pair of microchannel plates that were stacked on top of a collector anode. The anode itself was composed of 83 concentric gold rings, 0.3 mm wide with a spacing of 0.1 mm, each of which was divided into two semi-circles. These were mounted on an alumina ceramic wafer with a 6 mm hole at its centre, through which the undiffracted beam could pass. The counting circuitry was mounted on the underside of the ceramic wafer. After a succession of problems, the main one being static damage, the device was eventually abandoned as it was deemed too fragile to cope with the conditions in the apparatus.

The second detection method was more successful and was installed and tested by Paul Papathomas.[2] This time the electron diffraction pattern was converted to a visible pattern using a phosphor screen, mounted on a quartz view port. The pattern was recorded using an external CCD camera. Two types of phosphor were used, an inorganic one (P22G) and an organic one (NE102A), each of which were coated with a layer of aluminium, 50 and 100 nm thick, respectively, in order to prevent charge build-up. The CCD camera was bought from Princeton Instruments and contained a Scientific Grade 1 CCD made by SITe, whilst the lens used was either a Nikkor 85 mm /f1.8 or Micro-Nikkor 55 mm /f2.8 lens, depending on the distance from the screen. In some cases an optical filter was inserted between the phosphor and the quartz window.

Using this set-up, data were collected for CF_4 and 1,2,4,5-tetrafluorobenzene and structure refinements were attempted. CF_4 data collected without the filter were of reasonable quality and yielded an *R* factor of 12%. The addition of the filter would be expected to improve the quality of the data. However, the diffraction patterns

appeared asymmetric and despite adopting four different methods of data correction an improvement in the fit was not obtained. Data for tetrafluorobenzene were obtained using the filter and again appeared more intense on one side than the other. In this case the agreement between theoretical and experimental curves was worse than for CF_4 and the mean C–C bond length refined to about 4 pm shorter than expected. At this point it was realised that there was a problem with the data, although it was unclear whether this arose in the collection stage or in its treatment afterwards. Statistical analysis revealed that the signal-to-noise ratio was not a problem so Papathomas suggested the problem originated in the argon calibration.

2.3.2. The new CCD camera

The impetus for much of the work described in this thesis was provided by the acquisition of a new detector (**Figure 2.5**) from the X-ray imaging company, Rigaku, who used it as a prototype in the development of their Mercury 2 CCD detector.

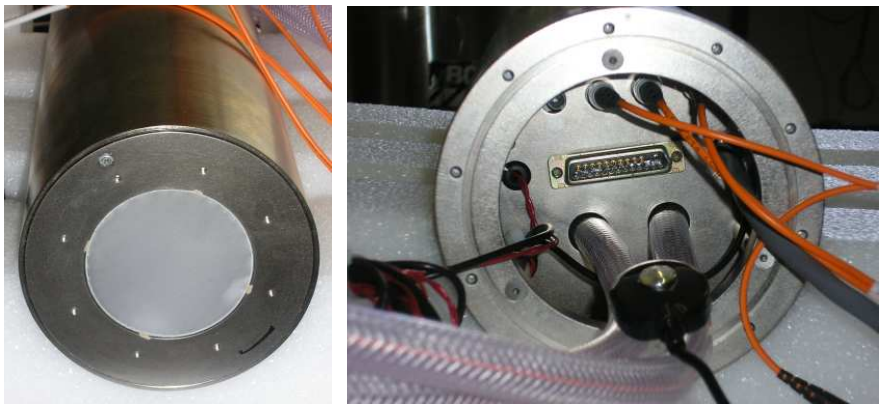

Figure 2.5 – The new detector as viewed from the front (left) and the back (right).

As was the case for the previous detection method, the new detector works by imaging the diffraction pattern produced by a phosphor screen onto a CCD. The phosphor is terbium-doped gadolinium oxysulfide (GdOS:Tb), as is often used in X-ray detectors, coated with a 50-70 nm layer of aluminium. Both the phosphor and a graded neutral-density filter were deposited directly onto a fibre optic faceplate, which is optically coupled to the CCD using a fibre-optic taper (3.17 : 1), rather than

using a lens as was the case in the previous detector. In theory, this allows all the light produced by the phosphor to reach the CCD, significantly increasing the sensitivity of the new setup. The CCD is an array of 1024×1024 pixels, 24 μm wide, and the active region of this array is circular with a centre approximately coincident with the centre of the array and a diameter approximately equal to 1024 pixels. In contrast to the previous camera, the detector is mounted inside the apparatus, although only the outside of the detector is at high vacuum. The CCD is maintained at about –40°C by thermoelectric cooling and is therefore sealed in an evacuated chamber (~ 1 mbar) with the fibre optics to prevent condensation. The electronics that control the CCD are contained in the detector at atmospheric pressure, but are powered by an external power supply and operated remotely from a desktop PC using fibre-optic transmission.

2.4. The supersonic molecular beam

Supersonic molecular beams (sometimes also called nozzle beams) are used extensively in spectroscopy, as the low temperature and lack of inter-molecular collisions characteristic of such beams simplifies the analysis of the data. They have also been widely used in crossed-beam experiments as the high velocity of the mass flow and narrow distribution of velocities (to which the translational temperature refers) in such a beam makes it ideal for the study of molecular collisions.

They were first proposed by Kantrowitz and Grey[3] as a method of producing a collimated molecular beam with a much greater intensity than was previously attainable. In a conventional beam the intensity was limited by the rate of effusion through the first slit (see **Figure 2.6**). This is because increasing the pressure of the gas supply reduces the mean free path of the gas molecules and when this becomes less than the orifice diameter, free molecular flow is lost, reducing the gas density at the second collimating aperture.

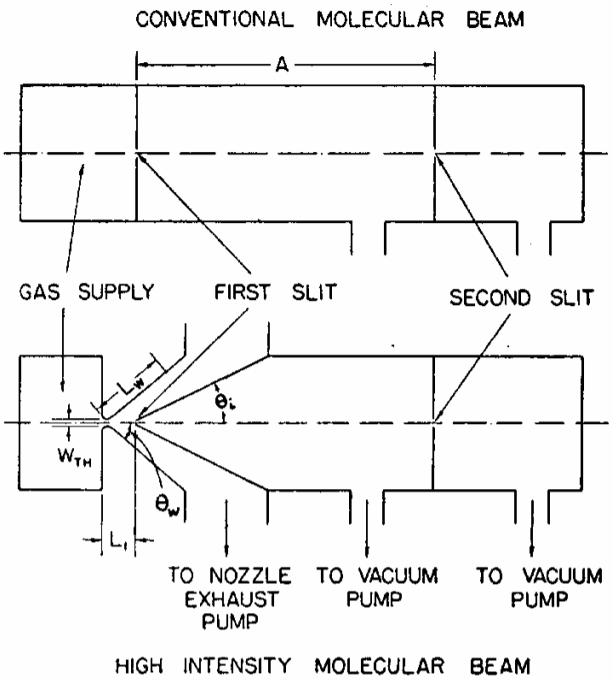

Figure 2.6 – Comparison of Kantrowitz and Grey's high-intensity molecular beam with a conventional type of collimated beam (Ref. 3).

Kantrowitz and Grey's proposal was to place the first opening in the flow from a supersonic nozzle, which would provide some collimation of the beam before it reaches the second slit. In this method free molecular flow is established as the supersonic expansion is skimmed at the first slit, so there is no loss of intensity due to a cross-over of flow regimes as the gas pressure is increased. In addition, as the beam is partially collimated at the first slit, the loss of intensity between the first and second slits is much less for a nozzle beam than for a conventional molecular beam.

This design was tested by Kantrowitz and Grey's colleagues, Kistiakowsky and Slichter,[4] who found that the provision of enough pumping capacity was critical to its implementation. Within a few years Becker and Bier[5] showed that a supersonic nozzle could successfully be used as a source of a molecular beam.

2.4.1. The use of supersonic molecular beams in GED

Supersonic molecular beams of the type proposed by Kantrowitz and Grey have previously been combined with electron diffraction in the investigation of the structures of clusters, but have not yet been used to obtain molecular structures of comparable accuracy to those obtained by traditional GED.

The first investigations of supersonic beams were performed by Raoult and Farges,[6] who found that the greatest difficulty in combining the technologies was that the density of a supersonic molecular beam is two to three orders of magnitude lower than that conventionally used in GED. (Given the historical impetus for the invention of molecular beams this may seem counter-intuitive. However, in a GED experiment the beam density is not lowered by collimation and, as was noted by Bartell,[7] the conventional GED nozzle source is a free expansion rather than an effusive source, although too few intermolecular collisions occur for the associated cooling to be noticed.) The extraneous scattering therefore had to be reduced by the same amount. This was done by reducing the electron scattering from the beam stop and lowering the background pressure to 5×10^{-8} Torr using cooled active charcoal surfaces and a liquid helium cryostat. In addition, the beam source was modified to be less bulky than the classical Campargue-type design[8] in order to allow the scattering point to be as close as possible to the nozzle.

A significant amount of optimisation of the gas delivery system for obtaining clusters has been performed by Bartell,[7] although the nozzle type adopted was not strictly that proposed by Kantrowitz and Grey, as no collimating (second) slit was used. However, this enabled the supersonic molecular beam to be used in conjunction with a conventional GED apparatus, the only modifications being a lengthening of the beam stop from 20 to 60 mm and a faster diffusion pump. (Unfortunately, no details of the subsequent improvement were given.) The optimisation included testing three shapes of skimmer (**Figure 2.7**), three types of sources (thin plate, tubular and tapered glass nozzles), and variation of the pressure and composition of the gas.

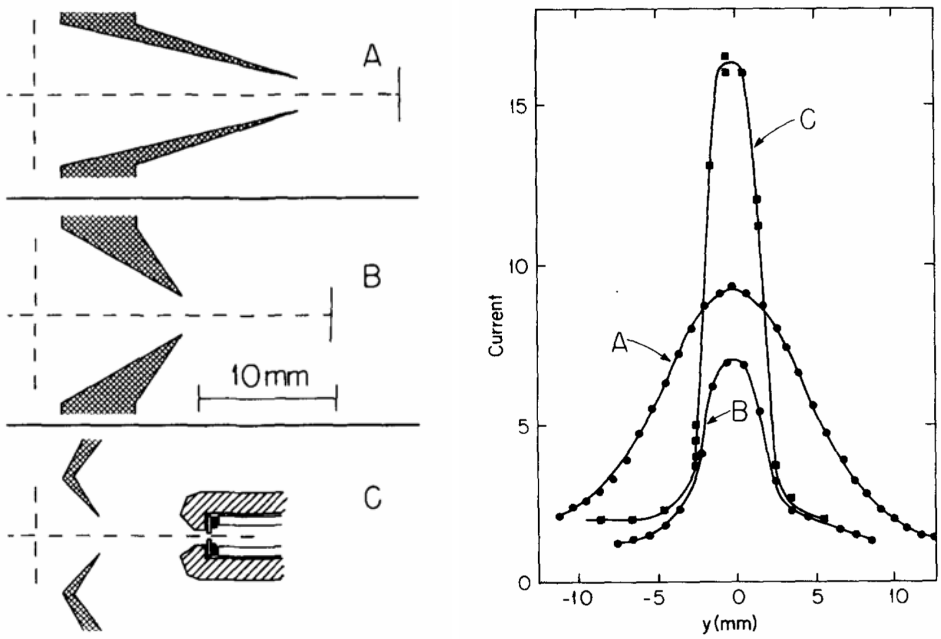

Figure 2.7 – Skimmer shapes tested by Bartell (left) and the recorded current scattered by *n*-pentane in helium as a function of the lateral displacement of the supersonic nozzle (right). The dashed vertical line indicates the electron beam position and the solid vertical line is the nozzle position, which was 7, 11 and 8 mm from the skimmer entrance in A, B and C, respectively (Ref. 7).

Bartell also investigated the use of pulsed, skimmed supersonic beams and modified the apparatus accordingly as shown in **Figure 2.8**.[9] The main alteration is the use of a pulsed electron beam (achieved by electrostatic deflection), which is synchronised with the pulsed molecular beam. However, it also makes use of a glass Laval nozzle, which is one with a curved, tapered throat and has been shown to increase beam intensities and cluster formation rates.[10] In addition, the conical shaped skimmers shown in **Figure 2.7** were replaced by a V-shaped skimmer, in order to position the skimmer entrance as close as possible to the electron beam.

A final notable achievement regarding the use of supersonic molecular beams is the work of Yokozeki in Gilbert Stein's laboratory, who used the nozzle in **Figure 2.9** to obtain data for lead microclusters.[11] Inspired by this work, Monot built a similar apparatus, the nozzle (**Figure 2.10**) for which was based on Yokozeki's design, and used it to study silver clusters.[12]

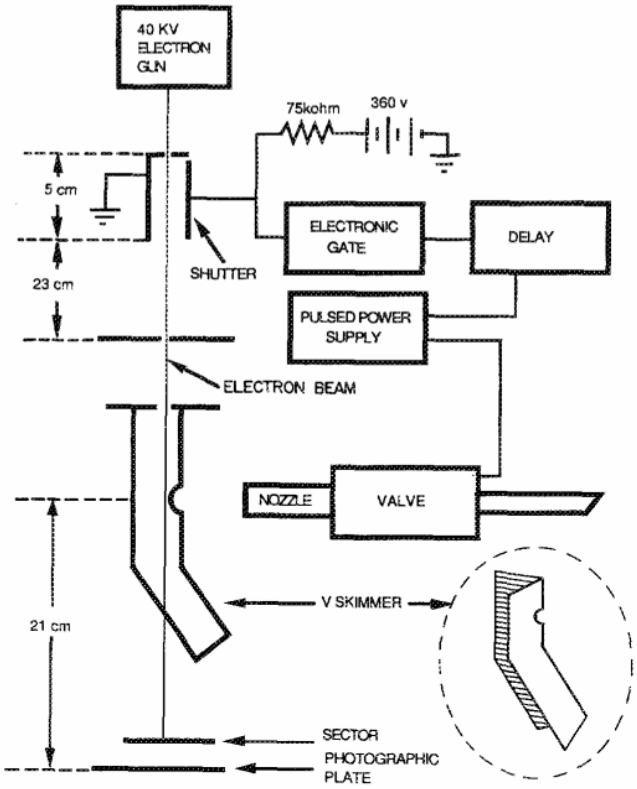

Figure 2.8 – Schematic of Bartell's apparatus for use with pulsed molecular beams. (Ref. 9).

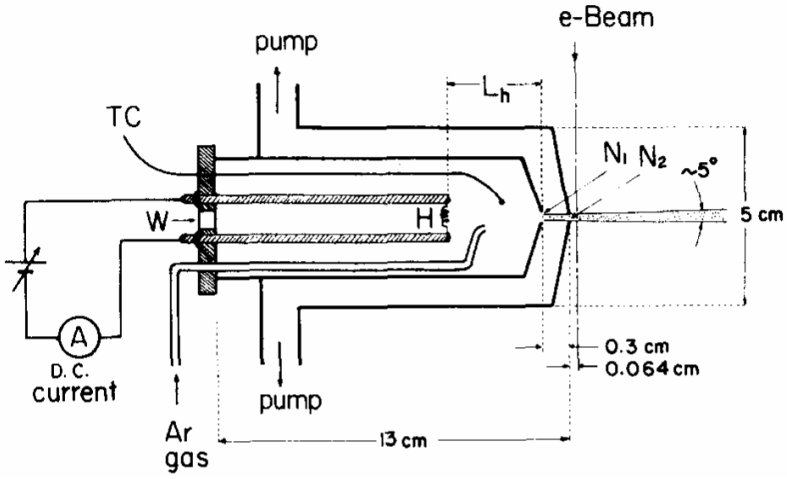

Figure 2.9 – Yokozeki's nozzle (reference 11).

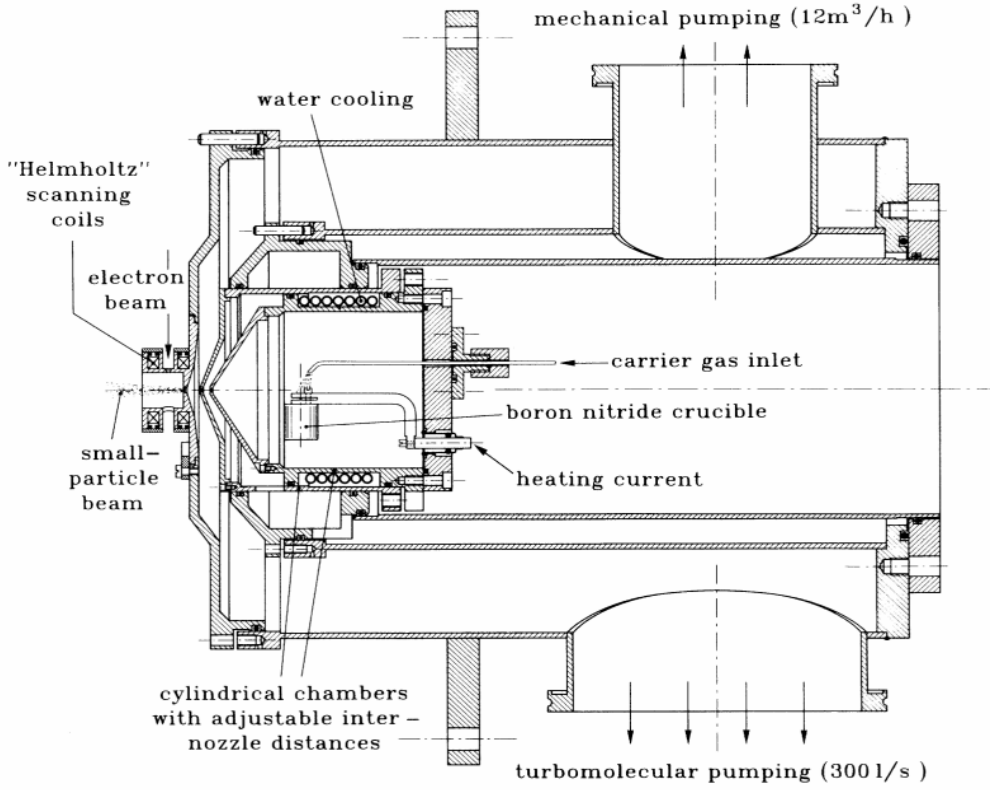

Figure 2.10 – Monot's molecular beam source (Ref. 12).

2.4.2. Supersonic expansion theory

The type of flow that occurs when a gas is expanded into a vacuum is determined by its Knudsen number, K_n. This is given by the ratio of the mean free path in the reservoir, λ_0, to the nozzle diameter, D, as shown in **Equation 2.1**.

$$K_n = \frac{\lambda_0}{D} \tag{2.1}$$

For $K_n > 1$ the gas flow is effusive and the constituent molecules have the same temperature as in the reservoir, whilst for $K_n < 1$ collisions between molecules after they exit the nozzle enables their internal energy to be converted into kinetic energy

in the direction of the beam, although significant cooling is not observed unless K_n << 1. As the gas expands, any molecules moving with high velocity components perpendicular to the electron beam either leave the beam axis or are scattered back into the beam with a lower perpendicular velocity. At the point of skimming, the molecules have a high velocity component in the direction of the beam, but very low relative velocities, corresponding to translational temperatures approaching 1 K.

Molecular beams are often characterised in terms of their Mach number, *M*, which is given by **Equation 2.2**, where *u* is the mass flow velocity and *c* is the local speed of sound.

$$M = \frac{u}{c} \tag{2.2}$$

Clearly *u* increases in the expansion process, but the high Mach numbers quoted for supersonic beams are largely due to the reduction in *c*. The speed of sound can be related to the temperature, *T*, of an ideal gas by **Equation 2.3**, where γ, the adiabatic ratio, is that of the heat capacity at constant pressure to constant volume, *P* is the pressure, ρ is its density, k_B is the Boltzmann constant and *m* is the molecular mass.

$$c = \sqrt{\frac{\gamma P}{\rho}} = \sqrt{\frac{\gamma k_B T}{m}} \quad \text{where } \gamma = \frac{C_P}{C_V} \tag{2.3}$$

The region of the expansion where $M > 1$ is called the zone of silence and at the edges of this severe temperature and pressure gradients are present. The boundary of the zone of silence in the absence of a skimmer is indicated by the dashed line in **Figure 2.11**.

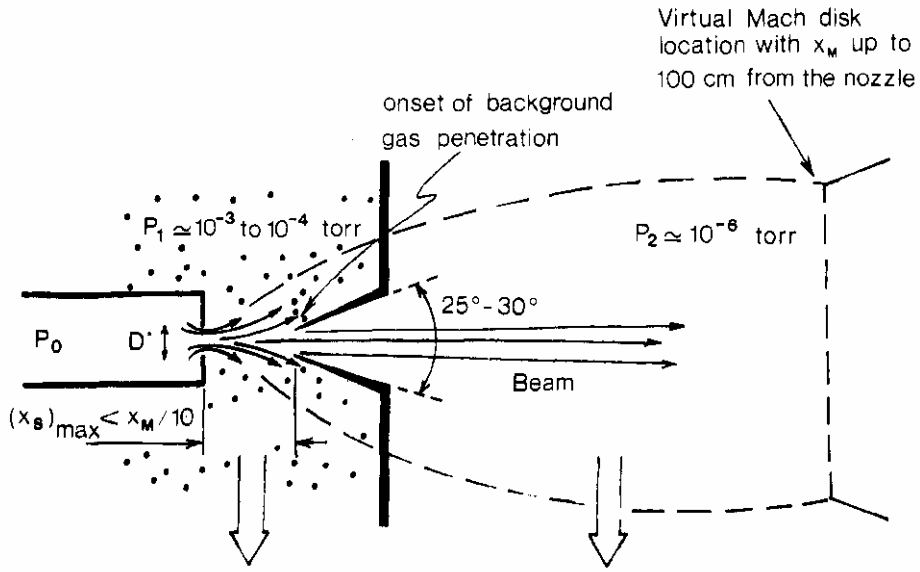

Figure 2.11 – Skimmed supersonic molecular beam (taken from reference 13).

The end of the zone of silence is called the Mach disk and its position, x_m, can be calculated using **Equation 2.4**,[13] where P_0 and P_1 are the pressures in the nozzle and skimmer chamber, respectively. The ideal placement of the skimmer is not at the Mach disk, however, as the collision frequency drops sufficiently for the transition from continuum flow to free molecular flow to occur at a nozzle-to-skimmer distance, $x_s < x_m / 10$.[13]

$$x_m = 0.67D\sqrt{\frac{P_0}{P_1}} \tag{2.4}$$

2.4.3 Thermodynamics relating to supersonic beams and SSED

If we assume that the background pressure is zero no work is done by a supersonic expansion and, as it is also effectively thermally isolated from its surroundings, it can be considered to be adiabatic. In addition, the increase in entropy due to the increase in volume and energy in the direction of the beam is balanced by a drop in entropy due to cooling, thus the expansion is also isentropic.

The temperature of a molecular beam is a somewhat abstract concept as the system is far from thermal equilibrium. As the redistribution of energy takes place at different rates for each degree of freedom it makes sense to quote a separate temperature for the translational, rotational and vibrational motion. The translational temperature is defined in terms of the width of the velocity distribution in the skimmed beam whilst the rotational and vibrational temperatures are those that would be used in a Boltzmann distribution (**Equation 2.5**) to reproduce the population of states.

$$\frac{n_i}{N} = \frac{\exp\left(-\frac{E_i}{k_B T}\right)}{q} \qquad \text{where} \quad q = \sum_i \exp\left(-\frac{E_i}{k_B T}\right) \tag{2.5}$$

In a typical supersonic beam the respective temperatures for translational, rotational and vibrational motion are generally around 1, 10 and 100 K. However, for SSED we would like to know the proportion of molecules in the ground vibrational state, v_0. If we assume that, for a given normal mode, the vibrations are harmonic, the spacing of energy levels corresponding to that mode will be constant, ΔE. The partition function, q, can be simplified to that shown in **Equation 2.6**. The fraction of molecules in the ground state is therefore given by **Equation 2.7** and is plotted against T/ν ($\nu = E/hc$) in **Figure 2.12** along with q and the populations of the first and second excited vibrational states.

$$q = \frac{1}{1-\exp\left(-\frac{\Delta E}{k_B T}\right)} \quad \text{since} \quad \sum 1 + x + x^2 + x^3 \ldots = \frac{1}{1-x} \tag{2.6}$$

$$\frac{n_0}{N} = \frac{1}{q} = 1 - \exp\left(-\frac{\Delta E}{k_B T}\right) \tag{2.7}$$

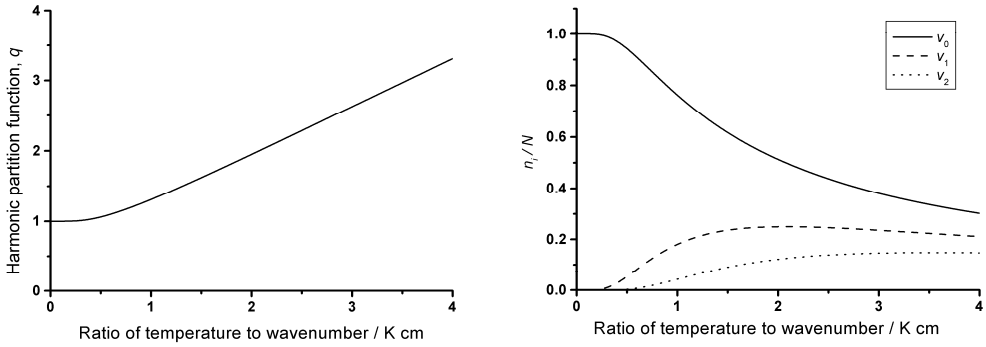

Figure 2.12 – Dependence of the partition function (left) and the population of vibrational states (right) on the ratio of temperature to vibrational frequency.

From **Figure 2.12** the population of v_0 drops below 95% when the temperature, T (in Kelvin) is greater than about half the vibrational wavenumber, v (in cm^{-1}). Therefore, molecules with a lowest frequency of vibration greater than 200 cm^{-1} are likely to be predominantly in their ground vibrational state.

2.5. Potential applications and limitations of the apparatus

The unique setup of the apparatus allows four areas to be studied that are inaccessible to conventional GED:

1. Compounds with low volatility.

2. Molecules in their ground vibrational state.

3. Weakly associated dimers.

4. Unstable species using laser excitation.

2.5.1. Low volatility compounds

Compounds with low volatility are difficult to study due to the low signal-to-noise ratio and extended exposure times required. The layout of the apparatus (**Section 2.2**) results in a low background pressure along the path of the electron beam (approximately 10^{-6} mbar in the electron gun chamber and 10^{-7} to 10^{-8} mbar in the collision zone and detector chambers) and should therefore reduce the background gas scattering. However, further modifications such as an efficient cold trap and an electron beam skimmer immediately in front of the scattering point, as are found in conventional apparatuses are still required. In addition, further optimisation of the beam stop (**Sections 3.3** and **5.2.2**) is required to reduce the extraneous scattering from this source.

The telefocus electron gun and the online detection system are also important for solving this problem. The combination of a high-intensity electron beam and the high sensitivity of the camera will allow data to be collected at much shorter exposure times. In addition, the ability to view the data immediately after exposure will allow the experimental conditions to be optimised far more easily than if photographic detection is used.

2.5.2. Investigation of molecules in low or ground vibrational states

In conventional GED accounting for vibrational motion is one of the largest sources of uncertainty and for some molecules even prevents reasonable structures being obtained. Cooling molecules using a supersonic molecular beam is therefore useful for two reasons: it reduces the effect of vibrations on the electron diffraction data, which would manifest itself in a sharpening of the peaks in the radial-distribution curve, and reduces the size of the distance corrections applied to the GED model when extrapolating to a static structure. However, the smaller available data range and the lower molecule densities in the molecular beam may counterbalance these potential benefits.

2.5.3. Investigation of dimers and clusters

As mentioned in **Sections 1.3.2** and **2.4.1** the observation of the structures of clusters has been the main application of the use of supersonic molecular beams in GED. This field has not been exhausted, however, and the incorporation of a mass spectrometer in the set-up may help to fine-tune the components of the molecular beam. However, a related area that could be extended using a supersonic molecular beam and has been investigated much less widely is that of hydrogen-bonded dimers and other weakly bound dimers.

Only four hydrogen-bonded dimers have been characterised by GED. The structures of the monomers and dimers in the series of carboxylic acids, methanoic acid,[14] ethanoic acid[15] and propanoic acid[16] have been studied, as has the structure of the dimethylphosphinic acid dimer $(Me_2P(=O)OH)_2$.[17] The data for the monomers of methanoic, ethanoic and propanoic acid were obtained at 175, 160 and 215°C, respectively, whilst those for the dimers were collected at 12, 24 and 55°C. In the case of propanoic acid the dimer could not be isolated and a mixture of monomer and dimer was refined. For dimethylphosphinic acid the monomer was not observed in the GED experiment, even at the experimental temperature of 433 K.

The effect of substituting hydrogen with deuterium in the hydrogen bond of the methanoic acid dimer has also been investigated using GED.[18] The investigators found small changes in the geometry of the carboxyl group, in particular an elongation of the C–O bond of 0.9 pm and a reduction in the O=C–O angle of 0.7°. However, they were also careful to point out that these differences were at the limits of the accuracy of the experiment and should be treated with caution. A more substantial finding was a lengthening of the O–H··O interaction of 1.9 pm, a value that was consistent with both the X-ray and neutron diffraction structures for α-oxalic acid dihydrate in the solid state.[19] The deuteration of the methanoic acid hydrogen bond therefore appears to synergistically affect the potential-energy surface of the

dimer. In contrast, the deuteration of methane, which was studied by Bartell,[20] showed only the expected reduction in amplitudes of vibration.

In light of these successes it seems strange that this work has not been followed up. This could be done using conventional equipment so long as the system to be studied has the correct thermochemical properties, but this constraint may be too great for larger systems with weaker hydrogen bonds, as they will require more heating to enter the gas phase. The cooling afforded by a supersonic expansion may therefore be required to provide access to such species. In addition, the presence of a mass spectrometer and the ability to observe diffraction patterns immediately should simplify the optimisation of the experiment.

An ambitious extension of the work mentioned above is to bimolecular species exhibiting complementary hydrogen bonding as found in DNA base pairing. The gas-phase Watson-Crick structures of base pairs have not yet been experimentally determined, although the structure of a base-pair mimic has been determined in a molecular beam using rotational spectroscopy[21] and numerous theoretical studies have been performed, including some thermodynamic analysis based on rigid-rotor, harmonic-oscillator and ideal-gas approximations.[22] Free base pairs can be formed in the gas phase using a combination of laser ablation and supersonic cooling and have been observed by time-of-flight mass spectrometry.[23] Moreover, the guanine-cytosine dimer has been characterised by resonance-enhanced multiphoton ionisation (REMPI) spectroscopy and appears to adopt a single conformation,[24] making it suitable for study by GED. However, the guanine-guanine dimer has also been observed as a major constituent of the molecular beam produced in this way, which would complicate the analysis. In addition, purines and pyrimidines have high melting and boiling points, so a high temperature nozzle would be required for such compounds, which may mean that this study would be out of the reach of applications for this apparatus. A more realistic goal would therefore be an investigation of base-pair analogues like 2-aminopyridine·2-pyridone as studied by Roscioli and Pratt using rotational spectroscopy.[21]

2.5.4. The use of laser excitation

Provision has been made in the design of the apparatus for incorporating a laser into the set-up. It is therefore possible to propose a number of exotic applications:

- unstable species produced by photolysis
- molecular ion structures using multi-photon ionisation
- excited vibrational states
- excited vibronic states

However, there are a number of challenges and important general considerations that have to be made if structures of these types of species are to be found. For all four of the categories above, the magnitude of the expected structural changes should be considered. Of critical importance, however, will be the proportion of the excited species in the gas beam, as in each case this is likely to be severely limited. Photolysis products have been characterised and the reactions even timed using strobed and time-resolved electron diffraction. However, in all cases pulsed lasers were used, providing higher photon intensities than a continuous source. Therefore, in order to study photolysis products, such high-intensity pulsed lasers may be required and the data collection, electron beam or molecular beam may have to be synchronised with the laser pulses. In multi-photon processes the cross-sections increase with photon intensity and species produced by this method, such as molecular ions, are more likely to require a pulsed laser source. The cross-sections for excitation to higher vibrational or electronic states are likely to be larger, but the stimulated emission of the absorbed radiation will create an upper limit on the proportion of such species in the molecular beam. In addition, the lifetimes of excited states ought to be considered as this will also affect their population.

Assuming data for these types of systems can be obtained, there exists the additional question of how to interpret them. Given that the reorganisation of vibrational energy may take place more slowly than the time between the species' generation and probing by the electron beam, these systems may no longer be characterised by Boltzmann energy distributions and the effect of vibrations in the theoretical treatment outlined in **Sections 1.4.2 and 1.4.4** will no longer be applicable. This problem has been considered in depth by those pursuing time-resolved or ultrafast electron diffraction (TRED / UED) and helpful reviews have been published by the collaboration of Ewbank, Schäfer and Ischenko[25] and by Zewail *et al.*[26,27] Both groups predict chaotic behaviour as a probable outcome for such systems, which may require the data analysis for non-Boltzmann structures to proceed by fitting probability distributions, rather than using a molecular model as in conventional GED refinements. However, despite these predictions the only experimental evidence of such behaviour has been the excessively 'hot' structure of cyclohepta-1,3,5-triene, which refined with root-mean-squared amplitudes of vibration three times greater than those predicted for a structure at 400 K.

2.6. References

1. R. S. Fender, Ph.D. thesis, *University of Edinburgh* (1996).
2. P. Papathomas, Ph.D. thesis, *University of Edinburgh* (1998).
3. A. Kantrowitz and J. Grey, *Rev. Sci. Instrum.* (1951), **22**, 328.
4. G. B. Kistiakowsky and W. P. Slichter, *Rev. Sci. Instrum.* (1951), **22**, 333.
5. E. W. Becker and K. Bier, *Z. Naturforsch.* (1954), **9**, 975.
6. B. Rault and J. Farges, *Rev. Sci. Instrum.* (1973), **44**, 430.
7. L. S. Bartell, R. K. Heenan and M. Nagashima, *J. Chem. Phys.* (1983), **78**, 236.
8. R. Campargue, *Rev. Sci. Instrum.* (1964), **35**, 111.
9. O. Abraham, J. H. Binn, B. G. DeBoer and G. D. Stein, *Phys. Fluids* (1981), **24**, 1017.
10. L. S. Bartell and R. J. French, *Rev. Sci. Instrum.* (1989), **60**, 1223.
11. A. Yokozeki, *J. Chem. Phys.* (1978), **68**, 3766.
12. B. D. Hall, M. Flüeli, R. Monot and J.-P. Borel, *Phys. Rev. B*, (1991), **43**, 3906.
13. R. Campargue, *J. Phys. Chem.* (1984), **88**, 4466.
14. A. Almenningen, O. Bastiansen and T. Motzfelt, *Acta Chemica Scandinavica* (1969), **23**, 2848.
15. J. L. Derissen, *J. Mol. Struct.* (1971), **7**, 67.
16. J. L. Derissen, *J. Mol. Struct.* (1971), **7**, 81.
17. L. S. Khaikin, O. E. Grikina, L. V. Vilkov, A. V. Golubinskii, E. G. Atavin, R. E. Asvin and G. S. Denisov, *J. Mol. Struct.* (2003), **658**, 153.
18. A. Almenningen, O. Bastiansen and T. Motzfelt, *Acta Chemica Scandinavica* (1970), **24**, 747.
19. R. G. Delaplane and J. A. Ibers, *Acta Cryst. B* (1969), **25**, 2423.
20. L. S. Bartell, K. Kuchitsu and R. J. de Neui, *J. Chem. Phys.* (1961), **35**, 1211.
21. J. R. Roscioli and D. W. Pratt, *Proc. Nat. Acad. Sci.* (2003), **24**, 13752.
22. P. Hobza and J. Šponer, *Chem. Rev.* (1999), **99**, 3247.
23. M. Dey, F. Moritz, J. Grotemeyer and E. W. Schlag, *J. Am. Chem. Soc.* (1994), **116**, 9211.
24. E. Nir, K. Kleinermanns and M. S. de Vries, *Nature* (2000), **408**, 949.
25. J. D. Ewbank, L. Schäfer and A. A. Ischenko, *J. Mol. Struct.* (2000), **524**, 1.

26. R. Srinivasan, V. A. Lobastov, C. Ruan and A. H. Zewail, *Helv. Chim. Acta* (2003), **86**, 1763.
27. D. Shorokhov, S. T. Park and A. H. Zewail, *ChemPhysChem* (2005), **6**, 2228.

Chapter 3

The electron beam

3.1. The telefocus electron gun

The Edinburgh SSED apparatus uses a telefocus electron gun (**Figure 3.1**). This is in contrast to many other experimental setups, where the electron beam is focused using lenses and apertures, as is the case in an electron microscope. Telefocus guns produce higher beam intensities than conventional electron guns, a factor which should compensate for the lower density of molecules found in supersonic molecular beams, another feature of the apparatus.

Figure 3.1 – Edinburgh telefocus electron gun, Wehnelt cylinder, Wehnelt cap and filament.

In both types of gun free electrons are generated by thermionic emission from a tungsten filament, which is maintained at a negative electrical potential of a few tens of kV. The electrons are accelerated towards an earthed plate (which acts as an anode) with a hole in its centre, through which the electron beam passes. The beam current is controlled by placing a shield containing a small hole over the filament. This is known as the Wehnelt cap and is at a slightly more negative voltage than the filament. The potential difference between the filament and the Wehnelt cap is known as the bias voltage. A typical circuit used to control such a triode system is shown in **Figure 3.2**.

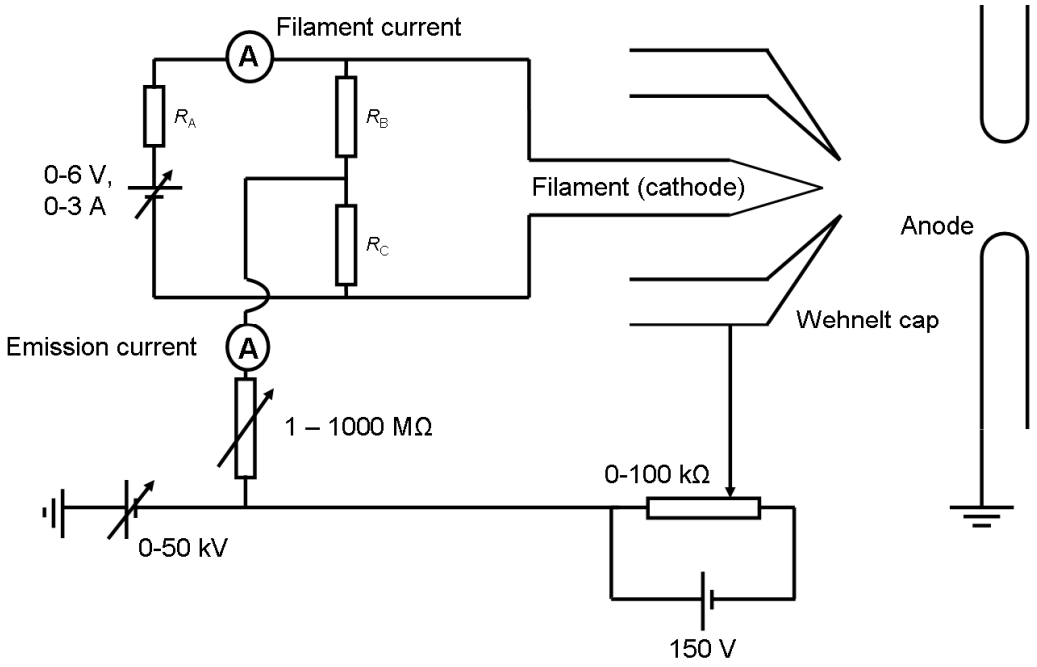

Figure 3.2 – Typical circuit diagram for control of a triode electron-gun system. Note how the emission current is measured. The emission current is always greater than the total beam current and, if the circuit is poorly insulated, the measured current will be greater than the current leaving the cathode. As long as $R_{\text{Filament}} << R_B = R_C$, the current in the filament is equal to that measured.

The two types of electron gun differ in the way they focus and steer the electron beam. As in an electron microscope, a traditional gun employs a series of magnetic lenses and apertures to obtain a narrowly focused beam, which is then steered magnetically to the point of interest. In a telefocus gun both the focusing and the steering of the electron beam are performed electrostatically. The electric field between the filament and the anode is manipulated by placing a metal Wehnelt cylinder (**Figure 3.1**) around the axis of the beam, in contact with the Wehnelt cap. The resulting electric field acts as a continuous series of lenses, as shown schematically in **Figure 3.3**, so that the beam can be focused by altering the distance between the filament and the anode, in a similar manner to the focusing of a telescope. This setup ensures that a minimal proportion of the electrons leaving the filament is lost as they reach the anode, whilst the absence of narrow apertures

ensures that most of the electrons exiting the anode are contained in the resulting electron beam, and there should be no background caused by deflection of electrons by the edges of apertures. The drawbacks of the telefocus gun compared to the electron-microscope type are a loss of ease with which the beam can be focused and a generally wider beam. For a more detailed description of the theory behind the focusing of telefocus electron guns reference 1 is recommended, whilst an overview of their use in GED and details specific to the Edinburgh telefocus gun are documented in references 2 and 3.

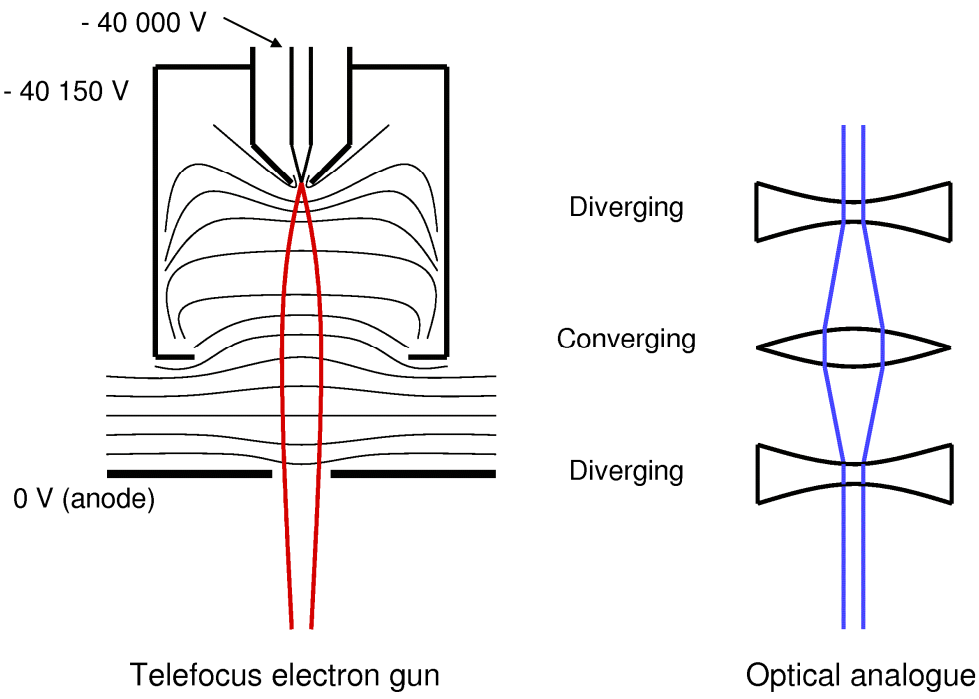

Figure 3.3 – Schematic diagram of a telefocus electron gun showing equipotential lines and its optical analogue.

3.2. Electron beam characteristics

Since it is not possible to observe an electron beam directly it is useful to know as much as possible about how the electron beam should behave theoretically. This will help to interpret the measured currents used to align the beam (**Section 3.4**) and characterise its width and profile shape (**Section 3.5**).

3.2.1. Electron mass and velocity

In order to calculate how the electron beam ought to behave under the influence of electric and magnetic fields, the velocity and mass of the electrons must be known. To calculate these using classical mechanics the rest mass of an electron (m_e) is used and the velocity (v) is obtained by equating the potential of an electron as it leaves the filament (eV) with its kinetic energy in the electron beam (**Equation 3.1**) and solving for v (**Equation 3.2**).

$$eV = \tfrac{1}{2} m_e v^2 \tag{3.1}$$

$$v = \sqrt{\frac{2eV}{m_e}} \tag{3.2}$$

Substituting a value of 40 kV for the accelerating voltage yields a velocity of 1.326×10^8 m s^{-1}, which is approaching the speed of light, and so a relativistic approach ought to be used. The electron mass, m, can be found by solving **Equation 3.3**, where c is the speed of light. The relativistic velocity can then be found by substituting **Equation 3.4** into **Equation 3.3**, and solving for v (**Equation 3.5**). **Figure 3.4** shows the classical velocity and the relativistic mass and velocities as functions of the accelerating voltage.

$$eV = mc^2 - m_e c^2 \tag{3.3}$$

$$m = \frac{m_e}{\sqrt{1 - \frac{v^2}{c^2}}} \tag{3.4}$$

$$v = c\sqrt{1 - \frac{m_e^2}{(m_e + \frac{eV}{c^2})^2}} \qquad (3.5)$$

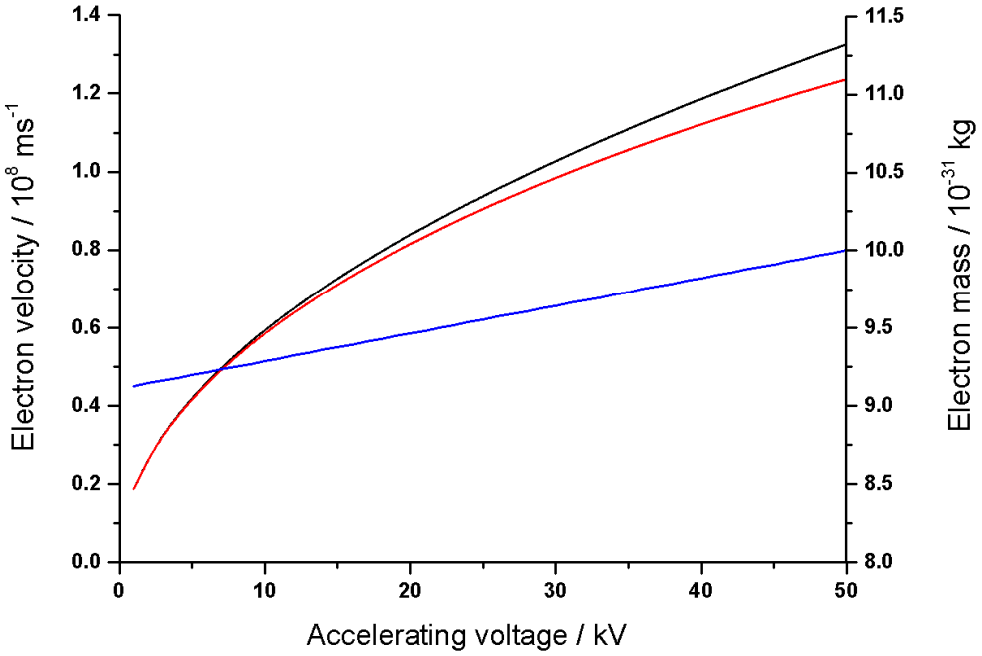

Figure 3.4 – Classical and relativistic electron velocities (black and red, respectively) and relativistic electron mass (blue) plotted as a function of the accelerating voltage.

3.2.2. Magnetic deflection

An electron moving in a magnetic field (**B**) experiences a force (**F**) according to **Equation 3.6**, where *e* is the charge on an electron and **v** is its velocity.

$$\mathbf{F} = e\mathbf{v} \times \mathbf{B} \qquad (3.6)$$

The Edinburgh SSED apparatus is situated so that the beam runs approximately west to east. The direction of the earth's magnetic field is therefore approximately perpendicular to the electron beam, upwards and to the left (as the electron travels).

Bearing in mind the negative charge on electrons, the force would have a component downwards and a component right to left. If we assume that the direction of this force is constant (*i.e.* the beam curvature is small), the magnitude of the displacement, *s*, due to magnetic deflection can be calculated using simple equations of motion, as shown in **Equation 3.7**, where *t* is the time taken to travel a distance, *l*, and *B* is the strength of the magnetic field.

$$s = \tfrac{1}{2}at^2 = \tfrac{1}{2}\frac{F}{m}t^2 = \tfrac{1}{2}\frac{eBl^2}{mv} \qquad (3.7)$$

The solutions of **Equation 3.7** for a uniform field of 0.3 Gauss (in SI units = 3×10^{-6} T), which is an approximate value for the earth's magnetic field, are shown in **Figure 3.5**:

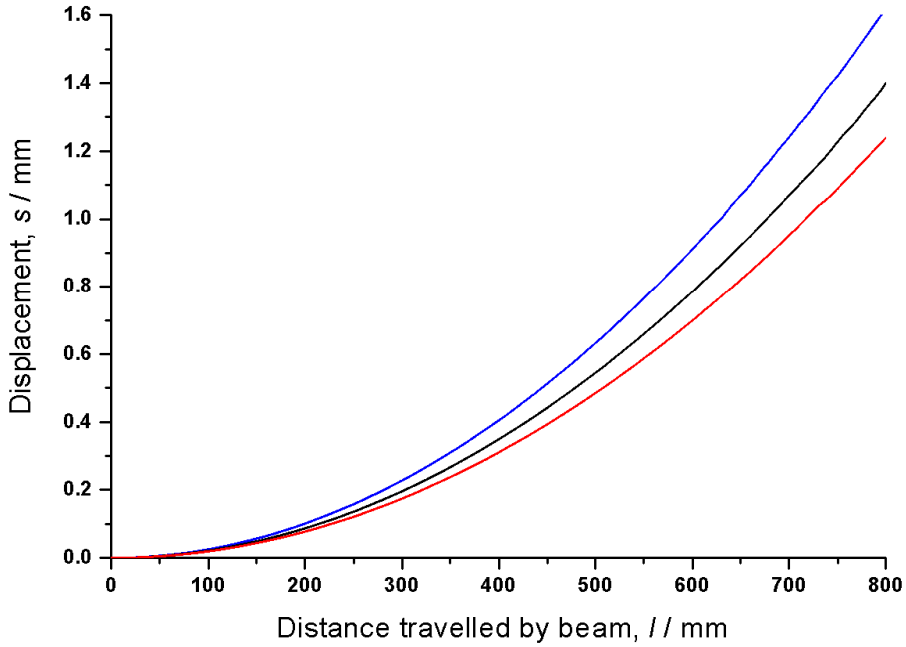

Figure 3.5 – Magnetic deflection of an electron beam by a uniform field of 3×10^{-6} T at 30, 40 and 50 keV (blue, black and red, respectively).

The intersection of the electron and molecular beams occurs at approximately 250 mm from the anode, by which point the electron beam will have moved about 0.14 mm. The minimum nozzle-to-camera distance is about 110 mm, over which it will be displaced a further 0.13 mm. At a typical 'long' nozzle-to-camera distance of 300 mm the total displacement will be about 0.65 mm, a displacement of about 0.5 mm from the nozzle position.

3.2.3. Steering by electrostatic deflection

The electron beam can be steered using four pairs of deflector plates (shown in **Figure 3.1**, and more closely in **Figure 3.6**). The first pair of deflector plates is for controlling the horizontal deflection and the second pair is for vertical deflection. Both pairs are controlled by the high-voltage electron-gun supply, which maintains each plate at an equal but opposite potential to its partner in the range ±200 V. A short spacer separates these from the two remaining pairs of plates, the first pair of which is again positioned for horizontal deflection and the second pair for vertical deflection. These two pairs of deflector plates, positioned further from the filament, are controlled by four Keithley power supplies, which provide up to ±2000 V for each plate.

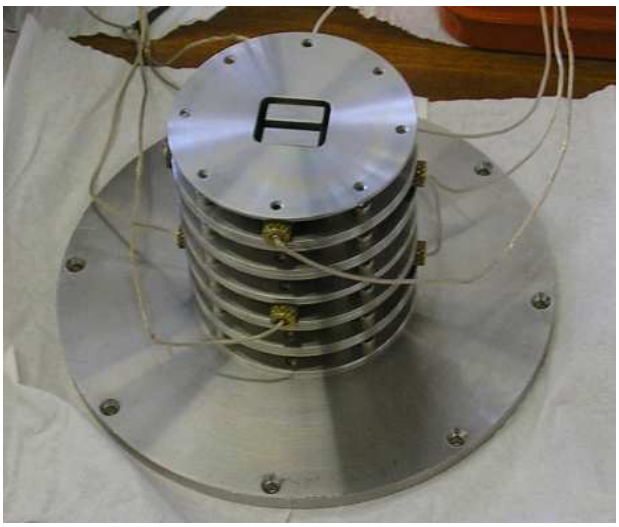

Figure 3.6 – Deflector plates positioned on top of the anode.

An estimate of the electron-beam deflection, s_{elec}, can be calculated using **Equation 3.8**, where E is the electric field strength (assumed to be uniform), V is the potential difference between a pair of plates, d is the spacing of the plates, L is the distance travelled after deflection, l is the length of the electric field along the electron beam path and t is time.

$$s_{elec} = \text{velocity induced by } E \times \frac{L}{v} = \frac{eEt}{m}\frac{L}{v} = \frac{eVlL}{mv^2 d} \tag{3.8}$$

The dimensions and spacing of the plates are shown in **Figure 3.7** and these values were used to calculate the solutions to **Equation 3.8**, which are shown in **Figure 3.8**. The electric field was assumed to be 10% longer than the deflector plates as it does not immediately fall to zero outside the region between the plates.

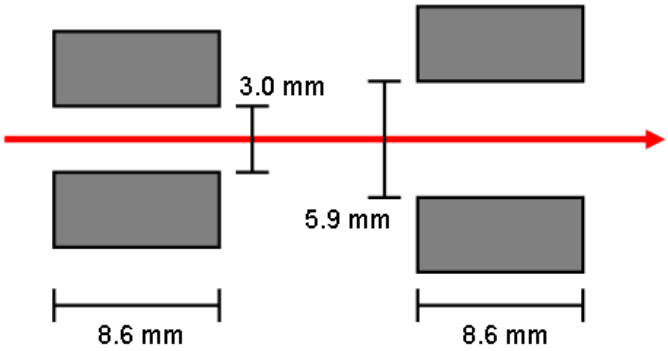

Figure 3.7 – Deflector plate dimensions used in calculations.

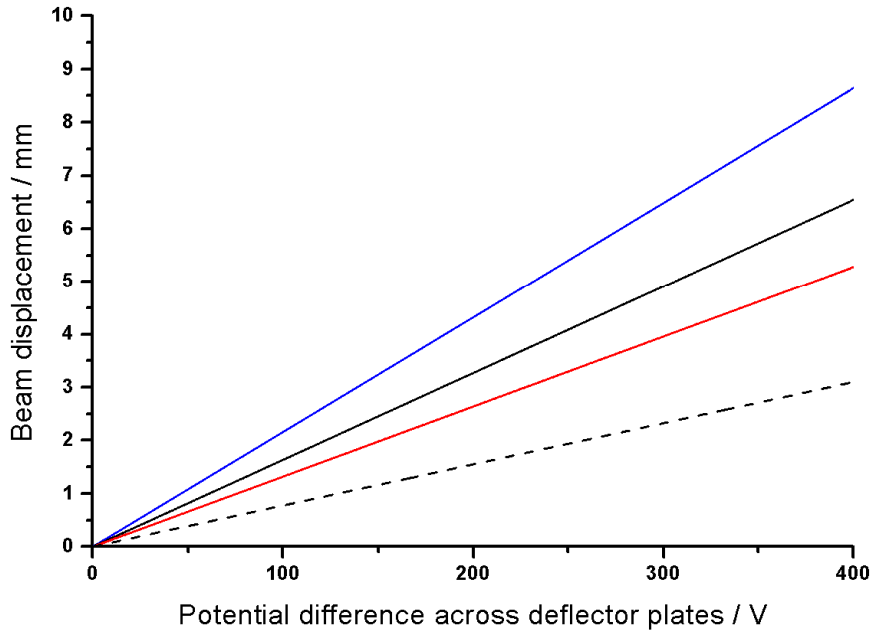

Figure 3.8 – Calculated beam displacement at a nozzle-to-camera distance of 200 mm for 30, 40 and 50 keV electron beams (blue, black and red respectively). Solid lines are used for the first and second pairs of deflector plates, for which the distance to the nozzle was assumed to be 240 mm. The dashed line is for the third and fourth pairs, assumed to be 30 mm closer to the nozzle for a 40 keV beam.

3.3. New beam stop and Faraday cup design

A beam stop and phosphor screen setup (**Figure 3.9**) had previously been used in the SSED apparatus by Paul Papathomas[3] and was useful for the initial alignment of the electron beam (**Section 3.4**). However, as the new camera could not accommodate the existing beam stop and Faraday cup a new beam stop had to be designed.

Figure 3.9 – Previous beam stop and aluminium-coated phosphor screen mounted on a re-entrant tube.

3.3.1. Lessons from the previous design

The previous beam stop served as a starting point for the new design as it successfully performed the three main functions that were required of it, namely:

1. it stopped the unscattered beam, which would otherwise burn out the phosphor and saturate the CCD,
2. it enabled the centre of the beam to be found,
3. it enabled the size and shape of the beam to be estimated.

Despite the success of the previous design in performing these tasks, there were also some severe problems with its design.

The initial concern was the physical instability of the beam stop. While positioning the re-entrant tube inside the apparatus the beam stop would invariably receive a knock of some sort, moving it away from the desired alignment. At best this would cause a misalignment of the centres of the beam stop and filter, resulting in asymmetric diffraction patterns. However, it was often the case that the beam stop

would move so far that the electron beam could no longer be directed into the Faraday cup. A second more serious worry was that the beam stop could be knocked into the phosphor screen, damaging it irreparably. Admittedly, because the new camera was to be mounted on an *xyz*-translator, the risk of the beam stop receiving a knock was substantially reduced, although it was still a possibility and a factor that was taken into consideration in the new design.

Another problem with the existing beam stop was the lack of an obvious heat dissipation route. This problem arises as the low gas pressure inside the apparatus, required for electron diffraction, effectively removes the main heat dissipation route by convection that would occur at atmospheric pressure, whilst conduction and radiation are limited. Although the maximum power of the electron beam is only about 5 W (50 kV and 100 μA), the heat in the beam stop builds up over time and, although not proven, it appeared that this heat build up was enough to melt the solder connection to the previous Faraday cup, approximately 5 cm from the incident electron beam.

3.3.2. The new design

The new beam-stop design is shown schematically in **Figure 3.10**, and can be seen in both its constituent parts and in its constructed form in **Figure 3.11**. In addition to the selection of appropriate materials for heat dissipation (**Section 3.3.3**) a number of other factors were taken into consideration and are summarised below.

The beam stop was designed in such a way that it could be almost completely dissembled. This is desirable so that it can be cleaned easily, any problems can be easily found, it allows individual parts, rather than the whole beam stop, to be remade if broken and, if necessary, it facilitates further modification. The use of solder and adhesives was avoided, in favour of mechanical fittings. For example, the electrical connection to the Faraday cup was made by clamping the wire with a screw.

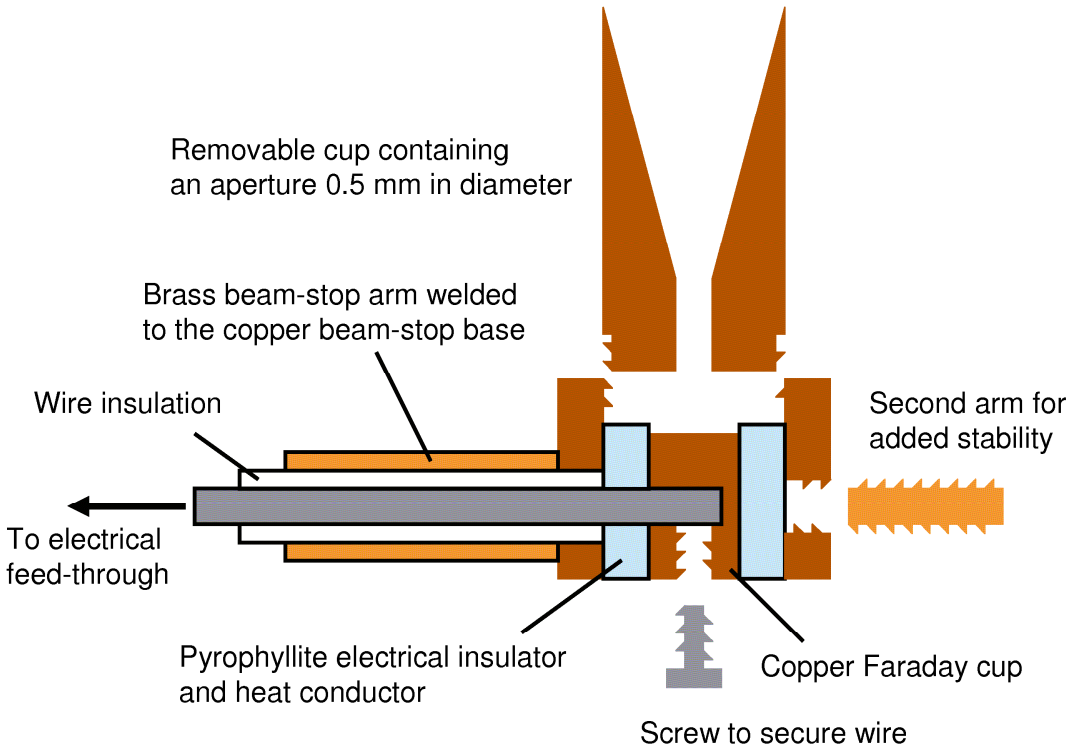

Figure 3.10 – Schematic diagram of the final beam-stop design.

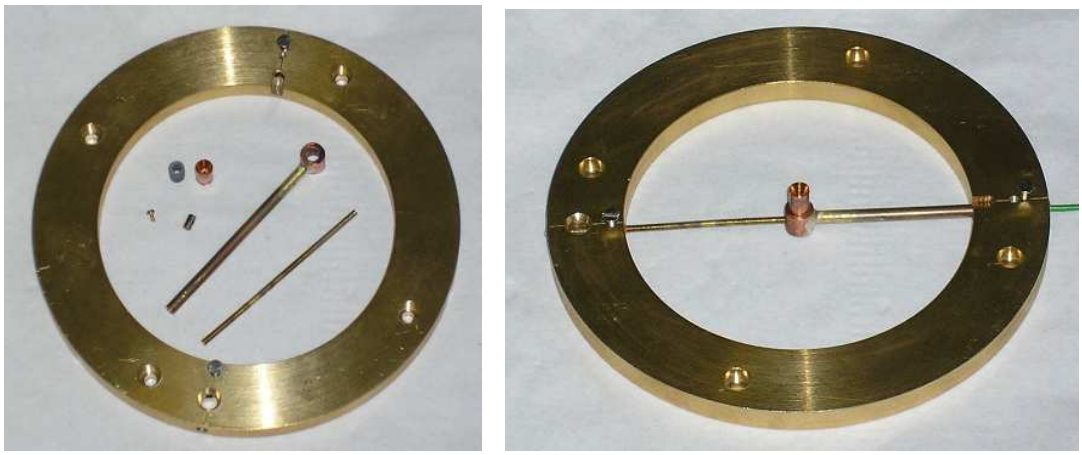

Figure 3.11 – The component parts of the new beam stop (left) and in its constructed form (right).

The physical stability of the beam stop was addressed in two ways. First, a solid circular brass base was used to attach the beam stop to the camera using four of the eight screw holes on the face of the camera, so that a knock to the base would not change the beam-stop position. Secondly, an optional second arm was included to add extra stability. These two features were also designed with the heat dissipation problem in mind, as the brass base would provide a good heat sink at the end of the beam stop arm, whilst the second arm would provide an extra route for heat to escape. In addition it was hoped that the circular symmetry of the base would help to centre the beam stop on the camera face.

The final important decision was the choice of size for the beam stop. The diameter of the beam stop limits the range of available data at small scattering angles, whilst its depth determines how closely the camera can be positioned to the fixed scattering point, limiting the widest angles at which data can be collected. The latter of these was addressed by adopting a low profile design, whereby the base of the beam stop protruded only a little more than the electronic feed-through, at the same time providing some protection against short circuiting the Faraday cup. The beam-stop diameter was chosen considering that a minimum s value of 40 nm^{-1} was desirable at the minimum nozzle-to-camera distance of about 10 cm. Assuming an electron wavelength of 6 pm therefore led to a maximum beam-stop diameter of 7 mm.

3.3.3. Choice of materials for beam stop components

For various metals the temperature difference, ΔT, between the point of impact of the electron beam with the beam stop and the beam stop base that would occur at equilibrium were calculated using **Equation 3.9**, where P is the power of the electron beam, L is the distance over which ΔT is to be calculated, τ is the thermal conductivity of the metal and A is the cross-sectional area of the metal normal to the direction of heat flow.

$$\Delta T = \frac{PL}{\tau A} \tag{3.9}$$

Calculated values for ΔT are shown in **Table 3.1** based on an area of 5 mm^2, a beam-stop length of 40 mm, a maximum beam power of 5 W (50 kV and 100 μA) and a routine beam power of 0.8 W (40 kV and 20 μA). It can be seen that copper and aluminium are better conductors than brass and stainless steel, so would be preferable on grounds of heat dissipation. The initial design therefore used copper for all of the metal components in the beam stop. However, it was also desirable to create a beam stop that would be reliably rigid and well centred on the camera face and for this purpose copper and aluminium were found to be too soft. Stainless steel was ruled out as its thermal conductivity was too low, but brass was a good compromise as it was felt that a maximum temperature increase of 400 K was tolerable.

Table 3.1 – Thermal conductivities of various metals and alloys and calculated maximum and routine equilibrated temperature increase on bombardment with an electron beam. For the parameters used in calulations, see text.

Material	Thermal conductivity, τ / W m^{-1} K^{-1}	ΔT_{max} / K	$\Delta T_{routine}$ / K
Aluminium	240	170	25
Brass	100	400	65
Copper	400	100	15
Stainless steel	20	2000	320

In addition to dissipating heat along the beam-stop arm, there needed to be a mechanism for dissipating the heat generated in the Faraday cup, which was anticipated to account for about 50% of a well-centred and focused beam. The biggest problem was finding a suitable way to insulate the Faraday cup electrically from the earthed camera, while enabling the heat to be carried away from it. It was decided that a ceramic material would serve this purpose and two potential materials were identified. One was a readily available machinable ceramic based on the natural mineral pyrophyllite ($AlSi_2O_5OH$), which has a thermal conductivity of about 2 W

m^{-1} K^{-1}. The second was a more expensive synthetic ceramic called Shapal-M®, based on aluminium nitride and with a much higher thermal conductivity of about 90 W m^{-1} K^{-1}. In order to decide whether the extra cost was necessary some further calculations were performed. Based on the design in **Figure 3.10**, the ceramic component was assumed to be cylindrical with an inner radius, L_{min}, an outer radius, L_{max}, and a height, h. As the area normal to the heat flow is now a function of the cylinder radius, **Equation 3.9** must be modified to **Equation 3.10**.

$$\Delta T = \frac{P}{\tau}\int_{L_{min}}^{L_{max}} \frac{1}{A(L)}\,\mathrm{d}L = \frac{P}{\tau}\int_{L_{min}}^{L_{max}} \frac{1}{2\pi hL}\,\mathrm{d}L = \frac{P}{2\pi h\tau}[\ln(L_{max}) - \ln(L_{min})] \qquad (3.10)$$

Taking a value of 1.5 mm for the inner radius, 2.5 mm for the outer radius, 4 mm for its height, 2.5 W for the electron-beam power reaching the Faraday cup and the thermal conductivity of pyrophyllite (2 W m^{-1} K^{-1}), the temperature difference was calculated to be about 25 K. The bottle-neck may not, therefore, be the heat transfer through the ceramic material, but could be the efficiency of heat transfer over the contact between the ceramic and copper surfaces. Pyrophyllite was therefore used as the electrical insulator.

3.4. Electron beam alignment

Aligning an electron beam presents one of the largest practical hurdles in traditional GED experiments. There are various contributory factors but part of the problem is that if the beam cannot be found immediately, it can be difficult to determine its position, or to discover what has caused the beam to move (if it had previously been aligned).

In general two methods can be used to find the electron beam. First, the electron beam can be viewed using a phosphor screen, on which a focused beam would appear as a small spot and the quality of focusing can be assessed by observing the

size and symmetry of this spot. The phosphor screen is also useful if the full beam cannot be seen at all, as any scattered electrons can give an indication of the electron-beam position. Secondly, the electron-beam position can be inferred by using Faraday cups coupled to electrometers.

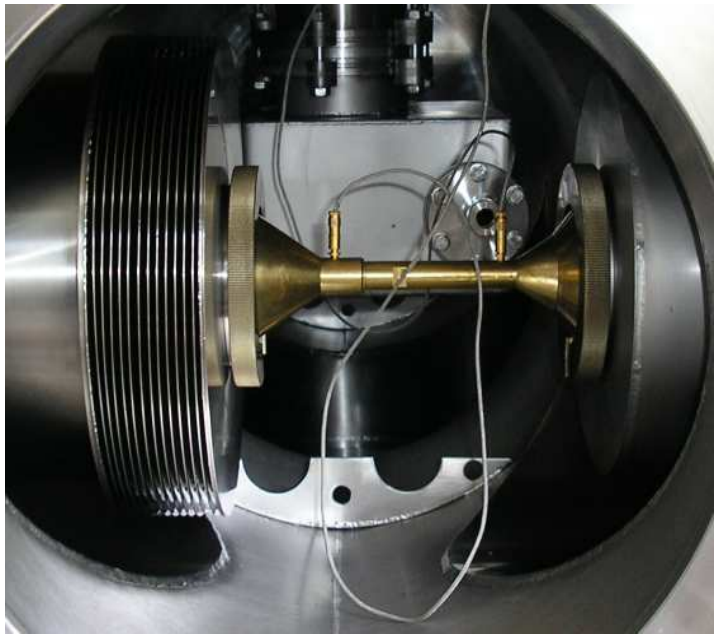

Figure 3.12 – Beam tube with two collars inside the apparatus.

The initial alignment was performed using the phosphor screen shown in **Figure 3.9** and a beam tube containing two copper collars (**Figure 3.12**), electrically insulated from the beam tube itself, from which current readings were taken. This setup successfully enabled the electron beam to be steered through the centre of the beam tube, but it struck the phosphor about five millimetres above and about two millimetres right of the centre of the screen. This was a concern as the diameter of the new camera was only a centimetre narrower than the inner diameter of the camera chamber. At the time it was unknown whether the origin of this misalignment was a sagging of the re-entrant tube, a larger magnetic deflection than expected or simply a geometric misalignment of the electron beam with the central axis of the diffraction chamber. (It was subsequently found to be a problem with the re-entrant tube, which became clear when the trial camera [see below] was tested.)

In order to prevent possible damage to the new camera and to determine the position of the electron beam, a trial camera was built that had the same weight and diameter as the new camera, that could accommodate the new beam stop and that could be mounted on the *xyz*-translator in the same way as the new camera. The trial camera with the beam stop attached is shown in **Figure 3.13**, both resting on the bench and mounted on the *xyz*-translator.

The trial camera and beam stop were then used to find the electron beam and record its position at a range of nozzle-to-camera distances, from about 110 to 320 mm (corresponding to readings of z = 90 mm and 300 mm, respectively, on the *xyz*-translator). At distances greater than this the electron beam moved too far from the centre of the chamber to centre it on the beam stop. This was not a concern, however, as data were not likely to be required at nozzle-to-camera distances greater than 300 mm.

Figure 3.13 – Test camera and beam-stop assembly on the bench (top) and mounted on the *xyz*-translator (below).

3.5. Beam size

3.5.1. Previous characterisation of beam width and shape

The size of the electron beam produced by the Edinburgh telefocus gun at 30 kV has previously been characterised by Robert Fender.[2] The method adopted was to place a ceramic disk containing a 0.85 mm aperture over a Woods' horn from which a current was recorded. 1-D cross-sections of the beam intensity were then obtained by recording the beam current through this aperture at a range of horizontal displacements of the detector from the position of maximum intensity. In addition, a 2-D surface composed of cross-sections at a range of detector heights was recorded. 1-D cross-sections were recorded for emission currents of 1.0 and 2.0 μA, 600 and 500 mm from the electron gun, respectively. The intensity profiles were approximately Gaussian in shape and the respective full-width, half-maximum (FWHM) values for the raw data for these beam currents and distances were estimated to be approximately 0.94 mm and 0.76 mm. A 2-D plot of the electron beam intensity was obtained at a beam current of 1.0 μA, 600 mm from the electron gun. An attempt to deconvolute this data to account for the effect of using a finite aperture size was performed and reduced the FWHM from 0.94 to 0.6 mm and, curiously, yielded a double maximum in the resulting intensity profile. As the initial data displayed no such double maximum, Fender attributed this phenomenon to poorly fitting data.

3.5.2. Calculation of beam width for a Gaussian intensity profile

An alternative approach to estimating the beam size is to use knowledge of the aperture size and assume a Gaussian beam profile (**Equation 3.11**). The ratio of the recorded current, I_{rec}, to the total beam current, I_{tot}, is given in **Equation 3.12**, where R is the radius of the aperture and σ is the standard deviation of the electron-beam intensity.

$$I = \frac{I_{tot}}{2\pi\sigma^2}\exp\left(-\frac{r^2}{2\sigma^2}\right) \tag{3.11}$$

$$\frac{I_{rec}}{I_{tot}} = \frac{1}{2\pi\sigma^2}\int_0^{2\pi}\int_0^{R}\exp\left(\frac{-r^2}{2\sigma^2}\right)r\mathrm{d}\theta\mathrm{d}r = \frac{1}{\sigma^2}\int_0^{R} r\exp\left(\frac{-r^2}{2\sigma^2}\right)\mathrm{d}r = 1-\exp\left(\frac{-R^2}{2\sigma^2}\right) \tag{3.12}$$

$$\sigma = R\left(-2\ln\left[1-\frac{I_{\mathrm{rec}}}{I_{\mathrm{tot}}}\right]\right)^{-\frac{1}{2}} \tag{3.13}$$

Equation 3.12 is rewritten in terms of σ in **Equation 3.13** and is plotted in **Figure 3.14**, where the solid line is for a 0.5 mm aperture as used in the new beam stop and the dashed line is for a 0.85 mm aperture as used by Fender in the original characterisation. The standard deviation, σ, can be related to the FWHM as shown in **Equation 3.14**, the solution for which is given in **Equation 3.15**.

$$\frac{I}{I_{\max}} = \frac{1}{2} = \exp\left(-\frac{r_{\mathrm{HM}}{}^2}{2\sigma^2}\right) = \exp\left(-\frac{\left[\mathrm{FWHM}/2\right]^2}{2\sigma^2}\right) \tag{3.14}$$

$$\mathrm{FWHM} = 2\sigma\sqrt{-2\ln(0.5)} = 2.355\sigma \tag{3.15}$$

Fender recorded a current of 0.51 μA for a total beam current of 1 μA and for the 2 μA beam recorded 1.25 μA. Application of **Equations 3.13** and **3.15** yields FWHMs of 0.84 and 0.71 mm for the 1 and 2 μA beams, respectively, whereas Fender quoted respective values of approximately 0.94 and 0.76 mm based on the 1-D cross-sections. These values are reasonably consistent given the crude approximation of point detection in the cross-section method and the assumption of a Gaussian intensity profile implicit in **Equations 3.13** and **3.15**.

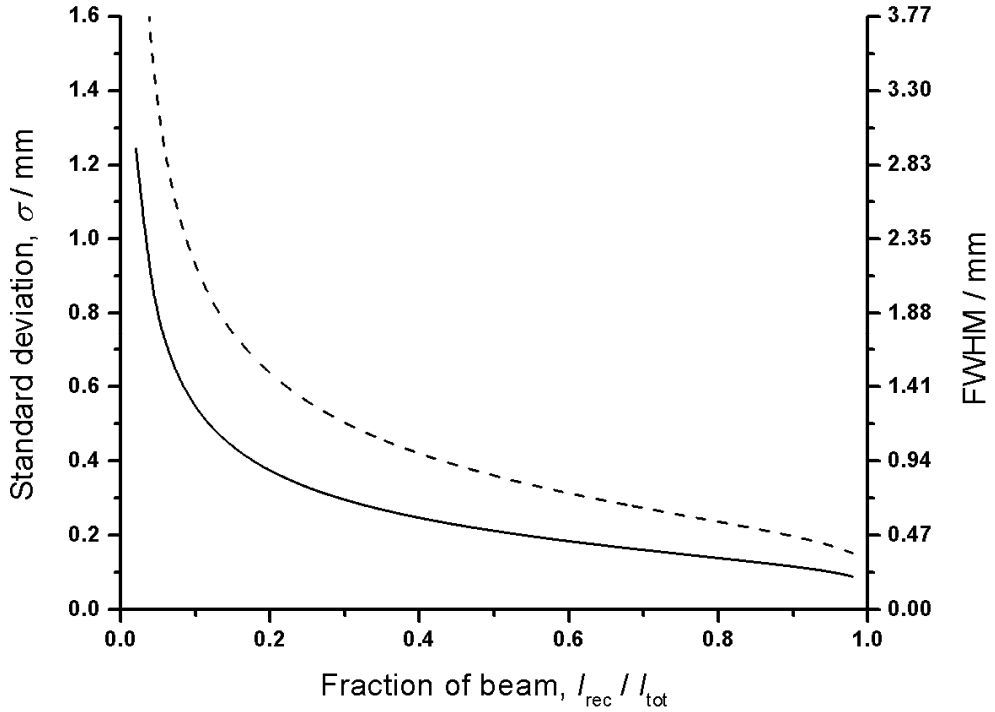

Figure 3.14 – Electron beam sizes calculated using Equation 13, where an aperture diameter of 0.5 or 0.85 mm (solid and dashed, respectively) has been used.

3.5.3. Estimated beam sizes using the new beam stop

After reproducible alignment of the electron beam (**Section 3.4**) had been achieved, the following method was used to estimate the size of a 40 keV beam over the range of nozzle-to-camera distances likely to be used in a GED experiment. The electron beam was centred on the beam stop, and then deflected onto the far collar of the double-collared beam tube (**Figure 3.12**). The current obtained from this collar was assumed to be the total beam current, I_{tot}, and was adjusted to 0.10, 1.00 or 10.0 μA by changing the bias voltage on the Wehnelt cap. The electron beam was then re-centred on the beam stop and the current, I_{rec}, recorded before the process was repeated at another camera distance. The fraction of the beam to reach the Faraday cup is plotted against the camera position in **Figure 3.15** and the corresponding beam

sizes, estimated using **Equations 13** and **15**, are plotted against the camera position in **Figure 3.16**.

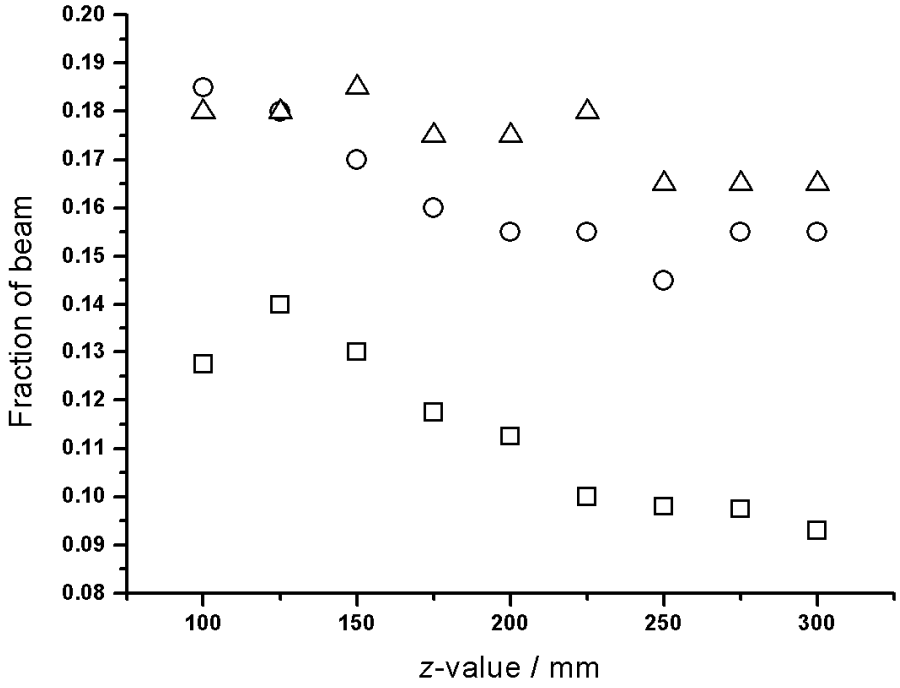

Figure 3.15 – Fraction of total beam current recorded at the beam stop for a 40 keV beam at various camera distances, *z*, and total beam currents: ○ = 0.1 μA, Δ = 1 μA and □ = 10 μA. The distance from the anode to the camera is approximately equal to *z* + 280 mm.

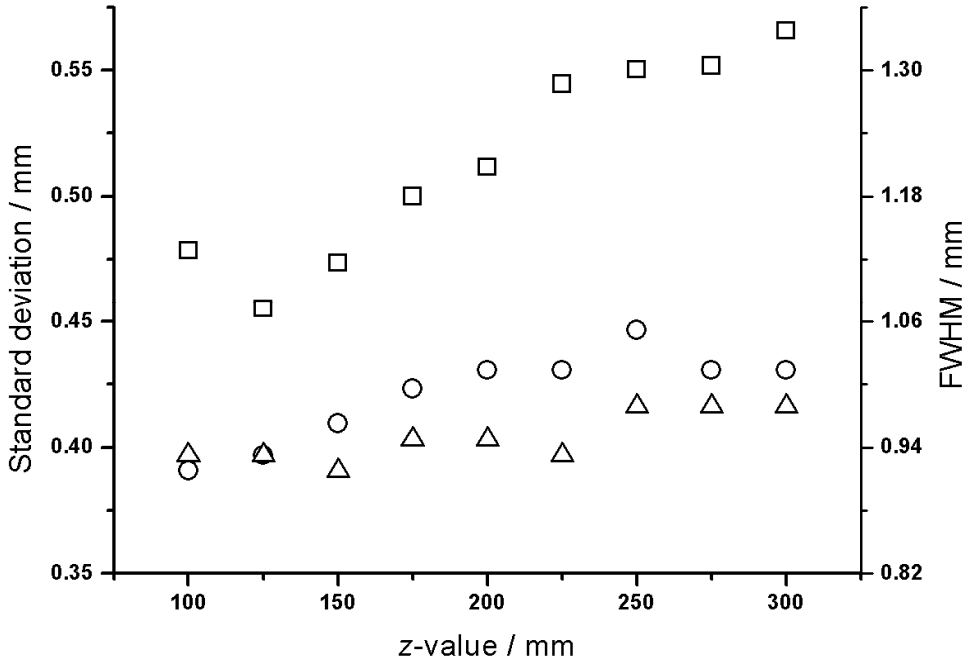

Figure 3.16 – Estimated beam sizes for a 40 keV beam at various camera distances, *z*, and total beam currents: ○ = 0.10 μA, Δ = 1.00 μA and □ = 10.0 μA. The distance from the anode to the camera is approximately equal to *z* + 280 mm.

3.6. References

1. High Energy Electron Scattering, Chapter 7, R. A. Bonham and M. Fink. *Van Nostrand Reinhold Co.* (1974), ACS Monograph 169.
2. R. S. Fender, Ph.D. thesis, *University of Edinburgh* (1996).
3. P. Papathomas, Ph.D. thesis, *University of Edinburgh* (1998).

Chapter 4

Calibration of the new CCD camera

4.1. Outline of the calibration task and possible approaches

4.1.1. Corrections to experimental GED data

Before an electron diffraction refinement can be performed, the data obtained from the diffraction image must be corrected to retrieve the intensity of the diffracted electrons. In a traditional type of set-up, this would involve three corrections: a "blackness" correction which accounts for photographic film having a non-linear response to incident electron intensity, a geometric "plate flatness" correction that divides the recorded intensity by $\cos^3(\theta)$ (where θ is the angle by which the electrons are deflected) and, most importantly, a correction for the rotating sector.

Data from the SSED apparatus will also require a flatness correction, but we will assume a linear response of the camera to electron intensity (*i.e.* the intensity of light produced by the phosphor is proportional to the incident electron intensity and the charge generated on each pixel of the CCD is proportional to the number of photons it is exposed to). The optical filter between the phosphor and the CCD in the new camera is the analogue of the rotating sector in a traditional set-up and a correction for this is essential for calibrating the camera. The remaining problem is accounting for a non-uniform coating of phosphor and aluminium. If the phosphor is uneven some areas may be brighter than others. The effect of the aluminium, however, is two-fold: it slows down electrons so they have less energy to convert into light at the phosphor and it acts as an electron multiplier as the high-energy electrons knock secondary electrons out of the aluminium. In addition, X-rays may be created as the electrons travel through the aluminium, so it is unclear whether a local increase in thickness will increase or decrease the recorded intensity at that point, but an uneven coating is likely to result in some areas of higher intensity than others.

4.1.2. Approaches considered

The optical filter and any unevenness of the phosphor and aluminium coatings can be dealt with in a single step (herein collectively termed the filter correction) by irradiating the camera with electrons with a known distribution at the experimental energy (*ca.* 40 keV). Ideally, this would be done using a β-emitting radioactive source, which would provide an almost uniform irradiation of the camera. However, in addition to the problems of finding a suitable source with an appropriate half life and energy, and the inherent handling difficulties, there exists the question of how to suspend the sample in the apparatus and how to eliminate contributions form reflections and X-rays from the chamber walls.

A more practical solution is to perform a scattering experiment using a compound with a well-known structure and (after applying the flatness correction) take the ratio of the observed and calculated intensities as the total correction (**Equation 4.1**).

$$Filter\ \ function = \frac{I_{observed}}{I_{incident}} \approx \frac{I_{observed}}{I_{theoretical}} \tag{4.1}$$

However, great care must be taken with such an approach because the compound used for the calibration has its own diffraction pattern, so any error in the calibration will introduce false data into future refinements. As can be seen in **Equation 4.2**, the incoherent background intensity is a likely source of error in such a calibration, as it is not accounted for in the theoretical intensities.

$$\frac{Filter\ function_{estimated}}{Filter\ function_{actual}} = \frac{I_{incident}}{I_{theoretical}} = \frac{I_{atomic} + I_{mol} + I_{backgroumd}}{I_{atomic} + I_{mol}} \tag{4.2}$$

The background intensity is composed of contributions from inelastic scattering, scattering from background gas, scattering from the beam stop and other surfaces in

the apparatus, and light from the filament. The background intensities due to light and scattering from the beam stop can be compensated for by subtracting a background of an equal exposure time to the diffraction image. The contribution from background gas is difficult to assess and the best approach is to minimise this experimentally, but it may also be possible to estimate once a reasonably accurate filter function is known. As the inelastic scattering is independent of the apparatus used, it should be possible to estimate this from diffraction data from other experimental set-ups where the same accelerating voltage has been used.

In addition to the problem with experimental background, errors in the theoretical intensities can also creep into the calibration as a result of errors in the structure parameters (distances, distance corrections and inter-nuclear probability distributions) or inadequacies in the theory adopted, such as assumption of the independent-atom model or omission of three-atom scattering terms. As for inelastic background scattering the contributions errors in the theoretical intensities due to assumption of the independent-atom model are predominantly at small scattering angles.

In view of this concern of introducing false data, argon is often adopted as the calibrant. (This also eliminates worries about the applicability of the independent-atom model.) However, the low boiling point of argon makes condensation difficult, requiring an efficient cold trap and, ideally, liquid helium cooling.

In the calibration that follows, benzene was chosen as the scattering source as its structure is well characterised. Data were obtained from a number of nozzle-to-camera distances as this would smooth out any oscillations inherited from the benzene pattern. However, this did not completely remove this concern and, as the filter was quoted to be linear in optical density, an exponential function that was fitted to the intensity ratio was considered to be the best initial attempt at calibration.

In addition to choosing an appropriate experimental procedure the correction could be applied to every pixel individually or to the average intensity profile, as is done for the rotating sector correction in a conventional set-up. The former approach is preferable as it does not assume that the electron beam position is identical on each occasion and is also better equipped to compensate for anomalous pixels. However, as an initial calibration procedure this was less suitable as errors would be less easily recognised and, as it required writing a program, would be substantially more time-consuming. A Fortran program for reading .raw files created by the camera software and applying filter corrections to individual pixels has been written, however, and is included in **Appendix 1**. This can correct data for an assumed radial function, therefore allowing some misalignment of the filter centre with the centre of diffraction. In order to use the ratio of the experimental to theoretical intensities to perform the correction, an interpolation method is still required and, given the results in this chapter, a smooth two-dimensional function will probably have to be fitted to the intensity ratios.

4.2. General procedures

4.2.1. Planning of a suitable procedure

Prior to analysing any GED data the following information was available:

- The pixel size of the CCD is 24 μm and the magnification due to the fibre optic taper is 3.17:1 with a maximum distortion of 2%, so the effective pixel size is 76 μm.

- The optical filter was deposited on a fibre-optic faceplate with a radius of 39.88 mm. It was quoted as having an optical density of 2.0 (± 5%) in the centre, dropping off linearly with optical density to the edge.

- The electron accelerating voltage could be set using the Start Spellman high voltage supply, from which a voltage reading could be obtained with a precision of 10 V. The voltage reading did not drift during the course of the experiment, but as the calibration of the high-voltage supply was performed many years ago and the steering of the electron beam is performed using electrostatics, rather than magnetically, the uncertainty in the electron energy is more than 10 eV.

- Either the electron wavelength or the camera pixel size could be calibrated using diffraction data, but not both. However, after one has been calibrated the scaling errors cancel. The electron wavelength was subsequently scaled as this was more convenient.

- The nozzle-to-camera distances were only known to an accuracy of about 20 mm, but the differences between camera positions could be determined with an accuracy of *ca.* 0.2 mm. Therefore, these difference values could be used to scale either the electron wavelength or the camera pixel size and obtain accurate nozzle-to-camera distances.

The proposed procedure for calibrating the camera pixel size and the optical filter is shown in the form of a flowchart in **Figure 4.1**.

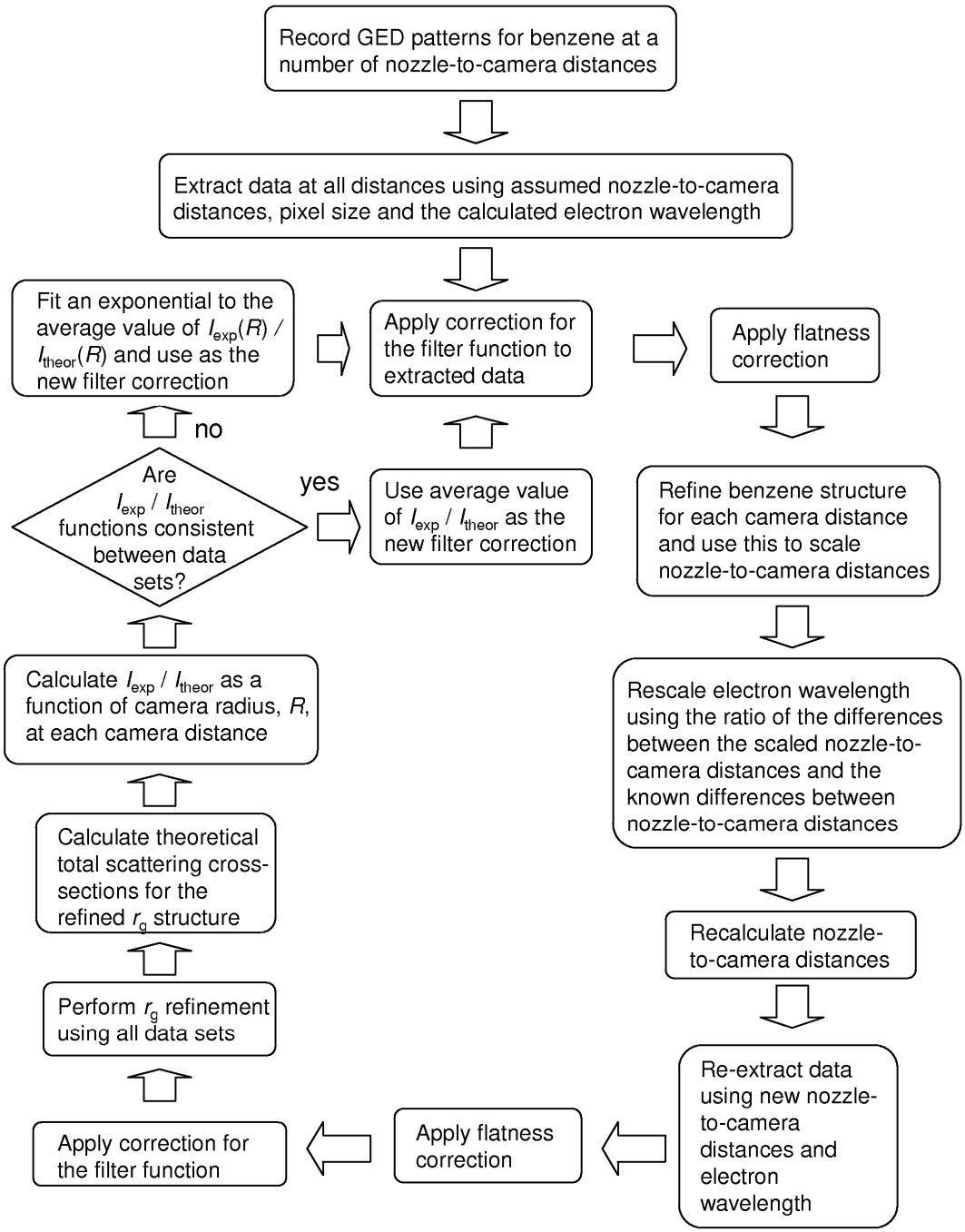

Figure 4.1 – Flowchart for the camera calibration procedure. In principle, the procedure should be followed until self-consistent.

4.2.2. GED experimental

Benzene vapour was introduced into the electron beam path using a needle nozzle with inner and outer diameters of *ca.* 0.25 and 0.5 mm, respectively, mounted on an *xyz* translator. The needle was positioned as follows: It was moved into the electron beam so that the current from the Faraday cup in the beam stop fell to zero. The needle was drawn backwards until a current could again be read from the Faraday cup and the needle was again translated perpendicular to the electron beam and positioned so that a minimum in the current was observed, ensuring that the needle was well centred. Finally, the needle was withdrawn further in approximately 0.25 mm steps, capturing images using the CCD camera at each step, until no electron scattering from the needle could be observed.

The vapour pressure of benzene was found to be too high to use at room temperature as the main chamber pressure increased from *ca.* 1.5×10^{-5} to 4×10^{-4} mbar, although the pressures in the other chambers did not change significantly. The benzene sample was therefore cooled using liquid nitrogen, at which point a background image was captured. The sample was allowed to warm in air and a series of images was acquired, beginning as the main chamber pressure started to rise. As the camera pixels at small scattering angles began to saturate, the sample was cooled once again and a second background image was captured.

4.2.3. Image handling

The image processing was performed using the Photoshop CS3 software package. For each camera distance, the two background images, acquired before and after the benzene diffraction, were averaged and subtracted from the highest quality images. In preparation for data extraction (**Section 4.2.4**) using the XPKG program[1] the .raw images generated by the camera software were converted to TIFF format. For data extraction using the UNEX[2] program the images were converted to their negative

and the beam stop masked by setting the intensities to maximum before converting to the TIFF format.

4.2.4. Data extraction

Two data extraction programs were investigated, namely the XPKG[1] and UNEX[2] programs. As these programs were developed completely independently, comparison of the data obtained from the two methods can help to reveal any errors introduced during the data extraction stage. The data from a number of refinements were subsequently compared and no significant differences were observed. The main advantage of the UNEX program, for the extraction of data from the SSED apparatus, is that the shadow from the beam stop can be masked so that it does not affect the centring of the diffraction pattern. However, it contains a number of other features such as the ability to refine the misalignment of the centre of a rotating sector (or filter) with that of the diffraction pattern and the removal of an asymmetric background prior to data reduction. The results in **Sections 4.3** to **4.6** were therefore obtained using the UNEX program to extract the data.

4.2.5. Data correction

The optical density (*O.D.*) of the filter quoted by Rigaku can be described by the function in **Equation 4.3**, where *R* is the radius of the faceplate (39.88 mm) and *r* is the radius on the camera face of a single data point, related to the scattering vector, *s*, by **Equation 4.4** (*L* is the nozzle-to-camera distance).

$$O.D.(r) = 2 \times \left(1 - \frac{r}{R}\right) \tag{4.3}$$

$$s = \frac{4\pi}{\lambda} \sin\left(\frac{\tan^{-1}(r/L)}{2}\right) \tag{4.4}$$

Equation 4.3 can be rewritten to give the incident intensity, I_0, in terms of the recorded intensity, I, and the radius of the data, r, as shown in **Equation 4.5**.

$$I_0 = I \times \exp\left(2 \times \ln 10 \times \left[1 - \frac{r}{R}\right]\right) \tag{4.5}$$

Data extracted using UNEX were corrected for this filter function (and those calculated experimentally) within the program. However, UNEX also multiplied the intensities by r^3, which was corrected for when data were read into the ed@ed program.[3] No filter correction was performed by the XPKG program, therefore, when this method was adopted the filter correction was performed as data was read into ed@ed.

In all cases, data were corrected for plate flatness within the ed@ed program and reduction of the corrected data to obtain experimental molecular-scattering intensity curves was performed in the usual way.

4.2.6. Generation of theoretical intensity cross-sections

Total theoretical intensity curves ($I_{\text{atomic}} + I_{\text{molecular}}$) were calculated as a function of the scattering vector, s, using the SCATTER program.[4] As it was an early version of the program no distance corrections were used and only harmonic vibrations were accounted for, assuming a Gaussian probability distribution for each inter-nuclear distance. The resulting intensity cross-sections therefore corresponded to an r_g structure type, so the input parameters for generation of these total intensity curves were taken from an r_g structure refinement, as indicated in **Figure 4.1**.

4.3. Calculation of camera distances and electron wavelength

4.3.1. Initial benzene refinement

Benzene data were obtained for five nozzle-to-camera distances (170, 195, 220, 245 and 270 mm), for which the absolute distances were only roughly known, but the differences were set to 25.0(2) mm. An r_a refinement was performed at each distance using a benzene model with a fixed ratio of the C–C and C–H bond lengths (139.7:108.4). The C–C distance was allowed to refine, as were all amplitudes of vibration except those between hydrogen atoms. The refined molecular-intensity and radial-distribution curves are shown in **Figures 4.2** to **4.6**. The data analysis parameters are shown in **Table 4.1** and the inter-nuclear distances and corresponding amplitudes of vibration are shown in **Table 4.2**.

From **Table 4.2** it can be seen that, for almost all inter-atomic distances, the refined amplitudes of vibration were much larger than the calculated values. This indicates that the assumed filter function is overcorrecting the data at small *s* values. However, a similar effect would be observed if the scattering was not from a single point, but from a range of nozzle-to-camera distances close to the determined value.

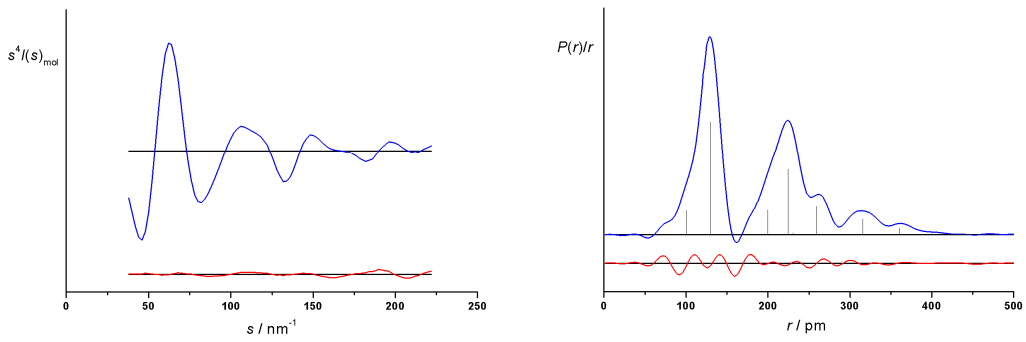

Figure 4.2 – Molecular-intensity and radial-distribution curves for benzene at an assumed nozzle-to-camera distance of 170 mm.

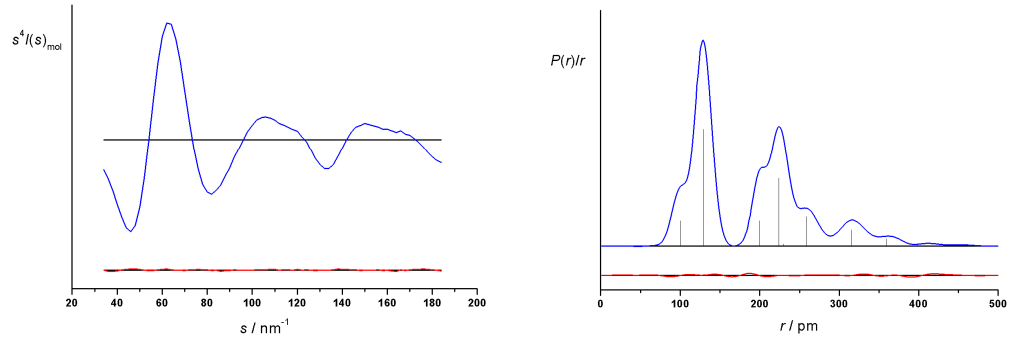

Figure 4.3 – Molecular-intensity and radial-distribution curves for benzene at an assumed nozzle-to-camera distance of 195 mm.

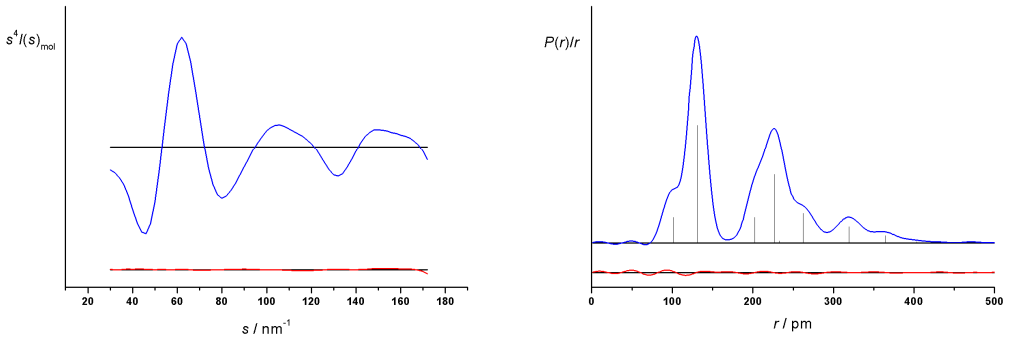

Figure 4.4 – Molecular-intensity and radial-distribution curves for benzene at an assumed nozzle-to-camera distance of 220 mm.

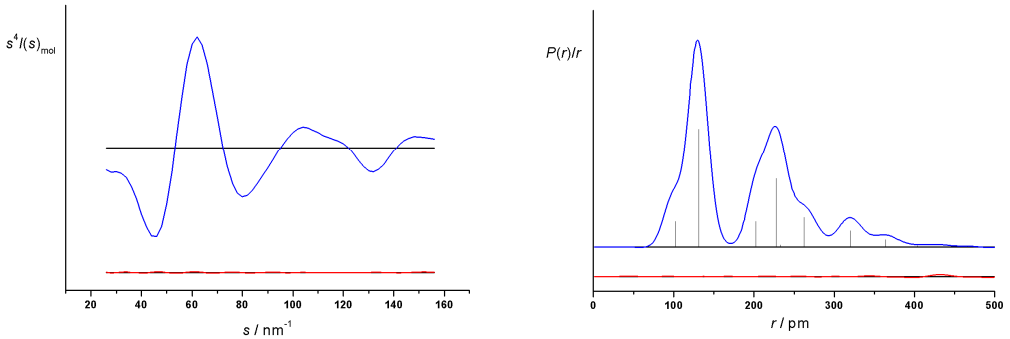

Figure 4.5 – Molecular-intensity and radial-distribution curves for benzene at an assumed nozzle-to-camera distance of 245 mm.

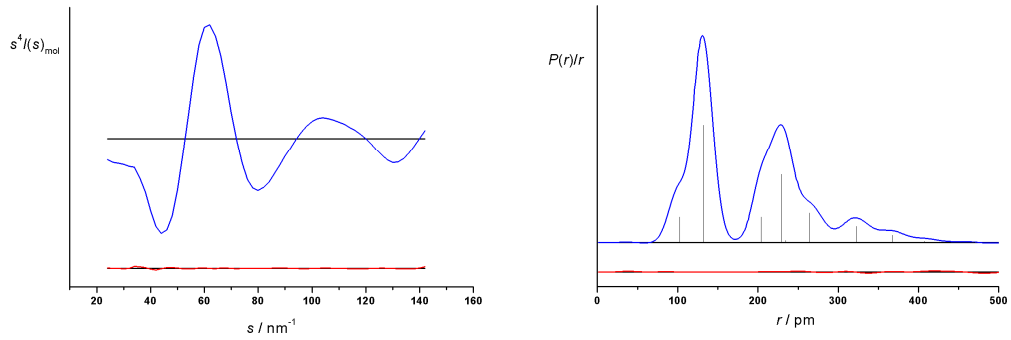

Figure 4.6 – Molecular-intensity and radial-distribution curves for benzene at an assumed nozzle-to-camera distance of 270 mm.

Table 4.1 – GED data analysis parameters.[a]

Camera distance	170	195	220	245	270
R_G	10.94%	3.95%	3.14%	2.53%	3.03%
R_D	10.19%	2.39%	2.53%	1.51%	1.92%
Scale factor, k	1.454(26)	1.308(11)	1.467(11)	1.338(9)	1.349(17)
Correlation parameter	0.499	0.426	0.498	0.433	0.401
Δs	2	2	2	2	2
s_{min}	38	34	30	26	24
s_{w1}	58	54	50	46	44
s_{w2}	190	158	148	134	122
s_{max}	222	184	172	156	142
Electron wavelength	6.018	6.018	6.018	6.018	6.018

[a] Units of s are nm^{-1}, nozzle-to-camera distances are in mm and electron wavelengths are in pm.

Table 4.2 – Inter-nuclear distances and root-mean-squared amplitudes of vibration involving carbon.[a]

	170 mm		195 mm		220 mm		245 mm		270 mm		Calc.[b]
	r_a	u	r_a	u	r_a	u	r_a	u	r_a	u	u
C–C	129.72(13)	9.3(3)	129.49(6)	8.7(2)	131.14(5)	9.0(2)	131.26(5)	10.4(2)	132.30(8)	10.4(3)	4.53
C–H	100.66(10)	10.2(12)	100.48(4)	8.2(5)	101.76(4)	10.4(6)	101.85(4)	10.9(5)	102.65(6)	10.7(9)	7.56
C···C*meta*	224.69(23)	10.5(4)	224.28(10)	9.3(3)	227.15(9)	10.6(2)	227.34(9)	11.5(2)	229.14(13)	11.9(4)	5.43
C···C*para*	259.44(26)	13.2(6)	258.97(11)	13.6(4)	262.29(11)	14.4(3)	262.51(10)	14.6(4)	264.59(15)	15.5(6)	6.06
C···H*ortho*	200.04(20)	10.1(8)	199.68(9)	6.0(6)	202.24(8)	9.1(4)	202.41(8)	9.2(4)	204.01(12)	9.4(5)	9.76
C···H*meta*	315.89(32)	13.7(8)	315.32(14)	13.0(5)	319.36(13)	13.6(3)	319.63(12)	13.0(3)	322.16(19)	16.2(6)	9.37
C···H*para*	360.10(36)	14.5(16)	359.45(16)	15.3(12)	364.05(15)	14.4(6)	364.36(14)	14.3(7)	367.25(21)	16.5(13)	9.31

[a] All molecular dimensions in units of pm.

[b] Reference 5. Obtained at the B3LYP/cc-pVTZ level of theory.

4.3.2. Camera distances and electron wavelength

The C–C distances obtained in **Section 4.3.1** were used to scale the nozzle-to-camera distances, assuming the correct r_a C–C distance to be 139.70 pm. These were plotted against the original distances (**Figure 4.7**) and a linear regression was fitted to the series of points, given by **Equation 4.6**, or, with axes reversed, by **Equation 4.7**.

$$Z_{\text{benzene}} = 1.018(12) \times Z_{\text{estimated}} + 10.8(26) \quad (4.6)$$

$$Z_{\text{estimated}} = 0.982(11) \times Z_{\text{benzene}} - 10.5(26) \quad (4.7)$$

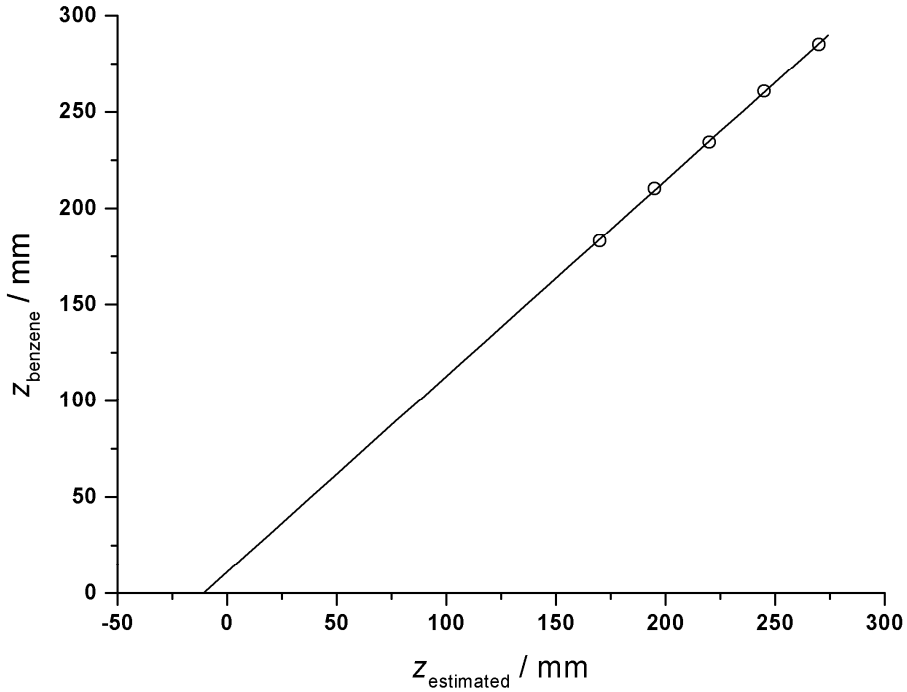

Figure 4.7 – Nozzle-to-camera distances calculated from benzene diffraction pattern (z_{benzene}) and initial nozzle-to-camera distances ($z_{\text{estimated}}$) for which the differences were well known. The *x*-intercept is -10.5(26) mm, which is the error in the estimated nozzle position, whilst the gradient is 1.018(12), which is the scaling correction to be applied to the electron wavelength.

As the differences between initial nozzle-to-camera distances ($Z_{estimated}$) were known accurately, the gradient provides the scaling factor for either the electron wavelength or the resolution of the camera. The *x*-axis intercept, –10.5(26) mm, provides the correction to be applied to the initial camera distances. The standard deviations in these values are relatively large, so further iterations are clearly required following an accurate determination of the experimental filter function. The uncertainties are smaller than the values of the corrections, however, so the corrected values should be an improvement over the initial parameters.

4.4. Benzene refinement (r_g) using corrected camera distances and electron wavelength

4.4.1. Data extraction

The data for the five data sets used in **Section 4.3** were re-extracted using the scaled electron wavelength (6.125 pm) and the corrected camera distances (180.5, 205.5, 230.5, 255.5 and 280.5 mm) determined in **Section 4.3.2**. The data were taken from approximately the same region of the camera face for each data set, from a minimum radius of 6 mm to a maximum radius of 36 mm.

4.4.2. Refinement procedure and results

An r_g refinement of the benzene structure was performed using all five data sets. In contrast to the refinement in **Section 4.3.1**, the benzene model allowed the C–C and C–H bond lengths to refine independently. All amplitudes of vibration for distances involving carbon were allowed to refine unrestrained, whilst the H···H amplitudes, which contribute only a small proportion of the total scattering, were fixed to assumed values. The total R_G and R_D factors were 8.6% and 6.5%, respectively.

The data analysis parameters are given in **Table 4.3**, the inter-nuclear distances and corresponding amplitudes of vibration are shown in **Table 4.4** and the experimental molecular-intensity and radial-distribution curves are shown in **Figures 4.8** and **4.9**, respectively.

Table 4.3 – Data analysis parameters for the first r_g refinement.

Camera distance	180.5	205.5	230.5	255.5	280.5
R_G	12.13 %	10.32 %	6.54 %	6.90 %	5.34 %
R_D	10.19 %	6.80 %	4.78 %	4.72 %	4.09 %
Scale factor, k	1.341(21)	1.252(18)	1.404(20)	1.275(18)	1.123(18)
Correlation parameter	0.498	0.493	0.496	0.494	0.497
Δs	2	2	2	2	2
s_{min}	36	30	28	26	22
s_{w1}	56	50	48	46	42
s_{w2}	172	152	136	122	112
s_{max}	200	176	158	142	130
Electron wavelength	6.125	6.125	6.125	6.125	6.125

[a] Units of s are nm^{-1}, nozzle-to-camera distances are in mm and electron wavelengths are in pm.

Table 4.4 – Inter-nuclear distances and root-mean-squared amplitudes of vibration involving carbon.[a]

	r_g	r_a	u	u [b]
C–C	139.41(6)	138.67(6)	10.18(20)	4.53
C–H	107.66(32)	106.31(32)	12.07(70)	7.56
C···C*meta*		241.01(11)	10.54(24)	5.43
C···C*para*		277.95(13)	15.55(39)	6.06
C···H*ortho*		214.23(28)	8.43(47)	9.76
C···H*meta*		338.44(34)	13.86(37)	9.37
C···H*para*		385.84(37)	15.84(80)	9.31

[a] All molecular dimensions are in units of pm.

[b] Reference 5. Obtained at the B3LYP/cc-pVTZ level of theory.

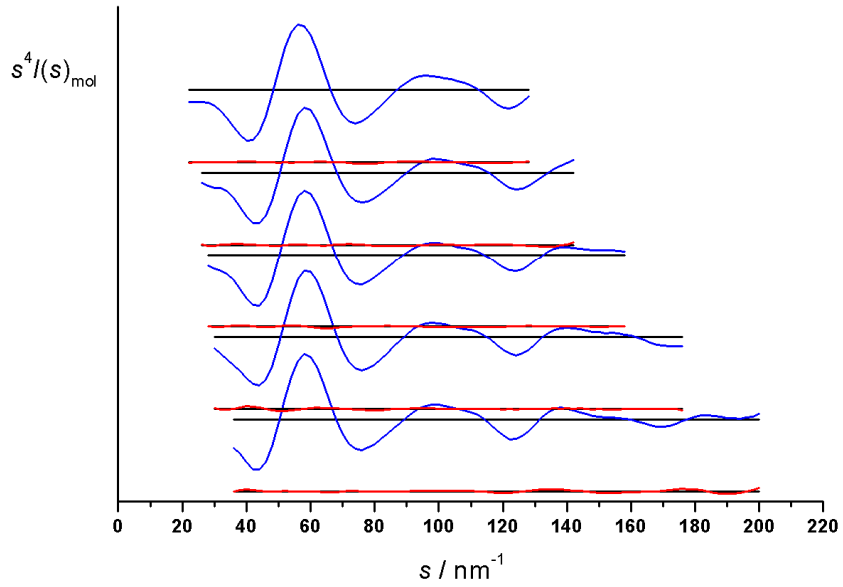

Figure 4.8 – Experimental and difference (experimental minus theoretical) molecular-intensity curves for the first benzene refinement (r_g) using the assumed filter function.

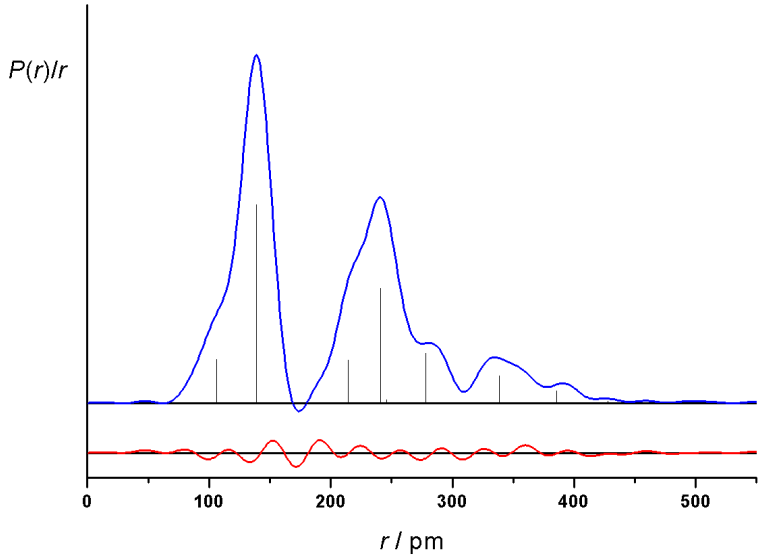

Figure 4.9 – Experimental and difference (experimental minus theoretical) radial-distribution curve, $P(r)/r$, for the first benzene refinement (r_g) using the assumed filter function. Molecular intensities were multiplied by $s\times\exp[(-0.00002s^2)/(Z_H - f_H)(Z_C - f_C)]$ before Fourier transformation.

4.4.3. Discussion

As was found in the refinements in **Section 4.3**, in general, the refined amplitudes of vibration are significantly larger than the calculated values. The overall quality of the fit is also good, as can be seen by the flatness of the difference curves in **Figure 4.8** and the R_G factor of 8.6 %.

The radial-distribution curve in **Figure 4.9** appears to contradict this observation, as there is a small but regular wave running through the difference curve. This could be attributed to an effect of the Fourier transformation, but increasing the damping factor to 3 or 4×10^{-5} has only a small effect on the difference curve. The period of the oscillation is *ca.* 35 pm, which indicates a problem in the average molecular-scattering curve at *ca.* 180 nm^{-1}. This is approximately at the joining point of the data sets, where the data set at the shortest camera distance becomes the only one contributing to the average experimental curve at this point. In addition, 180 nm^{-1} is also beyond the upper weighting point (s_{w2} = 172 nm^{-1}), therefore, the data in this region is weighted particularly weakly in the least-squares fitting process. The Fourier transformation is performed on the average intensity curve and does not account for the weighting of the data points or the number of data sets averaged and is therefore a poorer method for assessing the goodness-of-fit to the experimental data.

A similar oscillation can be observed, however, in the radial-distribution curve for the shortest camera distance in **Section 4.3** (**Figure 4.2**). This indicates that there may be a genuine problem with the data at the wider scattering angles, as in the r_a refinement the data up to 190 nm^{-1} were weighted fully in the least-squares procedure. A continuation of the refinement without the data set recorded at 180.5 mm did not significantly change any of the refining parameters, but reduced the overall R_G factor from 8.6 % to 6.8 % and improved the appearance of the radial-distribution curve, which is shown in **Figure 4.10**.

A final note should be made about the refined C–C distance [r_g = 139.41(6) pm, r_a = 138.67(6) pm]. The r_a value is about 1 pm shorter than the established r_a distance of 139.70 pm, which is not a large discrepancy, considering the standard deviation in the scaling parameter was *ca.* 1 % and that of the nozzle distance correction was 2-3 mm, again *ca.* 1 %.

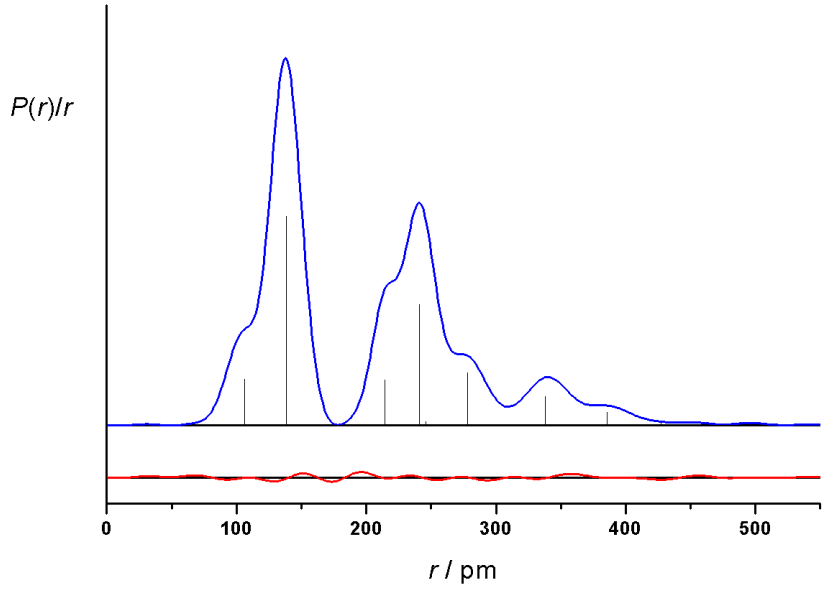

Figure 4.10 – Radial-distribution function for the r_g refinement, as in Figure 4.9, but omitting the data set recorded at a nozzle-to-camera distance of 180.5 mm.

4.5. Calculation of an experimental filter function

4.5.1. Data extraction

The data for the five benzene data sets were again re-extracted using the scaled electron wavelength (6.125 pm) and the corrected camera distances (180.5, 205.5, 230.5, 255.5 and 280.5 mm) as determined in **Section 4.3.2**. The data were taken

from the same area of the camera face for each data set, from a minimum radius of 6 mm to a maximum radius of 36 mm. As in **Sections 4.3** and **4.4**, the data were extracted using the UNEX program, but without the subtraction of an asymmetric background and correction for the assumed filter. The plate flatness correction was included, however.

4.5.2. Calculation of the ratios of observed to theoretical intensities

The ratio of the recorded intensity, $I_{observed}$, to the theoretical intensity, $I_{calculated}$, was calculated for each image. These are shown in **Figures 4.11** to **4.15** for each nozzle-to-camera distance, where the different coloured plots indicate data extracted from a separate image.

For all camera distances the experimental filter is approximately exponential, but with a smaller exponent than the assumed function and with significant oscillations. Once normalised, the data at any given distance are almost identical. The deviations from a smooth curve occur at different positions for each nozzle-to-camera distance, so are not due to irregularities in the filter. However, the same pattern in the maxima and minima is evident in all five figures, only expanded for those at longer nozzle-to-camera distances. These oscillations are therefore a consequence of either background scattering or the use of an inaccurate benzene structure for the generation of the theoretical intensities, as anticipated in **Section 4.1.2**.

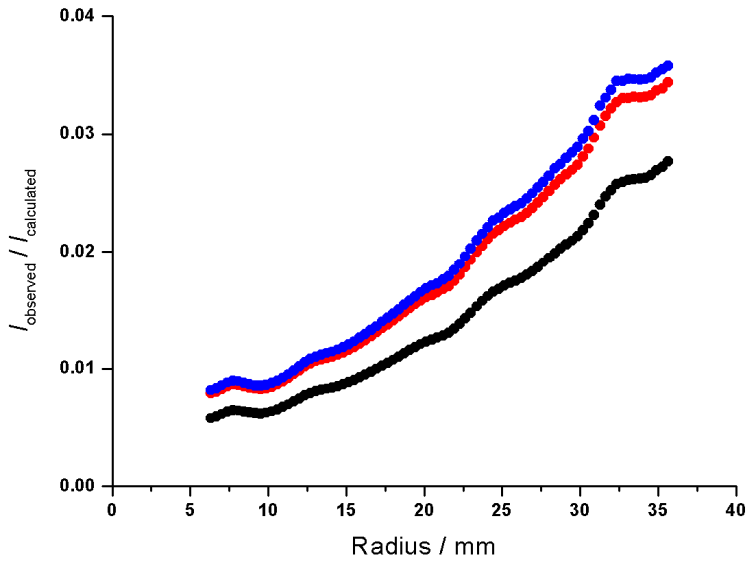

Figure 4.11 – Ratio of observed to theoretical intensities for three separate images as a function of the diffraction pattern radius at a nozzle-to-camera distance of 180.5 mm.

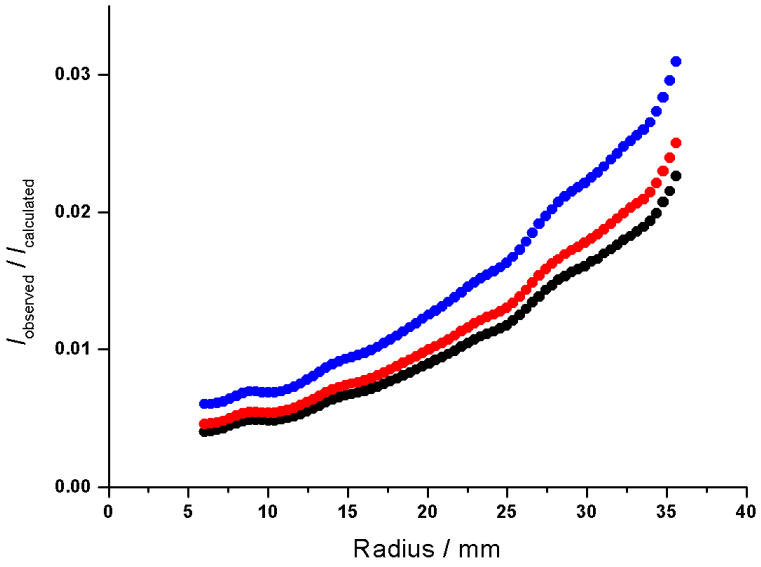

Figure 4.12 – Ratio of observed to theoretical intensities for three separate images as a function of the diffraction pattern radius at a nozzle-to-camera distance of 205.5 mm.

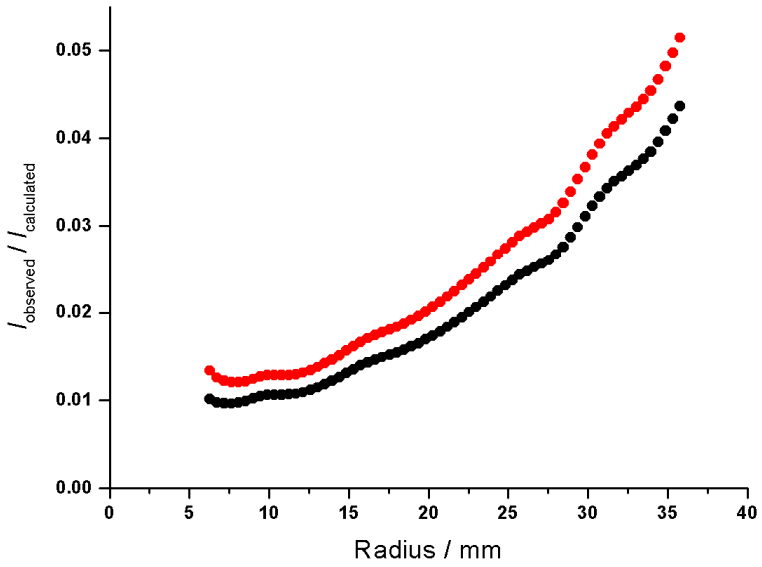

Figure 4.13 – Ratio of observed to theoretical intensities for two separate images as a function of the diffraction pattern radius at a nozzle-to-camera distance of 230.5 mm.

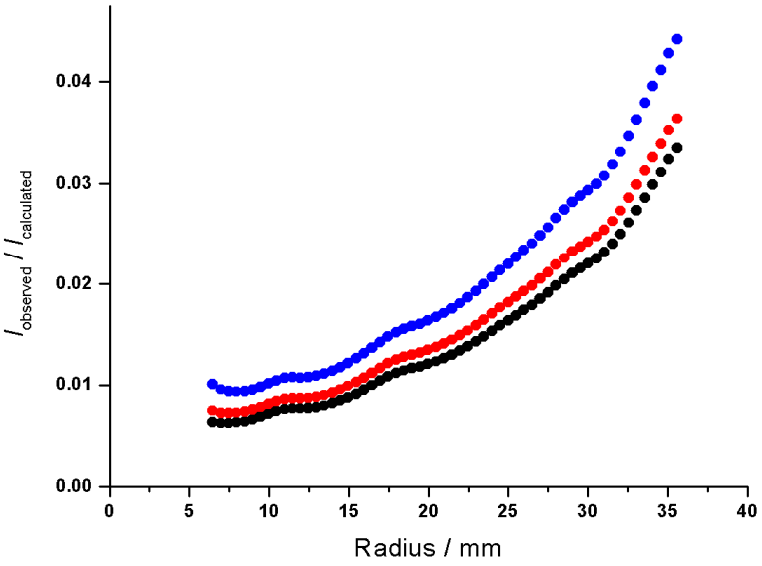

Figure 4.14 – Ratio of observed to theoretical intensities for three separate images as a function of the diffraction pattern radius at a nozzle-to-camera distance of 255.5 mm.

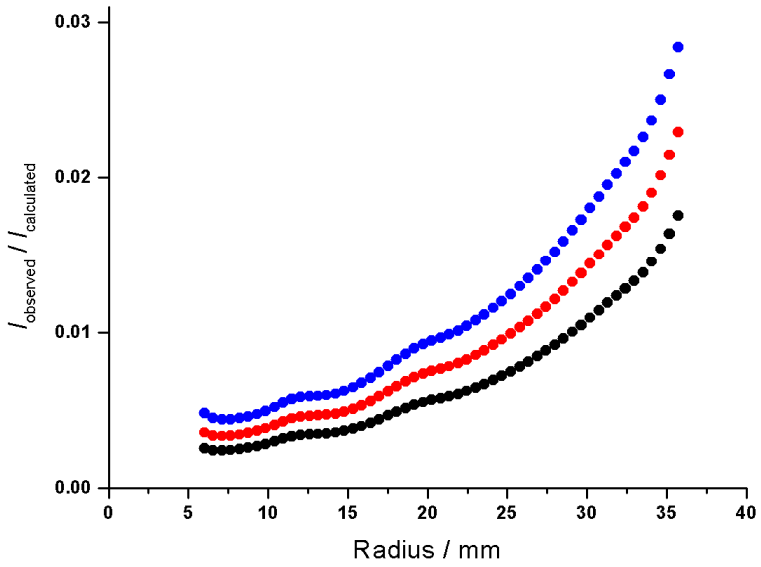

Figure 4.15 – Ratio of observed to theoretical intensities for three separate images as a function of the diffraction pattern radius at a nozzle-to-camera distance of 280.5 mm.

4.5.3. Calculation of an experimental approximation to the filter function

In **Figure 4.11** a large deviation from an exponential function can be observed at the edge of the data. This is in the same region as the data in **Section 4.4** appeared to be poor. The data from the shortest camera distance were therefore not used in the determination of a more suitable filter.

The intensity ratios ($I_{observed}$ divided by $I_{calculated}$) were averaged for each of the remaining nozzle-to-camera distances: 205.5, 230.5, 255.5 and 280.5 mm. These are plotted in **Figure 4.16,** where the average of the four curves is also shown. An exponential function was fitted to the average intensity-ratio curve and is given by **Equation 4.6**. This is compared with the original function (**Equation 4.5**) and an r^3 function in **Figure 4.17**.

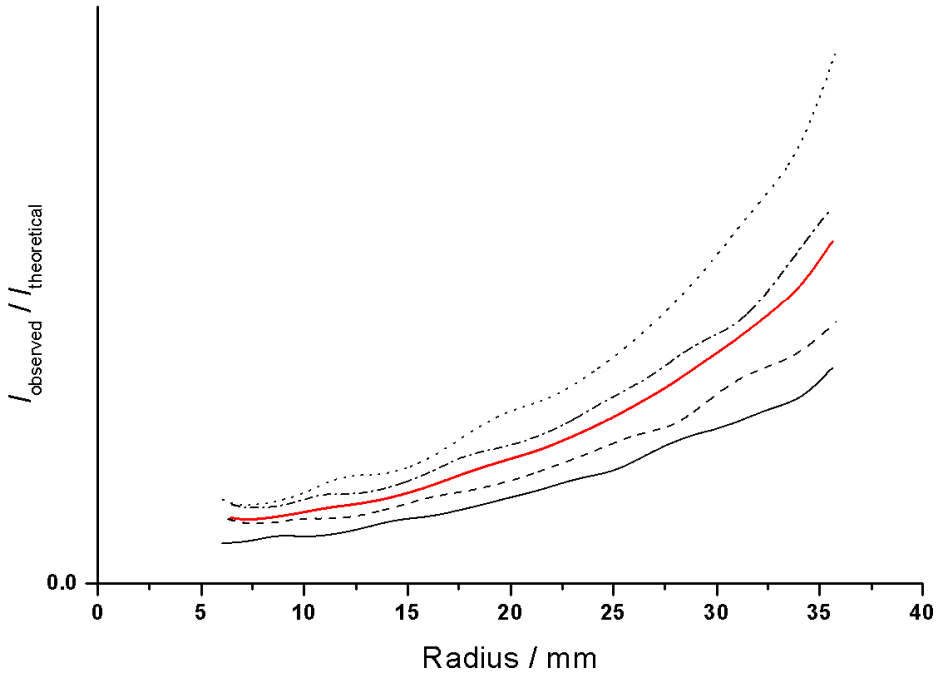

Figure 4.16 – Average intensity ratios (red) for data recorded at nozzle-to-camera distances of 205.5 mm (black, solid), 230.5 mm (dashed), 255.5 mm (dot and dash) and 280.5 mm (dotted).

$$\frac{I}{I_0} = 0.723 + \exp(0.07427 \times r) \tag{4.6}$$

One method of assessing the goodness-of-fit of the new function is to normalise the experimental data and correct it using the new function, where a perfect fit to a perfect data-set would yield a straight line at y = 1. This was done for the four experimental data sets in **Figure 4.16** and is shown in **Figure 4.18**. As before, the oscillations are clearly visible, but the curves for the data collected at 205.5 and 280.5 mm are approximately centred on y = 1. The data at the medium distances do not fit quite so well, but slope slightly downwards, perhaps indicating that the filter is not best described by an exponential function.

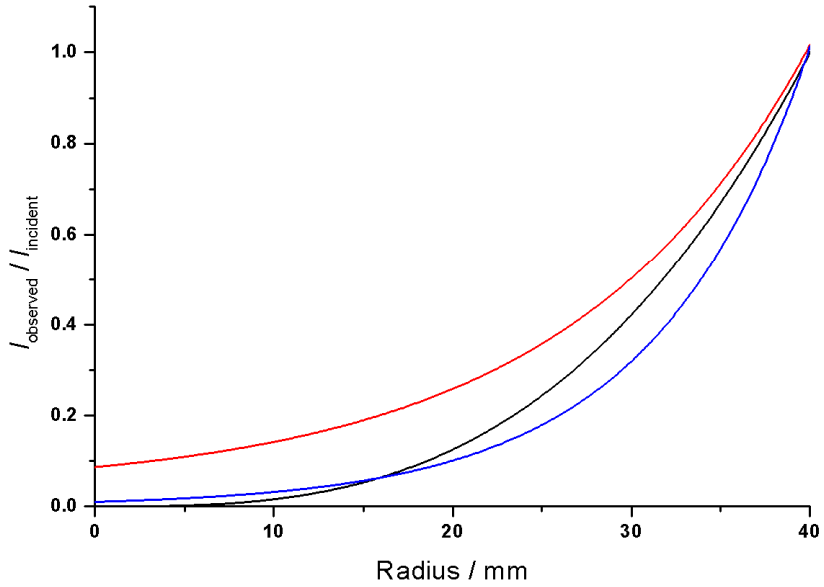

Figure 4.17 – New filter function (red) compared to an r^3 (black) and the assumed filter (blue).

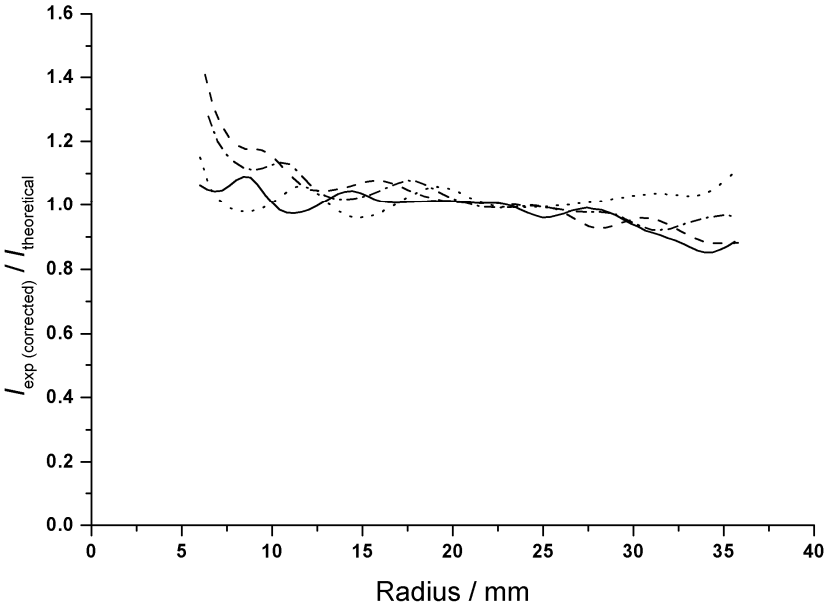

Figure 4.18 – Average intensity ratios corrected for the new filter function using data recorded at nozzle-to-camera distances of 205.5 mm (solid), 230.5 mm (dashed), 255.5 mm (dot and dash) and 280.5 mm (dotted).

4.6. Evaluation of the new filter function

The effectiveness of the calibration was assessed by attempting to repeat the determination of the electron wavelength and camera distances using the experimentally determined filter function.

4.6.1. GED procedure

Data for all five nozzle-to-camera distances were re-extracted using **Equation 4.6** as the filter function, allowing a misalignment of the centres of the filter and diffraction pattern. Refinements were performed for each distance using approximately the same data range as in **Section 4.3**, except for the refinement using data collected at 180.5 mm for which the s_{max} value was reduced to 180 nm^{-1}. The GED model was the same as that used in **Section 4.3**.

4.6.2. Results and discussion

The refined inter-atomic distances and root-mean-squared amplitudes of vibration are displayed in **Table 4.5** for all five nozzle-to-camera distances.

The first point to note is that despite having reasonably small standard deviations, the C–C distances are less consistent with one another than in **Section 4.3** (**Table 4.2**). Further calibration of the electron wavelength and nozzle-to-camera distances is therefore not feasible. The values obtained are scattered around the accepted value, however, indicating that the initial calibration of the camera distance was reasonably accurate.

The refined amplitudes of vibration are also highly variable, and some of them have large uncertainties, indicating that there is little information in the GED data about

Table 4.5 – Inter-nuclear distances (r_a) and amplitudes of vibration (u) obtained using Equation 4.6 as the filter correction.[a]

	180.5 mm		205.5 mm		230.5 mm		255.5 mm		280.5 mm		Calc.[b]
	r_a	u	r_a	u	r_a	u	r_a	u	r_a	u	u
C–C	140.2(2)	2.1(17)	138.8(1)	4.5(5)	139.6(1)	2.7(8)	138.6(1)	0.3(103)	135.9(2)	4.2(5)	4.53
C–H	108.8(2)	5.1(29)	107.7(1)	7.2(12)	108.3(1)	1.6(47)	107.5(1)	5.3(24)	105.5(1)	13.3(14)	7.56
C···C*meta*	242.8(4)	4.0(13)	240.4(2)	5.6(7)	241.8(2)	5.8(49)	240.0(2)	7.7(5)	235.4(3)	8.1(7)	5.43
C···C*para*	280.4(4)	8.7(12)	277.5(2)	11.5(9)	279.2(2)	11.9(6)	277.2(2)	11.2(8)	271.8(3)	13.3(10)	6.06
C···H*ortho*	216.2(3)	6.8(21)	214.0(2)	1.9(37)	215.3(1)	6.7(8)	213.7(2)	7.8(8)	209.6(3)	11.9(12)	9.76
C···H*meta*	341.4(5)	10.7(16)	337.9(3)	11.0(11)	339.9(2)	9.7(7)	337.5(2)	9.5(8)	330.9(4)	17.0(12)	9.37
C···H*para*	389.2(6)	10.9(31)	385.2(3)	13.6(25)	387.5(2)	11.8(13)	384.7(3)	12.8(16)	377.3(5)	22.9(32)	9.31
R_G	16.6%		9.2%		6.0%		5.8%		5.5%		

[a] All molecular dimensions in units of pm.

[b] Reference 5. Obtained at the B3LYP/cc-pVTZ level of theory.

these values. In general, the values obtained are closer to the calculated values than the refinements using data corrected with the original function. However, this should be expected, as the experimental filter function has a smaller contrast between the inner and outer regions, which will reduce the amplitudes.

The *R* factors are larger with the experimental filter but this may also be an effect of the data at large *s* values being relatively larger in magnitude rather than a poorer fit to the experimental data. This is because, rather than refining on the experimental intensities, the refinement is performed on $s^4 I_{mol}$. The original assumed filter was closer to s^3 and the experimental filter closer to s^2, so the contribution of experimental noise is roughly proportional to *s* for the first refinement, but roughly proportional to s^2 after data correction using the experimental filter function. It is possible that this factor is also playing a role in the variability of the C–C distance and the amplitudes of vibration.

4.7. Conclusions

A procedure for calibration of the electron wavelength, nozzle-to-camera distances and the optical filter in the CCD camera that has been installed in the SSED apparatus has been proposed using benzene scattering data. Using this procedure, the initial nozzle-to-camera distances were *ca.* 10 mm too short, with an uncertainty of *ca.* 3 mm whilst the scaling parameter to be applied to the electron wavelength was 1.018(12). An experimental filter function was also determined, but further attempts to improve the accuracy of the experimentally determined parameters by repeating the process yielded inconsistent values. At the time of writing it is not known whether the experimental filter correction is more accurate than that initially assumed.

The main difficulty is the presence of too many unknown quantities, all of which are correlated to some unknown extent, to eliminate any of the potential problems with

the filter determination systematically. The initial refined amplitudes of vibration are too large to correspond to the true structure, but there are three possible causes:

1. The filter correction is too large for the data at small scattering angles.

2. The scattering volume is too large for the assumption of a point source.

3. The diffraction patterns are not centring correctly.

If either of problem numbers two or three is present, the intensities used to calibrate the filter are incorrect and could easily account for the shallower experimental filter correction. The misalignment of the centres of the filter and the diffraction pattern will cause an error in the centring procedure, but without knowing an accurate filter function, the misalignment cannot be known accurately.

Additional, but less serious concerns, are that it is not known how symmetric the filter is and how large any contributions are from a less than uniform coating of the phosphor and aluminium. Also, the degree of stability of the high voltage supply is unknown. A small drift in the bias voltage used to control the beam current (see **Chapter 3**) has been noticed on occasions, which may be indicative of a larger drift in the high voltage supply, providing an alternative source of error in the calibration procedure.

4.8. Recent work and suggestions for the future

As an extension to the work presented in this chapter, various attempts have been made to improve the calibration procedure. These include using carbon tetrachloride in place of benzene as the greater number of oscillations in the molecular-intensity curve ought to provide a better handle for determining the nozzle-to-camera distances. This revealed an odd contraction of the data about the centre of the data set

and is discussed in **Chapter 5**. Data extraction using the XPKG program has been compared with that using the UNEX code and small (but for the moment insignificant) differences in the data were observed. The XPKG program experiences difficulties locating a centre for the diffraction pattern, probably due to the presence of the beam stop and for this reason takes considerably longer to obtain a full data set.

A Fortran program has been written to modify theoretical scattering curves to account for a finite beam width with a Gaussian profile and for an error in the centring procedure, albeit in an approximate manner. (This is included in **Appendix 2**.) This has been investigated for CCl_4 data (see **Chapter 5**) and the relatively large beam width is currently the suspected cause of the observed data contraction. Preliminary refinements on theoretical curves for benzene generated in this way show good agreement with those obtained after application of the improved filter function and provides a lead for further investigation. These modified theoretical curves would also be an improvement over the unmodified ones for the calculation of the theoretical intensities for the filter calibration stage, although the extent of this improvement has not yet been gauged.

On the experimental side, an improvement in the focus of the electron beam is clearly one way to eliminate errors. Insertion of a cleanup aperture close to the scattering point, as is found in conventional GED apparatus, would reduce scattering from background gas, and should enable a more accurate filter function to be determined.

Finally, once a reasonably reliable filter function has been established, it may be best to calculate a correction to the filter function, allowing a misalignment of the diffraction and filter centres, rather than attempting to calculate the absolute function.

4.9. References

1. H. Fleischer, D. A. Wann, S. L. Hinchley, K. B. Borisenko, J. R. Lewis, R. J. Mawhorter, H. E. Robertson and D. W. H. Rankin, *Dalton Trans.* (2005), 3221.

2. Y. V. Vishnevskiy, *J. Mol. Struct.* (2007), **833**, 30.

3. S. L. Hinchley, H. E. Robertson, K. B. Borisenko, A. R. Turner, B. F. Johnston, D. W. H. Rankin, M. Ahmadian, J. N. Jones and A. H. Cowley, *Dalton Trans.* (2004), 2469.

4. SCATTER version 0.0.5. Developed by J. K. Dewhurst.

5. S. Gundersen, S. Samdal, T. G. Strand and H. V. Volden, *J. Mol. Struct.* (2007), **832**, 164.

Chapter 5

Recent and future work

5.1. Overview

At the time of writing (December 2007) the Edinburgh SSED apparatus has been used to collect data for a few simple compounds (benzene, carbon tetrafluoride, carbon tetrachloride, 1,2,4,5-tetrafluorobenzene and $CF_3CO_2CH_2CF_3$) using a conventional needle nozzle. In contrast to earlier work,[1] where data were collected at a single nozzle-to-camera distance, data have been collected at at least three camera distances for each compound. This provides a much more stringent test of the quality of the data as irregularities cannot be overlooked so easily.

Attempts to determine the minimum required vapour pressure using toluene and attempts to observe diffraction using the supersonic molecular beam have not yet had any success due to relatively high background noise. Some progress has been made reducing the background and this could be improved further, as detailed in **Section 5.2**.

Currently, the most significant problem is with the measured scattering intensities. This was alluded to in **Chapter 4** and is explained more fully in **Section 5.3**. A number of attempts have been made to determine the cause and the main contributor is thought to be a large beam width. However, it is possible that there are a number of other problems, such as diffraction pattern centring errors, background scattering and uncertainty of the true filter function. The clearest way to make progress is on the experimental side, by improving the focus of the electron beam and by reducing the scattering from background gas. If this does not solve the problem, it will at least reduce the number of possible sources of error.

Finally, some ideas regarding the use of the molecular beam have been presented in **Section 5.4**. The main concerns have been highlighted and an attempt to assess their relative importance has been made.

5.2 Background scattering

There are three sources of background that are present in the SSED data: light from the electron gun filament, scattering from surfaces and scattering from background gas. These are dealt with below, each in turn.

5.2.1. Light from the electron gun filament

From the literature reviewed in **Chapter 1** it appears that the aluminium coating would need to be a factor of 10 thicker to prevent light reaching the CCD. This can be compensated for by recording a background image of the same exposure time and subtracting this from the sample image. However, in order to observe diffraction using the supersonic molecular beam, longer exposure times than have previously been used will be required and the background light may become a significant proportion of the total. Moreover, when the electron gun filament is illuminated without a beam tube in place, the background from light becomes significant even at short (< 20 s) exposure times. Insertion of an aperture *ca*. 2 mm in diameter along the electron beam path, just before the nozzle, could serve to purposes. It would remove the light that is not directed at the beam stop as well as reducing the electron scattering from any residual gas along the electron beam line.

5.2.2. Extraneous scattering

The background electron scattering was the first serious problem observed on installation of the new CCD camera. A number of possible sources were possible, such as scattering from the nozzle, scattering from the apertures in the beam tube, reflections from the beam stop and background X-rays generated by such collisions. Scattering from the nozzle can be ruled out as the high background persisted even when the nozzle was removed. The beam tube apertures were painted with colloidal carbon, left to dry and the background retested, but without noticeable improvement.

It therefore appeared that the scattering was from the beam stop, although whether it was due to scattered electrons or due to X-rays was unclear.

The beam stop was originally designed to be only about 7 mm deep, as a longer trap would risk a collision with the gate valve that can be used to separate the detector chamber from the rest of the apparatus. Early work by Brockway and Bartell[2] (**Figure 5.1**) seemed to indicate that this would be sufficient for a conventional apparatus, although their beam trap was a different shape.

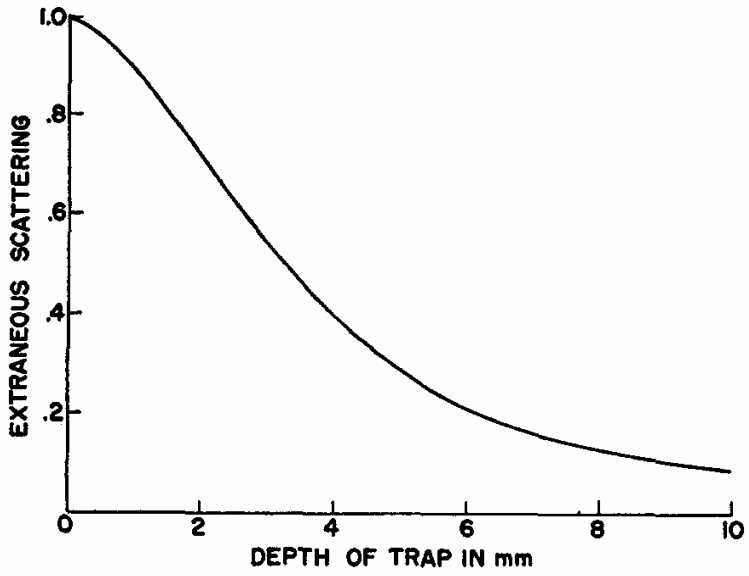

Figure 5.1 – Brockway and Bartell's estimation of background scattering as a function of the depth of a beam stop, 2 mm in diameter (reference 2).

The first attempt to reduce the background was by spraying the beam stop with carbon particles and this reduced the background marginally. Next, two more cups were designed to replace the original V-shaped copper cup; they can be seen in **Figures 5.2** and **5.3**. These were made of aluminium as it was anticipated that, due to its lower atomic number, aluminium would create fewer X-rays. Due to the softness of aluminium and in the interest of time, the new traps were not created with sharp edges at the rims. This may be a disadvantage as it increases the surface area at the rim which is especially true for the larger trap. However, the trap diameters are

sufficiently large that the electron beam intensity should be many orders of magnitude smaller than at its centre. In addition, it is not clear whether sharp edges are beneficial or not. This is because the presence of stray diffusion or rotary pump oil will cause charge build up on surfaces and the resulting local electric fields will be stronger at sharp points and edges.

Figure 5.2 – Removable collector cups tested. From left to right: Original V-shaped copper cup coated in graphite particles; 10 mm deep, flat-bottomed aluminium cup and 20 mm stepped aluminium cup.

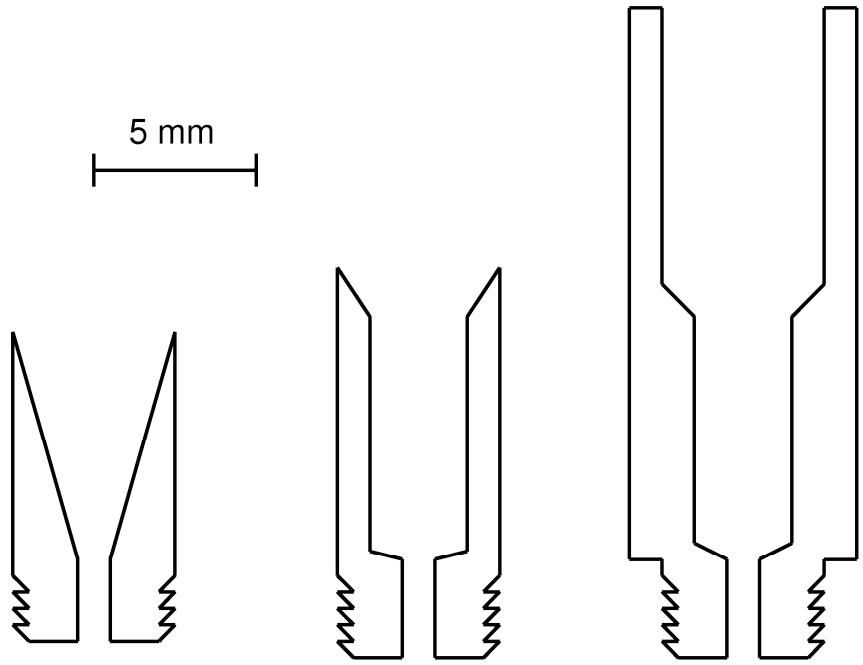

Figure 5.3 – Cross-sections of the three beam stops tested. Approximately to scale.

Both of the new cups reduced the background substantially and the longer beam stop, which was slightly more effective than the shorter one, reduced the scattering to about 10%. The background for benzene and CCl_4 is therefore no longer a large proportion of the total, but when data acquisition for toluene was attempted as a test of the minimum vapour pressure required, background scattering again became a problem.

It is still unknown whether the improvement in efficiency was due to the substitution of aluminium for copper, or the greater depth of the trap. In this respect it would be interesting to compare the background for two identical beam stops, one made of copper and one of aluminium. If this is shown to be important, it would be wise to also make the Faraday cup out of aluminium.

In his work with cluster beams, Bartell found that his beam stop had to be lengthened to 60 mm.[3] Therefore, in order to observe diffraction using a supersonic beam using the SSED apparatus, a longer beam stop will almost certainly be required. However, the base of the beam stop cannot support an attachment of this size and a new base will be required. Currently, only 1-2 mm of thread is available to secure the attachment to the base, but in order to position the trap coaxially with the electron beam at least another 2 mm is probably required. In addition, for a much longer trap the base must be joined accurately to the supporting arm and this may require an alternative to simply welding them together.

One way of circumventing these problems is by adopting a Woods' horn design, which is simply a curved metal tube that the electrons are directed into. Being curved, the electrons cannot be reflected out of the trap, but are directed further down the pipe. This is a much simpler design than that currently adopted, so it would be easy to make and would almost certainly reduce the background. (A simple first attempt could be to bend a copper pipe, 3 mm outer diameter as used for the beam stop arm, into an arc and widen the end that would capture the electron beam.) However, its drawback is the lack of an effective method of centring the electron

beam. This could be done by recording the voltages required to steer the beam onto the rim of the horn, which could be determined by observing the background scattering, then calculating an approximate centre, or alternatively, by minimising the background. This problem makes this type of beam stop unsuitable for the calibration of the camera filter described in **Chapter 4**, as the electron beam ought to be placed at the same position on the camera face for each nozzle-to-camera distance.

Other improvements to the beam-stop design are also possible. Initially, the diameter of the base was kept to a practical minimum in order to maximise the range of data available. However, it has been found that the camera saturates very quickly at the small angles and these data are not of much use. In addition, the high intensities at these small angles induces readout noise in the data, which is one of the limiting factors for the maximum beam current that can be used. A wider base is therefore recommended.

5.2.3. Background gas scattering

This was not initially a concern as the background scattering appeared to be strongest at the edge of the data and, after correction for the optical filter, was approximately uniform over the camera face. If the scattering was coming from background gas, however, it would be much stronger at the centre of the camera. In contrast to background noise from light or scattering from the beam stop, the data cannot be corrected for scattering by background gas by a simple subtraction of a background as it is likely to change as the gas inlet is opened. In addition, without having an accurate calibration of the filter (**Chapter 4**) it is difficult to determine the contribution to the background from this source, but conversely, the filter cannot be calibrated accurately if it represents a significant proportion of the signal.

The electron-scattering intensity of a gas is approximately proportional to θ^{-4} (θ is the scattering angle), so background gas near to the electron gun is far more significant than that in the vicinity of the detector. Insertion of a collimating aperture

immediately in front of the nozzle position, as is often present in a conventional GED apparatus,[2] would lessen this concern as well as reducing the noise due to light from the filament. A sophisticated method of implementing this would be to incorporate such an aperture into a beam tube in a similar way to the centring collars (**Figure 3.12**) used to initially align the electron beam. If a current could be read from this aperture, the total beam current could be easily determined, as it would require only a small deflection of the beam. The beam size could therefore be estimated using the method in **Section 3.5.2**, without risk of damaging the camera phosphor and the measurement could be made during the course of an experiment. As with all apertures, scattering from its edges would be a concern and it should therefore have a diameter at least a few times wider than electron beam diameter. Care would have to be taken that such an aperture can be easily cleaned so that it does not acquire charge, which would distort resulting diffraction patterns. The aperture should also be grounded during data acquisition, rather than remain connected to an electrometer.

Further improvement of the background pressure in the main chamber would also reduce the contribution from background gas. The pressure in this chamber is about 2×10^{-5} mbar and falls to about 1×10^{-5} mbar when a cold finger is present. Ten years ago, the pressure was as low as 5×10^{-6} mbar using the same vacuum system, so some improvement is possible. Some degradation of the pumps may have occurred over that time, however, and perhaps just as likely, the accuracy of the ion gauge used to determine this pressure may have drifted. In addition to searching for leaks (this has been attempted using a spectroscopic leak detector, but no leaks have been found, probably due to the large volume of the chamber) the water-cooled baffle on the oil diffusion pump could be replaced with one that does not hinder the gas flow. In addition to helping to remove the background scattering, this may be required to provide the pumping capacity for optimisation of the molecular beam intensity, outlined in **Section 5.4.2**.

5.3 The data problem

5.3.1. Outline of the data problem

An initial calibration of the filter in the new camera was performed using benzene data and scaling of the electron wavelength was achieved using known differences between the camera distances. When the data were re-corrected for the new filter the refined C–C distances were inconsistent with one another but, on the whole, the amplitudes of vibration were closer to the accepted values, indicating that the new filter function was an improvement on that originally assumed. For all data sets, the uncertainties of amplitudes of vibration were extremely high, however, and the refined values of some amplitudes of vibration were significantly smaller than accepted values.

5.3.2. Investigation of carbon tetrachloride data

For benzene, the largest peak in the radial-distribution curve (RDC) is that corresponding to the C–C distance of 140 pm, so the spacing of the peaks in the molecular intensity curve is *ca.* 45 nm^{-1}. The benzene data sets were collected for an *s* range of about 130 nm^{-1}, meaning that only two or three peaks were visible. In contrast, the largest peak in the RDC for CCl_4 is the non-bonded Cl···Cl distance at about 290 pm, so twice as many peaks in the molecular intensity curve ought to be clearly visible, resulting in more precise nozzle-to-camera distances and amplitudes of vibration.

Data were collected for CCl_4 and corrected using the experimentally determined filter. For most nozzle-to-camera distances, the amplitudes of vibration were worse than those for benzene and in many cases could not be refined unrestrained. However, with the amplitudes tightly restrained to literature values the C–Cl distances were reasonably consistent. More interesting, however, was the odd appearance of the data, as can be seen in **Figure 5.4**, where the data seem to be

contracted about the centre. The discrepancies in the amplitudes of oscillation were deemed to be of secondary importance. This indicates two main problems: a scaling error in the electron wavelength or camera pixel size and a shift of the whole data set. Rescaling and constraining the C–Cl distance to compensate for the scaling error revealed an apparent data shift of *ca.* 4 nm^{-1}, which was reasonably consistent between data sets.

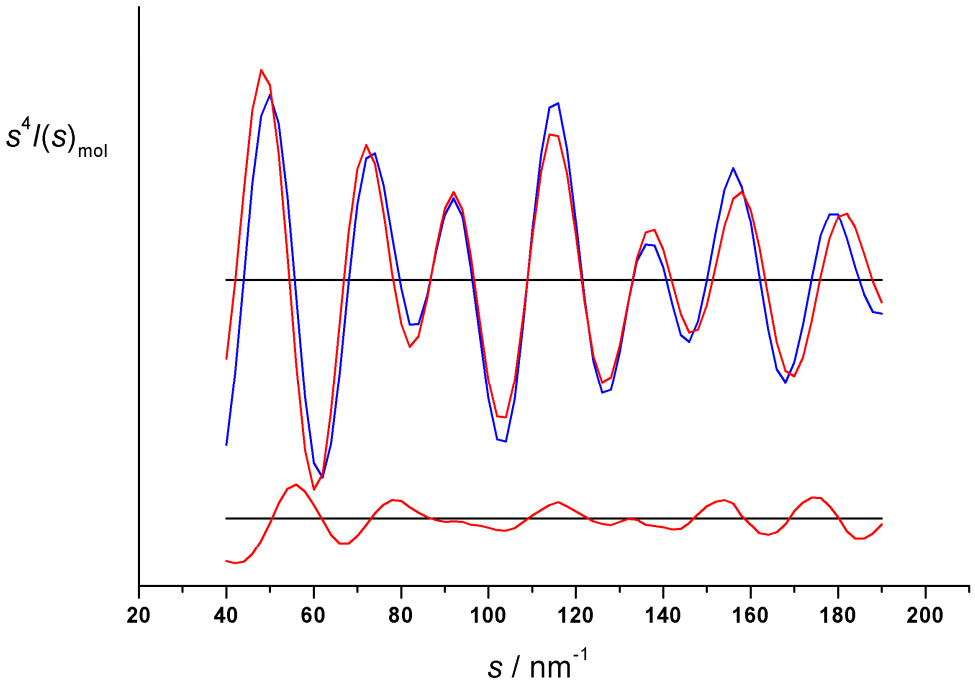

Figure 5.4 – Apparent contraction of the experimental (blue) molecular-intensity data relative to the theoretical intensities (upper red) for carbon tetrachloride. Data collected at a camera distance of *ca.* 150 mm. Only the C–Cl distance refining, whilst the C–Cl and Cl···Cl amplitudes were fixed at 5.05 and 6.96 pm, respectively.

Upon this discovery, data obtained for benzene and 1,2,4,5-tetrafluorobenzene were reanalysed without refining amplitudes of vibration, which hinted at a similar effect, although the magnitudes of the relative errors in the scaling and data shift were difficult to assess. In addition, the data obtained for 1,2,4,5-tetrafluorobenzene by

Papathomas[1] about 10 years ago, obtained using a different camera set-up and data extraction procedure also exhibited a contraction of the data about the centre, although data for CF_4 obtained at that time seemed to better resemble the theoretical intensities.

Several reasons were postulated for the data shift, some of which could be ruled out, whilst the effects of others were investigated.

- An error preparing data for reading into the ed@ed refinement program. This could be ruled out as the data were handled in different ways when extracted using XPKG[2] and UNEX,[3] both of which yielded similar results.

- Misalignment of the filter and diffraction centres or an error in the estimation of this misalignment. This would result in incorrect amplitudes of vibration, but would not result in a shift of the data set. However, it would be likely to cause an error in the determination of the centre of the diffraction pattern (see below).

- An error centring patterns. As electron scattering intensity is approximately proportional to s^{-4}, pixels corresponding to a given estimated s value would be weighted much more heavily if the value of s was overestimated than if it was underestimated, resulting in a shift of the data, especially those at small s-values, for which the relative error would be greatest. This would not be a problem in conventional GED, as the recorded intensities are approximately uniform, due to the presence of the rotating sector. As the filter function here is exponential, however, only the data in the outer regions, where its gradient approaches r^4, would be compensated for in this manner. However, the approximate shift of 4 nm^{-1} in s equates to about 0.5 to 1 mm on the camera face or about ten camera pixels and it was thought that the centre was better determined than this. In addition, data were extracted from an image of CCl_4

in segments of 45 degrees and although a small variability in the peak positions was observed, it was much smaller than those shown above.

- Width of the electron beam. A large electron-beam width would have a similar effect to an error in the determination of the diffraction centre. The electron beam width was known to be less than ideal, with a standard deviation of about 0.5 mm (**Chapter 3**) rather than approximately 0.1 mm in a typical GED experiment. In contrast to the centring error, the electron-beam width is therefore on the same scale as the data problem. In order to gauge the effect of a finite beam size, a Fortran program was written to generate a simulated curve from a theoretical intensity curve. Although several assumptions were made (see **Appendix 2**) and this procedure can certainly be improved upon, this serves as a reasonable first approximation. One of the assumptions invoked was that of a Gaussian beam profile and CCl_4 data for a beam with a standard deviation of 0.5 mm (*ca.* 1.2 mm FWHM) were generated, and subsequently treated in a similar manner to an experimental data set. The refined molecular-intensity curve is shown in **Figure 5.5**, where a small contraction of the data can be seen, but on a much smaller scale than the experimental data contraction.

- The presence of local electric fields. It is possible that some part of the apparatus became charged by the electron beam during the course of the experiment. The charging of an aperture along the beam line or the beam stop would cause it to act as a lens. However, data had been collected using a range of beam currents, from *ca.* 0.1 to 1 μA and no correlation between the data quality and the beam current has been observed.

- The presence of magnetic fields. A uniform magnetic field such as that of the earth could not result in the observed effect. The component of the field perpendicular to the electron beam would move the centre of the diffraction pattern without affecting its shape, whilst the component parallel to the

electron beam would result in spreading of the diffraction pattern, the degree of which would be proportional to the sine of the scattering angle. The calculations presented in **Chapter 3**, showed minimal deflection of an electron beam due to the earth's magnetic field at the experimental energies over the length of the apparatus. In addition, the velocity component perpendicular to the electron beam due to the scattering event is much smaller than the incident electron-beam velocity, and so the spreading of the diffraction beam due to the earth's magnetic field will be orders of magnitude smaller than the beam displacement. A strong local magnetic field could cause this effect, but care was taken to eliminate magnetically susceptible components from the apparatus, so there does not appear to be any possible source of such a local field.

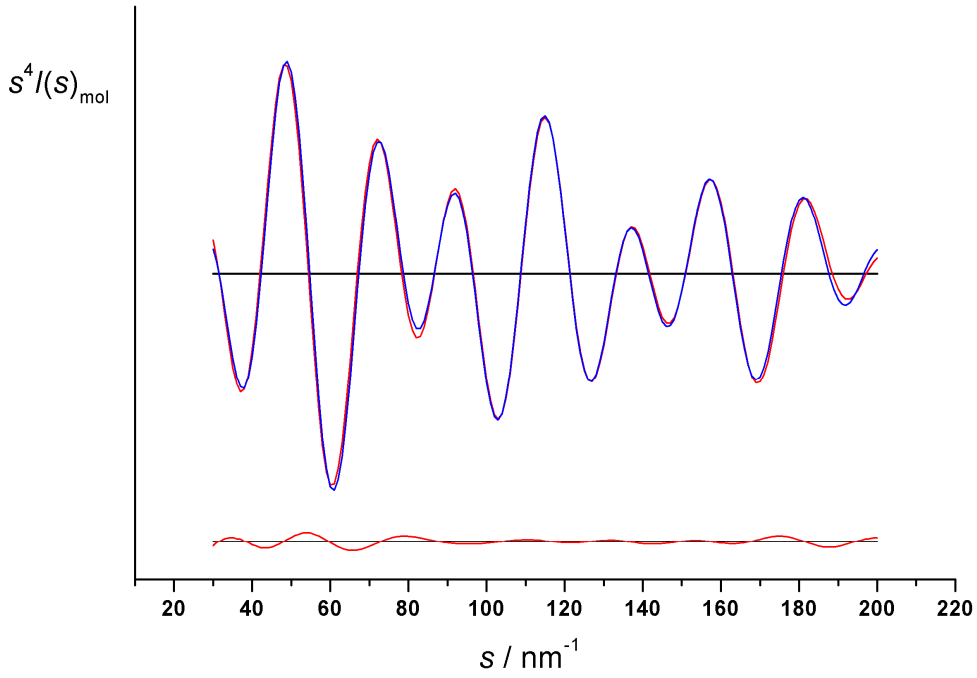

Figure 5.5 – Simulated CCl_4 molecular-scattering data (blue) for a Gaussian electron beam with a standard deviation of 0.5 mm.

- Distortion of the fibre optic taper within the camera. No calibration of the optical taper has been performed and a difference in magnification strength at its edges compared with the centre would result in a distortion of the data. The data presented by Papathomas[1] for 1,2,4,5-tetrafluorobenzene using a different detection system show a similar contraction of the data, suggesting that the new camera is not the source of this problem. It would be possible to test for a distortion of the filter by placing a metal plate containing an array of accurately spaced holes over the camera face and illuminating.

- Background gas. It has been a concern that gas is accumulating in the beam tube during the course of an experiment. Due to the presence of apertures beyond the scattering point, only the inner data produced in this way would reach the camera, shifting the data at small *s*-values. This could be eliminated as described in **Section 5.2.3**.

It was not known how accurate the electron-beam size estimate of 0.5 mm was, as it was possible that secondary electrons were released from the beam-stop aperture and the validity of a Gaussian beam shape is also questionable. Data were therefore also simulated for a larger electron beam, with a standard deviation of 0.75 mm. In contrast to data for a 0.5 mm beam, where all parameters were able to refine, only the C–Cl distance could be refined, as was found for the experimental data. The resulting molecular-intensity curve is shown in **Figure 5.6** and the refined parameters for both simulated data sets are shown alongside the initial parameters in **Table 5.1**.

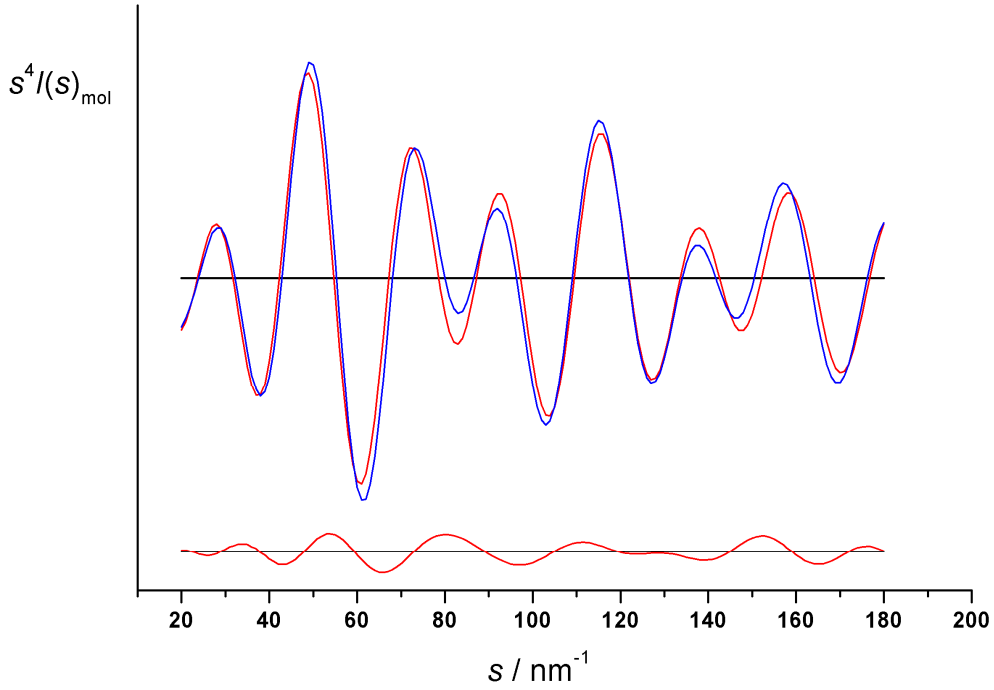

Figure 5.6 – Simulated CCl_4 molecular-scattering data (blue) for a Gaussian electron beam with a standard deviation of 0.75 mm (approximately equivalent to 4 nm^{-1} at a nozzle-to-camera distance of 200 mm).

Table 5.1 – Molecular parameters (in pm) for CCl_4, determined using simulated data for large electron beam widths.

Beam size [a]	0.50	0.75	Initial parameters
r_g C–Cl	176.04(4)	175.12(11)	176.60
u C–Cl	2.37(63)	5.05 [b]	5.05
u Cl···Cl	6.72(11)	6.96[b]	6.96
R_G	7.70%	19.20%	n/a

[a] Standard deviation in mm.

[b] Fixed to initial parameter value.

The data contraction in **Figure 5.6** is more evident than that in **Figure 5.5** and the error in the C–Cl distance is greater than for a 0.5 mm beam. Unexpectedly, the errors in the oscillation amplitudes are reasonably similar to those in the experimental data in **Figure 5.4**. In particular, the peak at 115 nm^{-1} is too large in both cases, but the peaks either side of this are too small. Also of interest are the values of the refined C–Cl distances. In both cases these refined to values less than the real ones, by 0.56 and 1.48 pm for a 0.5 and 0.75 mm beam, respectively. It is therefore likely that the nozzle-to-camera distances and scaled electron wavelength, determined in **Chapter 4**, are inaccurate and that this might also be the reason for the inconsistencies in the nozzle-to-camera distances after the experimental filter had been determined.

In conclusion, the similarities in the molecular-scattering curves in **Figures 5.4** and **5.6**, and the similar difficulties encountered when refining molecular structures for the simulated data sets indicate that the electron beam size is at least a significant problem, if not the root of the difficulties uncovered in **Chapter 4**. A mechanism is in place in the telefocus electron gun to focus the beam without breaking vacuum and without having to dissemble the gun. This allows the distance between the anode and the Wehnelt cap, Wehnelt cylinder and filament assembly to be varied by about 1 cm and an improvement in the focus has been attempted using this method. Currently, this distance is set to the maximum and reducing it worsens the focus. This implies that the filament and Wehnelt cap are positioned too far forward in the Wehnelt cylinder, as it has been observed[5,6] that the anode to filament distance is crucial to the beam focus whilst the position of the Wehnelt cylinder is of secondary importance.

5.4. Optimisation of the molecular beam for SSED

No progress has been made in the optimisation of the molecular beam since the work documented by R. Fender.[7] This included a mention of the observation of electron scattering from a molecular beam (5% CO_2/He), although no structural data were observed. This work was carried out by P. Papathomas who reported no further improvements.[1] Two attempts have since been made to observe diffraction using a molecular beam. In conjunction with the old phosphor screen and a brass beam tube with an entrance hole 1.6 mm in diameter and an exit hole 1.9 mm in diameter a molecular beam of CF_4 produced an observable increase in the background, but no observable structural data. The increased background was attributed to a build-up of stagnant gas in the beam tube. Upon installation of the new CCD camera the 5% CO_2/He mixture was retested, but using a beam tube with an open collision zone to reduce the build-up of gas in the beam tube. In this case, no electron scattering was observed, which was attributed to the low scattering intensities compared to the background.

This problem of extraneous electron scattering will certainly require attention before any meaningful data will be obtained using the supersonic nozzle and is dealt with in **Section 5.2**. However, in addition to this problem, there are three key issues relating directly to the use of the molecular beam: the alignment of the molecular and electron beams, maximisation of the absolute gas density at the intersection, and the relative densities of stagnant molecules in the beam tube to those at the scattering point.

5.4.1. Maximisation of the overlap of electron and molecular beams

A poor alignment of the electron and molecular beams was previously proposed[1,7] as the most significant problem, preventing the effective implementation of the molecular beam in the SSED apparatus. However, the FWHM of the electron beam is estimated to be at least 1 mm and, based on geometric considerations, a

conservative estimate of the molecular beam size is *ca.* 0.8 mm. (As this assumes no inter molecular collisions, the real molecular beam will probably be larger.) Both beams were aligned with the centre of the beam tube so that the misalignment of the centres of the two beams is not likely to be more than about 1 mm. Even at this extreme there should, therefore, still be significant overlap of the two beams. Rather, the main problem is most likely the maximisation of the beam intensity. (Both authors have misquoted the attainable gas densities available from the molecular beam source as being a thousand times greater than that of a conventional nozzle, whereas the literature reviewed in **Section 2.4** states the opposite and this may be the source of some confusion.)

The optimisation of the overlap is, however, likely to be significant and it is instructive to observe how other groups have tackled this problem. In most cases collecting plates have been mounted just outside the region for data collection and the recorded current maximised by displacement of the gas beam as a determination of the maximum overlap. If the magnitude of the displacement is also known an estimate of the molecular beam shape can be made, as shown by Bartell,[8] although some deconvolution of the data would be required for a reliable estimate. The setup of the SSED apparatus requires the molecular beam position to be fixed, but the electron beam could, instead, be displaced in order to maximise such a scattered current. However, this procedure would not be compatible with the suggestion of an active collimating aperture (**Section 5.2.3**) and one or the other would have to be adopted. The aperture method would ensure a centred electron beam and, as long as the molecular beam was centred, an alignment of the two. On the other hand, there is a chance that the ensuing loss of flexibility could be catastrophic.

5.4.2. Optimisation of molecular beam intensity

The skimmer that has been used so far is one built by Beam Dynamics, has an orifice diameter of 0.18 mm and is 25 mm in length. In contrast, Bartell opted for a skimmer diameter of 2 mm with an optimal length of only about 3 mm.[8] Eventually, the

conical skimmer conventionally used in molecular beam experiments was abandoned altogether, and a V-shaped skimmer was adopted in order to position the skimmer orifice as close as possible to the electron beam.[9] Investigation of shorter skimmers with a wider aperture may be required, in order to provide high enough target densities of molecules to satisfactorily overcome the background noise.

5.4.3. Accumulation of molecules in the beam tube

The scattering from background gas is a major concern as this was the first major obstacle encountered by those attempting to introduce a molecular beam into an electron diffraction apparatus.[10] They found that pressures of 10^{-5} to 10^{-6} Torr were too high for such an experiment, although this was before the optimisation of the gas delivery system outlined above. The SSED apparatus is designed to overcome this problem by maintaining a low vacuum (10^{-7} Torr) along the electron beam path, but allowing the remaining chambers to have higher pressures, which is facilitated by the presence of the beam tube. This approach has not previously been tried and, given the sensitivity of the technique to background noise, even a small accumulation of molecules in the beam tube may prevent the recording of any useful information. The placement of an aperture in the beam tube, as suggested in **Section 5.2.3**, would provide an additional benefit in this respect, as it would hinder molecules entering the beam tube.

5.5. Conclusions

There are a number of challenges to be tackled before high quality data will be obtainable for cooled molecular structures in a supersonic beam using the Edinburgh SSED apparatus. However, the main problems and specific future obstacles have now been identified, and with some further reduction of background intensities, narrowing of the electron beam size and some optimisation of the skimmer for the molecular beam this goal should be obtainable. The road to the ambitious goal of

obtaining structures of excited states is less clear and the specific challenges regarding this application are likely to be more than those briefly outlined at the end of **Chapter 2**. Nonetheless, this also remains an exciting future goal which, given the enormous scope of applications in structural and computational chemistry, deserves further consideration.

5.6. References

1. P. Papathomas, Ph.D. thesis, *University of Edinburgh* (1998).

2. L. O. Brockway and L. S. Bartell, *Rev. Sci. Instrum.* (1954), **25**, 569.

3. H. Fleischer, D. A. Wann, S. L. Hinchley, K. B. Borisenko, J. R. Lewis, R. J. Mawhorter, H. E. Robertson and D. W. H. Rankin, *Dalton Trans.* (2005), 3221.

4. Y. V. Vishnevskiy, *J. Mol. Struct.* (2007), **833**, 30.

5. High Energy Electron Scattering, Chapter 7, R. A. Bonham and M. Fink. *Van Nostrand Reinhold Co.* (1974), ACS Monograph 169.

6. H. Schmoranzer, H. F. Wellenstein and R. A. Bonham, *Rev. Sci. Instrum.* (1975), **46**, 89.

7. R. S. Fender, Ph.D. thesis, *University of Edinburgh* (1996).

8. L. S. Bartell, R. K. Heenan and M. Nagashima, *J. Chem. Phys.* (1983), **78**, 236.

9. L. S. Bartell and R. J. French, *Rev. Sci. Instrum.* (1989), **60**, 1223.

10. B. Rault and J. Farges, *Rev. Sci. Instrum.* (1973), **44**, 430.

Chapter 6

Molecular structures of *arachno*-decaborane derivatives by GED and *ab initio* calculations – the effect of isolobal substitution on the local geometry

6.1. Introduction

The families of *nido*- and *arachno*-decaboranes are both structurally related to icosahedral [*closo*-$C_{12}H_{12}]^{2-}$ by removal of two adjacent vertices. They differ, however in the number of skeletal electron pairs, so that the neutral parent compounds for each of the two families are $B_{10}H_{14}$ and $B_{10}H_{16}$, respectively. Whilst *nido*-$B_{10}H_{14}$ has been known for a long time and was characterised by GED in 1951,[1] *arachno*-$B_{10}H_{16}$ has never been observed and it is thought that two of the four bridging hydrogen atoms it would contain are energetically highly unfavourable.[2] The *arachno*-$B_{10}H_{14}^{2-}$ ion (**1**, **Figure 6.1**) can be synthesised, however, by reduction of *nido*-$B_{10}H_{14}$ and has been characterised as its tetramethylammonium salt by X-ray diffraction.[3]

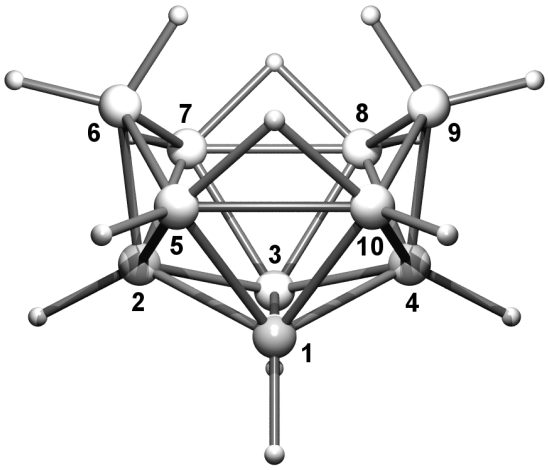

Figure 6.1 – Structure of [*arachno*-$B_{10}H_{14}]^{2-}$, **1**, showing heavy-atom numbering.

According to Gimarc's topological rule,[4] elements more electronegative than boron occupy the sites of highest electron density, which (as determined by natural population analysis, NPA) are at the 6 and 9 positions in $B_{10}H_{14}^{2-}$. A handful of monoheteroatomic anions isolobal with **1** have been prepared and are in agreement with this rule, including [6-$CB_9H_{14}]^-$, [5] [6-$NB_9H_{13}]^-$ [6] and [6-$SB_9H_{12}]^-$.[7] This chapter, however, concerns the structures of the neutral diheteroatomic decaboranes, although

the conclusions drawn from these (**Section 6.5**) may be useful for predicting the gas-phase structures of monoheteroatomic species.

Diheteroatomic decaboranes adopt either C_{2v} or C_s symmetry depending on whether the heteroatoms are the same or different elements. For C_{2v} symmetry the following are known: 6,9-$C_2B_8H_{14}$, [8] **2**, 6,9-$N_2B_8H_{12}$, [9] **3**, and 6,9-$Se_2B_8H_{12}$ [10] and the structures of **2** and **3** are shown in **Figure 6.2**. Two carbaboranes with C_s symmetry have been synthesised, namely 6,9-CNB_8H_{13}, **4**, and 6,9-CSB_8H_{12}, [11] **5**, and are shown in **Figure 6.3**.

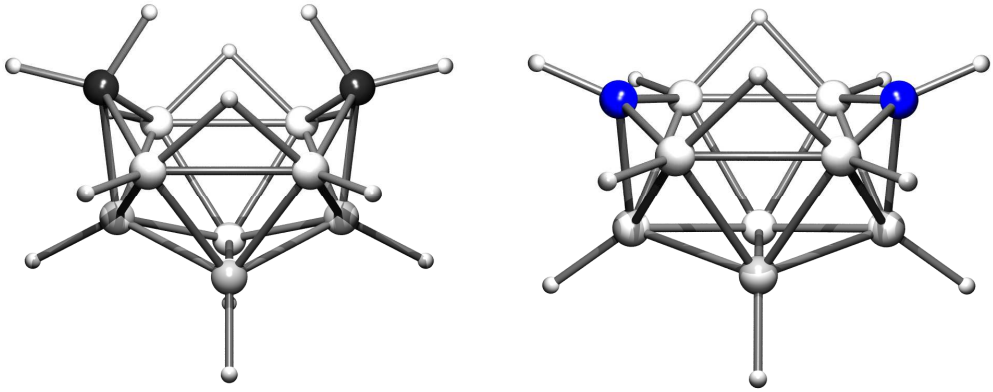

2 **3**

Figure 6.2 – C_{2v} symmetric *arachno*-6,9-$C_2B_8H_{14}$, **2**, and *arachno*-6,9-$N_2B_8H_{12}$, **3**.

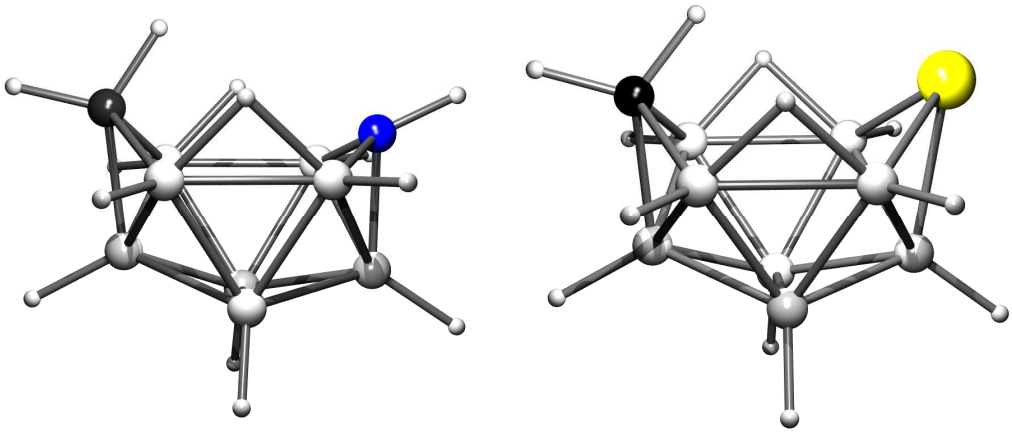

4 **5**

Figure 6.3 – C_s symmetric *arachno*-6,9-CNB_8H_{13}, **4**, and *arachno*-6,9-CSB_8H_{12}, **5**.

This chapter reports the determination of the structures of **2** and **5** by GED and shows that these are close to those predicted by theory. The *ab initio* structures of **1** to **5** have also been calculated and structural trends have been highlighted in **Section 6.4**.

6.2. Computational details

All geometry optimisations were performed using the Gaussian03 program package.[12] The structures were first optimized at the RHF/6-31G(d) level of theory with appropriate symmetry constraints (C_{2v} or C_s). Frequency calculations, carried out at the same level, verified that for each compound a minimum in the potential-energy surface had been found, as they exhibited no imaginary frequencies. Data output by the same frequency calculations were used by the program SHRINK[13] to calculate root-mean-squared amplitudes of vibration (u_{h1}) and perpendicular distance corrections (k_{h1}) for use in the GED refinements. Optimisation at the RMP2(fc)/6-31G(d) level included the effects of electron correlation and in some cases the size of the basis set was increased sequentially from 6-31G(d) to 6-311++G(d,p).[14-16] Wiberg bond indices[17] were calculated using the NBO program,[18] which is incorporated into Gaussian03.

The geometries optimised at the MP2/6-31G(d) level appear to be suitably accurate for these types of systems and exhibit the same trends on substitution as those with larger basis sets. Therefore, to enable easy comparison with similar published structures such as those of *arachno*-5,6,9-$C_3B_7H_{13}$ and -$C_2SB_7H_{11}$,[19] those at the MP2/6-31G(d) level are discussed in **Section 6.4** alongside the GED structures.

6.3. Gas electron diffraction

The GED refinements were performed using the SARACEN method[20] incorporating flexible restraints. Vibrational motion was accounted for using Cartesian force fields obtained from RHF/6-31G(d) calculations, which were converted to a force field

described by a set of symmetry coordinates using the program SHRINK.[13] From these, the root-mean-squared amplitudes of vibration (u_{h1}) and perpendicular distance corrections (k_{h1}) were generated, yielding r_{h1} structures.

6.3.1. Experimental

Samples of **2** and **5** were prepared by Drahomír Hynk according to the literature procedures in references 8 and 11, respectively. Data were collected on Kodak Electron Image film using the Edinburgh GED apparatus,[21] with an accelerating voltage of *ca*. 40 kV (*ca*. 6.0 pm electron wavelength). The precise electron wavelengths were calibrated using benzene and the Edinburgh room temperature nozzle, for which the nozzle-to-film distances are known. Nozzle-to-film distances were calculated for each compound using benzene vapour as a standard, immediately after recording the diffraction pattern for **2** and similarly for **5**. The electron-scattering patterns were converted into digital form using an Epson Expression 1680 Pro flatbed scanner with a scanning program described in reference 22. Data reduction and least-squares refinements were carried out using the ed@ed program,[23] employing the scattering factors of Ross *et al.*[24] The sample and nozzle temperatures, nozzle-to-film distances, scale factors, *s* limits, weighting points, correlation parameters and electron wavelengths for **2** and **5** are shown in **Table 6.1**. The atom numbering scheme used for the molecular models is shown in **Figure 6.4**.

6.3.2. GED model and refinement for *arachno*-6,9-$C_2B_8H_{14}$

A molecular model was written for **2**, converting the refineable independent parameters into atomic Cartesian coordinates. This model was constructed assuming C_{2v} symmetry, allowing the structure to be defined in terms of 18 independent parameters (p_1 to p_{18}, **Table 6.2**). Three of these parameters were used to define the lengths of the bonds, namely B(1)–B(2), B(1)–B(3) and B(1)–B(5). (See **Figure 6.4** for atom numbering.) This was done by taking the average of these three (p_1) and defining two differences: B(1)–B(3) minus B(1)–B(2) (p_2) and B(1)–B(3) minus

B(1)–B(5) (p_3). On the basis of geometry optimisation calculations, all C-H bonds were assumed to be the same length, as were the set of terminal B–H bonds and the remaining group of bridging B–H bonds. The bonds to hydrogen were thus defined in a similar way to the B–B bonds, first taking the average of the three groups (p_8), then defining two differences, B–H_b (bridging) minus C–H (p_9) and B–H_b minus B–H_t (terminal) (p_{10}). For the purposes of this model the *x* axis was defined as that axis lying perpendicular to the B(1)–B(3) bond in the direction of the non-bonded distance C(6)···C(9), the*y* axis forms the axis of rotation and the *z* axis lies along the B(1)–B(3) bond. The origin was defined as being the mid-point between atoms B(1) and B(3). The carbon atoms were placed on the *xy* plane and were positioned using a distance from the origin (p_5) and an angle from the *x* axis (p_6).

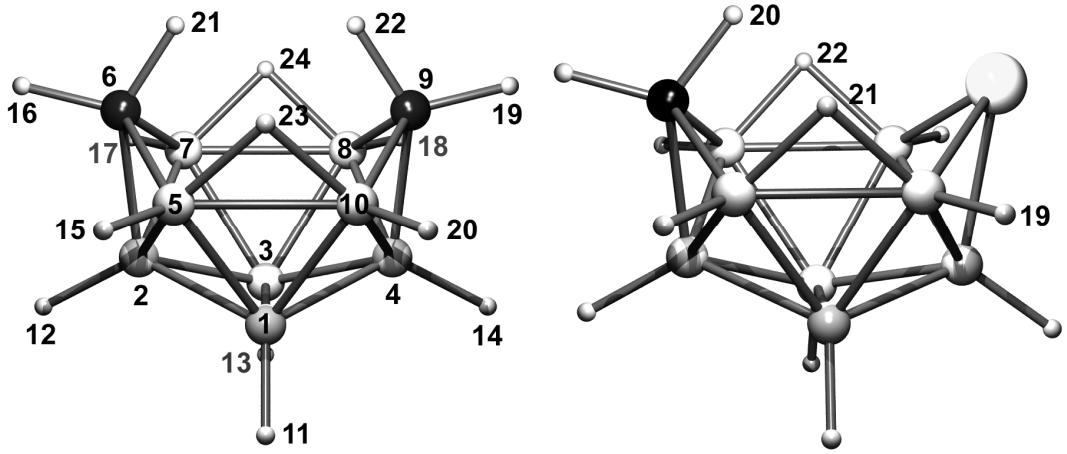

2 **5**

Figure 6.4 – Atom numbering used in the GED models. Where unspecified, atoms in **5** are numbered as in **2**.

Six bond angles were also included as independent parameters, of which B(5)–B(1)–B(3) (p_7) was the only one exclusively involving heavy atoms. The remaining bond angles (p_{11} to p_{15}) were required to position the hydrogen atoms, as shown in **Table 6.2**. Three torsional angles were used, B(4)–B(3)–B(1)–B(5) (p_{16}) being the only one relating only heavy atoms. The torsions B(3)–B(1)–B(5)–H(15) and B(8)–B(5)–B(10)–H(23) (p_{17} and p_{18}) were used to position the hydrogen atoms H(15) and

H(23), respectively. The remaining parameter (p_4) was used to position atoms B(2) and B(4), and was defined as the angle made by B(4), the origin and the *x* axis.

Table 6.1 – GED data analysis parameters for **2** and **5**.[a]

Compound	**2**	**2**	**5**	**5**
Nozzle-to-film distance [b]	96.0	257.1	204.2	262.0
Sample temperature	455	415	410	395
Nozzle temperature	495	460	440	415
R_G	10.3%	4.3%	4.93%	3.01%
R_D	9.4%	2.9%	3.28%	1.38%
Scale factor, *k*	0.579(12)	0.719(6)	0.743(6)	0.794(5)
Correlation parameter	0.453	0.485	0.489	0.486
Δs	4	2	2	1
s_{min}	68	20	50	25
s_{w1}	150	24	80	45
s_{w2}	225	132	180	110
s_{max}	320	154	206	130
Electron wavelength / pm	6.02	6.02	6.13	6.13

[a] Units of *s* are nm^{-1}, nozzle-to-camera distances are in mm, electron wavelengths are in pm and temperatures are in Kelvin. [b] Determined by reference to scattering by benzene.

It was therefore possible to refine all 18 independent parameters, 11 of which were restrained to the MP2/6-31G(d) calculated values, as shown in **Table 6.2**. Four dependent parameters (d_1 to d_4) were also restrained to their MP2/6-31G(d) values during the refinement. These were defined as the differences between the B(5)–C(6) and B(2)–C(6) bonds (d_1), B(2)–B(5) minus B(5)–C(6) (d_2), B(1)–B(2) minus B(5)–C(6) (d_3) and B(5)–B(10) minus B(2)–B(5) (d_4). In addition, seven groups of vibrational amplitudes were refined (Table S2). Two of these groups (amplitudes corresponding to heavy atom distances from 160 to 200 pm and 280 to 320 pm) refined unrestrained, whilst the remaining five groups of amplitudes were each restrained with an uncertainty of *ca.* 10% of its calculated (RHF/6-31G(d)) value.

The final refinement produced an *R* factor (R_G) of 0.057 (R_D = 0.036). The refined molecular-scattering intensity curves and corresponding radial-distribution curve are

shown in **Figures 6.5** and **6.6**, showing good agreement between the model and experimental data. The least-squares correlation matrix and a full list of interatomic distances (r_a), amplitudes of vibration (u_{h1}) and curvilinear perpendicular distance corrections (k_{h1}) are provided in **Appendix 3**.

Table 6.2 – Experimental and theoretical geometric parameters for **2**.[a]

Independent parameters	Description	Value [b]	MP2/6-31G(d) [c]
p_1	*r*B–B average	179.1(2)	178.0
p_2	*r*B(1)–B(3) minus B(1)–B(2)	6.9(4)	7.1(5)
p_3	*r*B(1)–B(3) minus B(1)–B(5)	2.0(5)	1.8(5)
p_4	∠X–O–B(4) [d]	20.2(3)	20.3
p_5	*r*O–C [d]	268.4(6)	267.7
p_6	∠X–O–C(9) [d]	54.4(2)	54.0
p_7	∠B(5)–B(1)–B(3)	107.7(1)	107.3
p_8	*r*B/C–H average	121.0(4)	119.7
p_9	*r*B/C–H diff 1	22.7(5)	22.7(5)
p_{10}	*r*B/C–H diff 2	12.7(4)	12.5(5)
p_{11}	∠B(3)–B(1)–H(11)	120.3(5)	120.3(5)
p_{12}	∠B(4)–B(2)–H(12)	152.7(5)	152.7(5)
p_{13}	∠B(1)–B(5)–H(15)	120.0(5)	120.0(5)
p_{14}	∠B(2)–C(6)–H(16)	109.9(5)	109.8(5)
p_{15}	∠B(2)–C(6)–H(21)	140.5(5)	140.4(5)
p_{16}	ϕB(5)–B(1)–B(3)–B(4)	103.1(4)	102.7
p_{17}	ϕB(3)–B(1)–B(5)–H(15)	144.4(9)	145.6(10)
p_{18}	ϕB(8)–B(10)–B(5)–H(23)	–106.9(5)	–106.5(5)
Dependent parameters			
d_1	*r*B(5)–C minus B(2)–C	8.0(4)	7.7(5)
d_2	*r*B(5)–B(2) minus B(5)–C	3.5(3)	3.2(5)
d_3	*r*B(1)–B(2) minus B(5)–C	0.1(2)	0.2(2)
d_4	*r*B(5)–B(10) minus B(2)–B(5)	9.5(4)	9.6(5)

[a] All distances in pm, angles in °. [b] Numbers in parentheses following experimental values are estimated standard deviations. [c] Where theoretical values are followed by parentheses, the corresponding parameter was restrained to this value in the GED refinement with an uncertainty indicated in brackets. [d] O is the origin and X refers to the positive direction of the *x* axis.

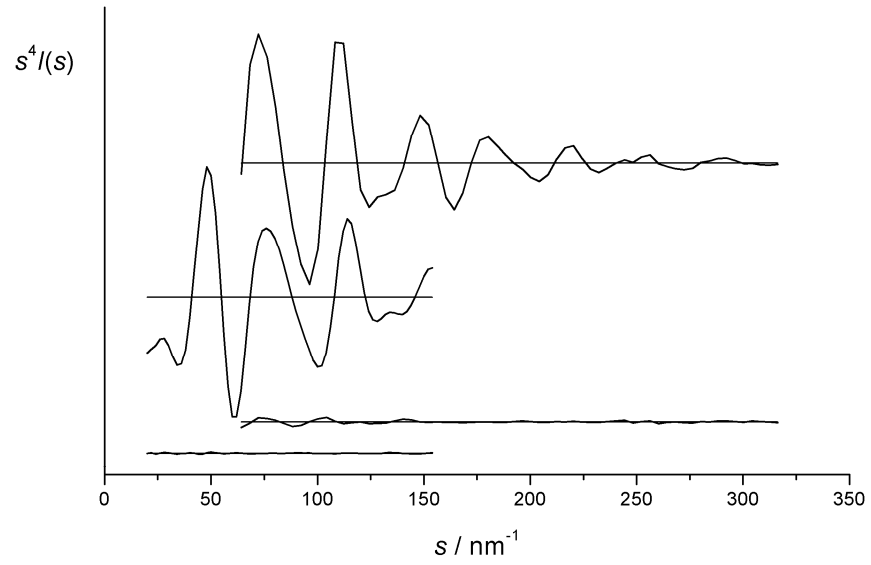

Figure 6.5 – Experimental and weighted difference (experimental – theoretical) molecular scattering intensities for **2**.

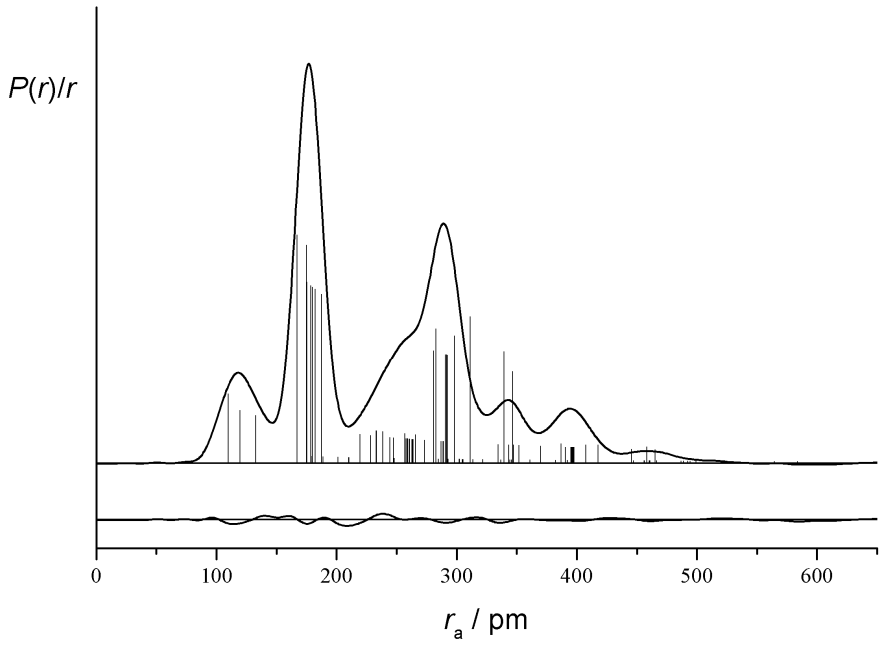

Figure 6.6 – Experimental and difference (experimental – theoretical) radial-distribution curves, $P(r)/r$, for **2**. Before Fourier inversion the data were multiplied by $s.\exp[(-0.00002s^2)/(Z_C - f_C)(Z_B - f_B)]$.

6.3.3. GED model and refinement for *arachno*-6,9-CSB_8H_{12}

The molecular model for **5** was constructed assuming C_s symmetry, allowing the structure to be defined in terms of 30 independent parameters (p_1 to p_{30}, **Table 6.3**). The heavy-atom cage was described using the weighted average of all the B–B, B–C and B–S distances (p_6) and 11 differences (p_7 to p_{17}). The remaining two degrees of freedom in the skeleton were provided by the angle O···B(2)–C(6) (p_{18}) and a fold angle defined as 180˚ minus B(2)···O···B(4) (p_{19}). [In both cases O denotes the origin, defined as the mid-point of B(1) and B(3).] The average of all bonded distances to hydrogen was used in the model (p_1). This, in combination with the difference between the average terminal hydrogen (H_t) and average bridging hydrogen (H_b) distances (p_2), allowed these two distances to be defined. The difference between the two B–H_b distances (p_3) then allowed both of these to refine. On the basis of the *ab initio* calculations only one B–H_t distance was required. This was derived using the difference between B–H_t and the average C–H distance (p_4). The difference between C–H(16) and C–H(20) (p_5) allowed these two bond lengths to be found.

The positions of the hydrogen atoms lying in the plane of symmetry (numbers 12, 14, 16 and 20) were defined using angles made with the heavy atoms (p_{20}, p_{21}, p_{22} and p_{23}, respectively). Similarly, three angles (p_{24}, p_{26} and p_{28}) and three torsional angles (p_{25}, p_{27} and p_{29}) made with the cage were used to define the respective positions of the terminal hydrogen atoms, H(11), H(15) and H(19). Finally, the bridging hydrogen atoms were positioned using the angle B(7)···B(5)–H(21) (p_{30}).

It was possible to refine all 30 independent parameters, 26 of which were restrained to the values calculated at the MP2/6-311++G(d,p) level as shown in **Table 6.3**. Nine groups of amplitudes of vibrations were also refined, all of which were restrained to their RHF/6-31G(d) values. Eight of these groups of amplitudes were restrained with uncertainties of 10% of their values and the remaining group, corresponding to the heavy-atom bonded distances, with an uncertainty of 5%.

Table 6.3 – GED (r_{h1}) and theoretical molecular parameters for **5**.[a]

Independent parameter	Description	GED	MP2/6-311++G(d,p)[b]
p_1	*r*H average	122.3(2)	120.9
p_2	*r*B–H_b average minus B/C–H_t average	15.0(5)	15.3(5)
p_3	*r*B(5)–H(21) minus B(10)–H(21)	4.9(5)	4.9(5)
p_4	*r*B–H_t average minus C–H average	9.9(5)	9.7(5)
p_5	*r*C–H(20) minus C–H(16)	0.4(2)	0.4(2)
p_6	*r*B–B/C/S average	181.7(1)	181.3
p_7	*r*B–B average minus B–C average	9.7(2)	9.4(2)
p_8	*r*B–S average minus B–B average	13.6(3)	13.3(5)
p_9	*r*C–B(5) minus C–B(2)	8.3(4)	8.1(5)
p_{10}	*r*S–B(4) minus S–B(8)	0.2(5)	0.6(5)
p_{11}	*r*B–B difference 1[c]	8.0(1)	7.9(1)
p_{12}	*r*B–B difference 2[d]	2.1(2)	1.9(2)
p_{13}	*r*B–B difference 3[e]	6.3(3)	6.1(3)
p_{14}	*r*B(1)–B(4) minus B(1)–B(2)	1.3(2)	1.3(2)
p_{15}	*r*B(1)–B(10) minus B(2)–B(5)	0.9(2)	0.9(2)
p_{16}	*r*B(1)–B(5) minus B(1)–B(3)	1.6(2)	1.7(2)
p_{17}	*r*B(4)–B(10) minus B(5)–B(10)	5.3(5)	5.3(5)
p_{18}	∠O–B(2)–C[f]	116.4(3)	116.1
p_{19}	∠[180° minus B(2)–O–B(4)][f]	35.1(2)	35.4
p_{20}	∠H(12)–B(2)–C	112.2(5)	112.2(5)
p_{21}	∠H(14)–B(4)–S	116.1(5)	116.1(5)
p_{22}	∠H(16)–C–B(2)	111.9(5)	111.8(5)
p_{23}	∠H(20)–C–B(2)	135.9(5)	136.0(5)
p_{24}	∠H(11)–B(1)–B(3)	120.5(2)	120.5(2)
p_{25}	ϕH(11)–B(1)–B(3)–B(2)	109.0(5)	109.1(5)
p_{26}	∠H(15)–B(5)–B(1)	118.3(2)	118.2(2)
p_{27}	ϕH(15)–B(5)–B(1)–B(2)	107.3(8)	107.5(10)
p_{28}	∠H(19)–B(10)–B(1)	120.8(5)	120.8(5)
p_{29}	ϕH(19)–B(10)–B(1)–B(4)	–104.9(9)	–104.7(10)
p_{30}	∠B(7)···B(5)–H(21)	103.7(8)	103.5(10)

[a] Distances in pm and angles in degrees.

[b] Where theoretical values are followed by parentheses, the independent parameter was restrained to this value in the GED refinement with an uncertainty indicated in brackets.

[c] {[B(1)–B(3)] + 2×[B(1)–B(5)] + 2×[B(5)–B(10)] + 2×[B(4)–B(10)]} / 7 minus {[B(1)–B(2)] + [B(1)–B(4)] + [B(2)–B(5)] + [B(1)–B(10)]} / 4.

[d] {[B(1)–B(2)] + [B(1)–B(4)]} / 2 minus {[B(2)–B(5)] + [B(1)–B(10)]} / 2.

[e] {[B(1)–B(3)] + 2×[B(1)–B(5)]} / 3 minus {[B(5)–B(10)] + [B(4)–B(10)]} / 2.

[f] O is the model origin, defined as the mid-point of B(1)–B(3).

The final refinement produced an R factor (R_G) of 0.037 (R_D = 0.019). The refined molecular-scattering intensity curves and corresponding radial-distribution curve are shown in **Figures 6.7** and **6.8**. The least-squares correlation matrix and a full list of interatomic distances (r_a), amplitudes of vibration (u_{h1}) and curvilinear perpendicular distance corrections (k_{h1}) is provided in **Appendix 4**.

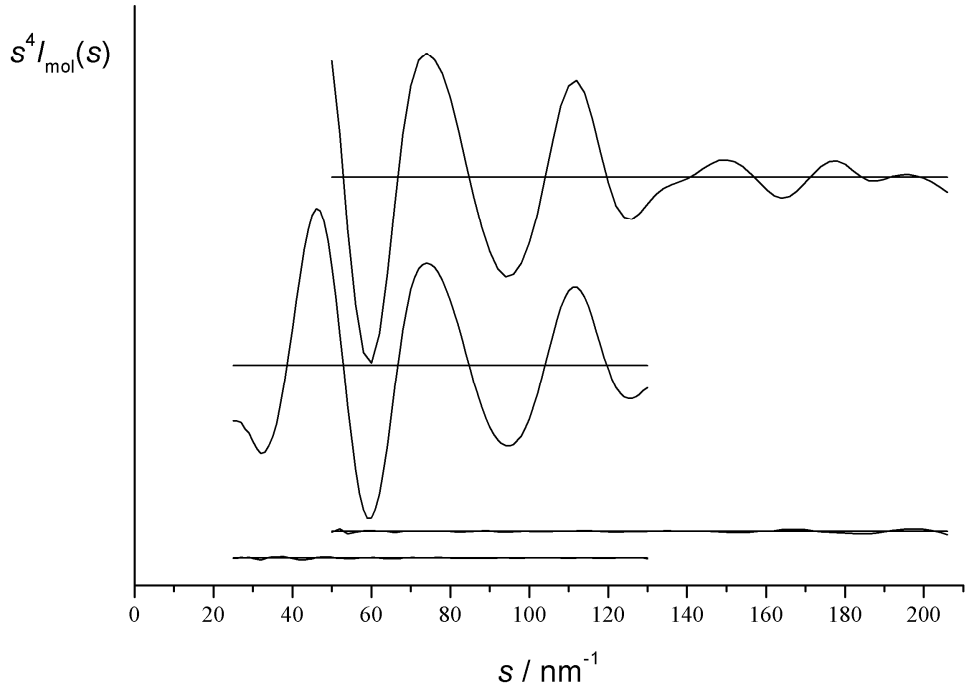

Figure 6.7 – Experimental and weighted difference (experimental – theoretical) molecular-intensity scattering curves for **5**.

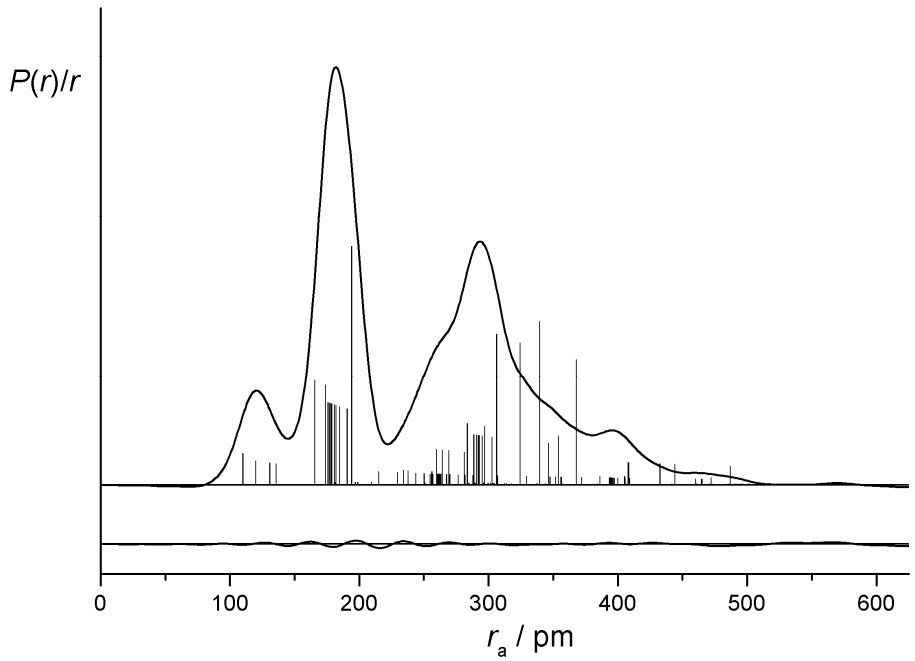

Figure 6.8 – Experimental and difference (experimental minus theoretical) radial-distribution curve, $P(r)/r$, for **5**. Before Fourier inversion the data were multiplied by $s \cdot \exp[(-0.00002s^2)/(Z_S - f_S)(Z_C - f_C)]$.

6.4. Results and discussion

The interesting features of these compounds' molecular structures are the relative bond lengths and the geometries of the six-membered rings in the open faces. The GED and calculated values for the bond lengths in **1** to **5** are shown in **Table 6.4** as are the B–X–B and B–B···B–X angles that characterise the geometry of the open face. **Table 6.4** shows that the bond lengths and angles calculated at the MP2/6-31G(d) are in resonable agreement with those obtained by GED, although in both cases the bond lengths calculated at this level are *ca.* 1-2 pm too short. As GED structures were only obtained for **2** and **5** (and cannot be obtained for **1**) the MP2/6-

31G(d) values are used in the following discussion, where the effect of substituting the $[BH_2]^-$ unit with CH_2, NH and S is highlighted.

From **Table 6.4,** the five B–B distances connecting the four atoms in the base of the molecule (farthest from the substitution site) are relatively unchanged by substitution. The B–B distance in the open face is also effectively unaffected by substitution with carbon, but introduction of either N or S shortens this bond length by *ca*. 3 pm per substitution. The remaining B–B distances (those between atoms adjacent to the substitution site) are the shortest in the parent $[B_{10}H_{14}]^{2-}$ anion and are most affected by substitution. When the nearby substitution is by C they increase by about 2 pm, but replacement by N or S increases these by 11 to 17 pm.

The effect on the substituted bonded distance is approximately in line with that expected on consideration of the relative covalent radii of the substituting atom. The B–C bonds are about 10 to 15 pm shorter than the corresponding B–B bonds, whilst the B–N bonds are 20 to 35 pm shorter. Being a second-row element, sulfur has a covalent radius slightly larger than that of boron and the average B–S distance is lengthened by 9 pm.

A closer inspection of the bond lengths to the heteroatoms reveals another structurally interesting feature of these heteroboranes. In **1** the longest bond is B(5)–B(6) (189.4 pm) and its three symmetrical equivalents. In contrast, the adjacent bond, B(2)–B(6) is one of the shortest (174.9 pm) so that the difference between these two bond lengths is 14.5 pm. Replacement of B(6) with carbon results in a substantial reduction of the difference between these bonds to 7.8, 8.1 and 8.7 pm in **2**, **4** and **5**, respectively. This effect is even more pronounced when the heteroatom is nitrogen or sulfur, for which the respective values of [B(8)–X(9) minus B(4)–X(9)] are –1.6, –3.4 and 0.1 pm in **3**, **4** and **5**, respectively.

Table 6.4 – Selected geometrical parameters for $[B_{10}H_{14}]^{2-}$, **1**, *arachno*-6,9-$C_2B_8H_{13}$, **2**, *arachno*-6,9-$N_2B_8H_{13}$, **3**, *arachno*-6,9-CNB_8H_{13}, **4**, and *arachno*-6,9-CSB_8H_{12}, **5**. (Distances are in pm and angles and torsions are in degrees.)

	***C*$_{2v}$**				***C*$_s$**			
	1 (X,Y=B) MP2/ 6-31G(d)	**2** (X,Y=C) MP2/ 6-31G(d)	GED	**3** (X,Y=N) MP2/ 6-31G(d)	**4** (X=C, Y=N) MP2/ 6-31G(d)	**5** (X=C, Y=S) MP2/ 6-31G(d)	MP2/ 6-311++G(d,p)	GED
r B(1)–B(2)	177.2	174.0	175.2(2)	176.1	174.3	174.4	175.5	175.7(2)
r B(1)–B(4)					175.6	175.7	176.7	177.0(2)
r B(1)–B(3)	180.6	181.0	182.1(3)	180.6	180.3	179.3	180.3	180.7(2)
r B(1)–B(5)	177.1	179.1	180.1(3)	181.6	181.3	180.8	182.0	182.3(2)
r B(1)–B(10)					179.2	177.5	178.5	178.8(2)
r B(2)–B(5)	174.6	176.8	178.5(3)	191.4	177.3	176.4	177.6	178.0(2)
r B(4)–B(10)					186.1	189.2	190.2	190.7(3)
r B(2)–X(6)	174.9	166.0	167.0(5)	155.3	165.6	165.0	166.0	165.9(4)
r B(4)–Y(9)					157.8	193.5	194.4	194.8(4)
r B(5)–X(6)	189.4	173.8	175.1(2)	153.7	173.7	173.7	174.0	174.2(2)
r Y(9)–B(10)					154.4	193.6	193.8	194.6(3)
r B(5)–B(10)	186.6	186.4	188.0(4)	180.0	183.7	183.9	184.9	185.4(3)
∠ B(5)–X(6)–B(7)	101.5	111.9	112.8(4)	120.0	111.4	112.9	113.4	113.2(3)
∠ B(8)–Y(9)–B(10)					122.8	98.7	99.2	98.9(2)
ϕ X(6)–B(5)···B(7)–B(8)	131.1	131.3	129.9(7)	156.7	132.8	129.9	129.6	130.7(6)
ϕ Y(9)–B(10)···B(8)–B(7)					144.6	136.9	136.2	136.8(3)

Inspection of the Wiberg bond indices[16] computed by the NBO program[17] (included in the Gaussian software) provides some insight into these effects. Selected results are displayed in **Table 6.5**. The first thing to be noted is that despite B(5)–B(6) being much longer than the other bonds in the parent compound, **1**, the bond indices are remarkably similar. The origin of this difference is presumably the fewer neighboring atoms. As can be expected, substitution of BH_2^- units significantly disrupts the bond indices in the vicinity of the substitution. With the exception of those to sulfur, all increases in bond index are accompanied by a reduction in bond length. The decrease in the bond length differences [B(5)–X(6) minus B(2)–X(6)] and [B(8)–X(9) minus B(4)–X(9)] on substitution appear to be the result of an increase in the electron density shared in the B(5)–X(6) and B(8)–X(9) bonds, rather than a decrease in B(2)–X(6) and B(4)–X(9) bond strengths. The accompanying decrease in B(2)–B(5) and B(4)–B(10) bond indices (and corresponding increases in bond lengths) suggests that these bonds are the primary source of electron density for the strengthening of the B(5)–X(6) and B(10)–Y(9) bonds in the open face.

Table 6.5 – Selected Wiberg bond indices computed from the MP2/6-31G(d) electron density and corresponding bond lengths.[a]

	C_{2v}						C_s			
	1, $[B_{10}H_{14}]^{2-}$ X = B, Y = B		**2**, $C_2B_8H_{14}$ X = C, Y = C		**3**, $N_2B_8H_{12}$ X = N, Y = N		**4**, CNB_8H_{13} X = C, Y = N		**5**, CSB_8H_{12} X = C, Y = S	
	Index	Length	Index	Length	Index	Length	Index	Length	Index	Length
B(2)–B(5)	0.53	174.6	0.39	176.8	0.23	191.4	0.38	177.3	0.39	176.4
B(4)–B(10)							0.28	186.1	0.36	189.2
B(2)–X(6)	0.54	174.9	0.56	166.0	0.59	155.3	0.57	165.6	0.58	165.0
B(4)–Y(9)							0.56	157.8	0.65	193.5
B(5)–X(6)	0.54	189.4	0.62	173.8	0.68	153.7	0.61	173.7	0.61	173.7
B(10)–Y(9)							0.68	154.4	0.79	193.6

[a] Bond lengths are in pm.

6.5. Conclusions

The structures of two ten-vertex *arachno* carboranes, 6,9-$C_2B_8H_{14}$ and 6,9-CSB_8H_{12} have been determined by GED. These were found to have structures close to those calculated at the MP2/6-31G(d) level of theory, indicating that this level of theory is sufficient for determination of accurate molecular geometries for these types of systems. The theoretical structures of the related compounds: $[B_{10}H_{14}]^{2-}$, 6,9-$N_2B_8H_{14}$ and 6,9-CNB_8H_{12}, were also calculated at the MP2/6-31G(d) level and the theoretical structures of the five compounds were compared. The effects of substitution on the bond lengths are summarised in **Figure 6.9**. This shows that, despite extensive delocalisation of the bonding, the affected bonds were predominantly those in the triangle of bonds nearest the site of substitution - between atoms B(2), B(5) and X(6) and those symmetrically equivalent.

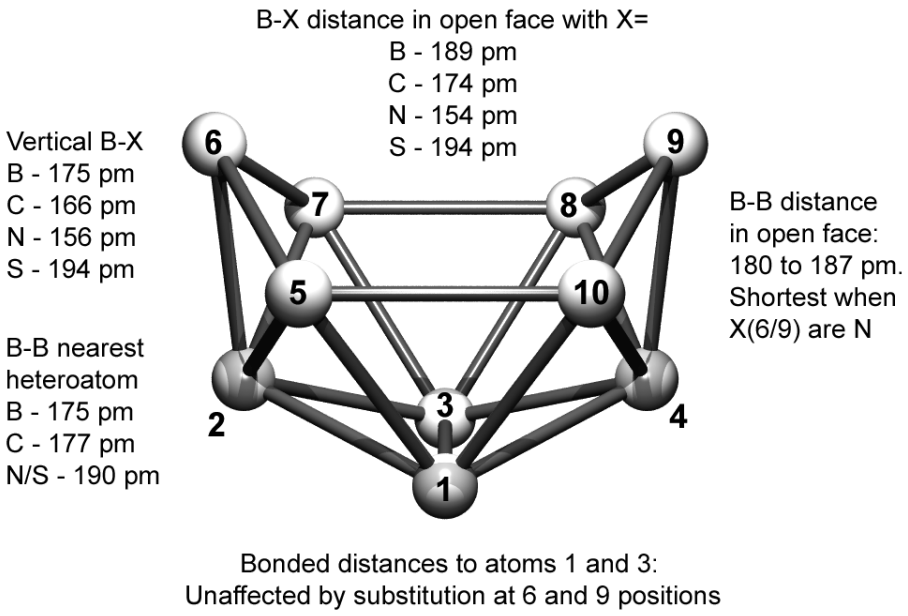

Figure 6.9 – Trends in the bonded distances in the heavy-atom cage for 6,9-substituted *arachno*-decaboranes. The atom labels indicate the heteroatom at the 6 or 9 position closest to the specified bond. Values are average r_e distances calculated at the MP2/6-31G(d) level, which for **2** and **5** were found to be *ca.* 1–2 pm shorter than r_{h1} distances obtained by GED.

6.6. References

1. C. M. Lucht, *J. Am. Chem. Soc.* (1951), **73**, 2373.
2. R. E. Williams, *Adv. Inorg. Chem. Radiochem.* (1976), **18**, 67.
3. D. S. Kendall and W. N. Lipscomb, *Inorg. Chem.* (1973), **12**, 546.
4. J. J. Ott and B. M. Gimarc, *J. Am. Chem. Soc.* (1986), **108**, 4303.
5. X. L. R. Fontaine, J. D. Kennedy, M. Thornton-Pett, K. Nestor, B. Štíbr, T. Jelínek and K. Baše, *J. Chem. Soc., Dalton Trans.* (1990), 2887
6. (a) W. R. Hertler, F. Klanberg and E. L. Muetterties, *Inorg. Chem.* (1967), **6**, 1696. (b) K. Baše, F. Hanousek, B. Štíbr, J. Plešek and J. Lyčka, *J. Chem. Soc., Chem. Commun.*, (1981), 1163. (c) K. Baše, *Collect. Czech. Chem. Commun.* (1983), **48**, 2593.
7. (a) R. W. Rudolph and R. W. Pretzer, *Inorg. Synth.* (1983), **22**, 226. (b) A. R. Siedle, G. M. Bodner, A. R. Garber, D. McDowell and L. J. Todd *Inorg. Chem.* (1977), **13**, 1756. (c) M. Bown, X. L. R. Fontaine and J. D. Kennedy, *J. Chem. Soc., Dalton Trans.* (1988), 1467.
8. B. Štíbr, J. Plešek and S. Heřmánek, *Collect. Czech. Chem. Commun.* (1974), **39**, 1805.
9. B. Štíbr, J. D. Kennedy and T. Jelínek, *J. Chem. Soc., Chem. Commun.* (1990), 1309.
10. G. D. Friesen, A. Barriola and L. J. Todd, *Chem. Ind.* (1978), 631.
11. J. Holub, T. Jelínek, J. Plešek, B. Štíbr, S. Heřmánek and J. Kennedy, *J. Chem. Soc., Chem. Commun.* (1991), 1389.
12. Gaussian 03, Revision B.03, M. J. Frisch, G. W. Trucks, H. B. Schlegel, G. E. Scuseria, M. A. Robb, J. R. Cheeseman, J. A. Montgomery, Jr., T. Vreven, K. N. Kudin, J. C. Burant, J. M. Millam, S. S. Iyengar, J. Tomasi, V. Barone, B. Mennucci, M. Cossi, G. Scalmani, N. Rega, G. A. Petersson, H. Nakatsuji, M. Hada, M. Ehara, K. Toyota, R. Fukuda, J. Hasegawa, M. Ishida, T. Nakajima, Y. Honda, O. Kitao, H. Nakai, M. Klene, X. Li, J. E. Knox, H. P. Hratchian, J. B. Cross, C. Adamo, J. Jaramillo, R. Gomperts, R. E. Stratmann, O. Yazyev, A. J. Austin, R. Cammi, C. Pomelli, J. W. Ochterski, P. Y. Ayala, K. Morokuma, G. A. Voth, P. Salvador, J. J. Dannenberg, V. G. Zakrzewski, S. Dapprich, A. D. Daniels, M. C. Strain, O. Farkas, D. K. Malick, A. D. Rabuck, K. Raghavachari, J. B. Foresman, J. V. Ortiz, Q. Cui, A. G. Baboul, S. Clifford, J. Cioslowski, B. B. Stefanov, G. Liu, A. Liashenko, P. Piskorz, I. Komaromi, R. L. Martin, D. J. Fox, T. Keith, M. A. Al-Laham, C. Y. Peng, A. Nanayakkara, M. Challacombe, P. M. W. Gill, B. Johnson, W. Chen, M. W. Wong, C. Gonzalez and J. A. Pople, Gaussian, Inc., Wallingford CT, (2003).
13. (a) V. A. Sipachev, *J. Mol. Struct.* (*THEOCHEM*) (1985), **121**, 143.
14. R. Ditchfield, W. J. Hehre and J. A. Pople, *J. Chem. Phys.* (1971), **54**, 724.

15. P. C. Hariharan and J. A. Pople, *Theo. Chim. Acta.* (1973), **28**, 213.

16. A. D. McLean and G. S. Chandler, *J. Chem. Phys.* (1980), **72**, 5639.

17. K. Wiberg, *Tetrahedron* (1968), **24**, 1083.

18. E. D. Glendening, A. E. Reed, J. E. Carpenter and F. Weinhold, *NBO Version 3.1*.

19. D. Hynk and J. Holub, *Collect. Czech. Chem. Commun.* (2002), **67**, 813.

20. (a) A. J. Blake, P. T. Brain, H. McNab, J. Miller, C. A. Morrison, S. Parsons, D. W. H. Rankin, H. E. Robertson and B. A. Smart, *J. Phys. Chem.* (1996), **100**, 12280. (b) N. W. Mitzel and D. W. H. Rankin, *J. Chem. Soc., Dalton Trans.* (2003), 3650.

21. C. M. Huntley, G. S. Laurenson and D. W. H. Rankin, *J. Chem. Soc., Dalton Trans.* (1980), 954.

22. H. Fleischer, D. A. Wann, S. L. Hinchley, K. B. Borisenko, J. R. Lewis, R. J. Mawhorter, H. E. Robertson and D. W. H. Rankin, *Dalton Trans.* (2005), 3221.

23. S. L. Hinchley, H. E. Robertson, K. B. Borisenko, A. R. Turner, B. F. Johnston, D. W. H. Rankin, M. Ahmadian, J. N. Jones and A. H. Cowley, *Dalton Trans.* (2004), 2469.

24. A. W. Ross, M. Fink and R. Hilderbrandt, *International Tables for Crystallography*, (Ed.: Wilson, A. J. C. Kluwer Academic Publishers, Dordrecht, Boston, and London, Vol. C, p. 245, (1992).

Chapter 7

Molecular structures of $CF_3SO_2OCF_3$ and $CH_3SO_2SCH_3$ by GED and *ab initio* calculations – the effect of basis set on theoretical sulfonate and thiosulfonate structures.

7.1. Introduction

A small number of compounds with the structure XSO_2–OY have previously been studied by GED: FSO_2–OCH_3,[1] $ClSO_2$–OCH_3,[2] FSO_2–OF and FSO_2–OCl,[3] CF_3SO_2–OCH_3,[4] $ClSO_2$–OCF_3,[5] FSO_2–OSF_5,[6] CF_3SO_2–OC(O)F[7] and CF_3SO_2–OC(O)Cl.[8] Perhaps the most interesting feature of these structures is the variability of the length of the S–O single bond. Those obtained for the compounds above are shown in **Table 7.1** and in the cases where the authors presented calculated values, the result from the highest level calculation is also shown.

Table 7.1 – S–O single bond distances obtained by GED and in some cases by theoretical calculations.[1-8]

X	Y	S–O (GED) [a]	Type	S–O (calc)	Method
F	CH_3	155.8(7)	r_a	–	–
Cl	CH_3	156.2(4)	r_a	–	–
F	F	160.6(3)	r_a	160.8	HF/6-31G(d)
F	Cl	158.9(3)	r_a	158.4	HF/6-31G(d)
CF_3	CH_3	155.5(1)	r_a	162.2	B3LYP/6-31G(d)
Cl	CF_3	160.6(2)	r_{h1}	162.8	B3LYP/6-311+(3df)
F	SF_5	159.9(3)	r_{h1}	165.2	MP2/6-31G(d)
CF_3	FCO	163.2(2)	r_a	169.4	MP2/6-311G(d)
CF_3	ClCO	162.6(2)	r_g	165.8	MP2/6-311+G(2df)

[a] Uncertainties for the first two compounds are estimated total uncertainties, whilst those for the remaining compounds are standard deviations.

From **Table 7.1** it appears that the presence of an electron-withdrawing group at the Y position weakens the S–O bond. Also of interest is that the correlated theoretical methods, B3LYP and MP2 appear to overestimate this distance whereas HF values are much closer to the GED ones.

The freedom to rotate around the S–O bond also poses the question of which conformers are present and the possible conformations are presented in **Figure 7.1**. None of the GED analyses of these compounds yielded much information regarding the preferred conformation and in most cases a single conformer was assumed approximately midway between the *gauche* and *anticlinal* structures. However, in the analysis of $ClSO_2–OCH_3$ the structure refined with 11(8)% *trans* form. In most of these studies theoretical calculations were also performed for the torsional potential around the S–O bond. In all cases the *gauche* conformer was found to be the most stable although some calculations predicted a second stable *trans* conformer a few kJ mol^{-1} higher in energy.

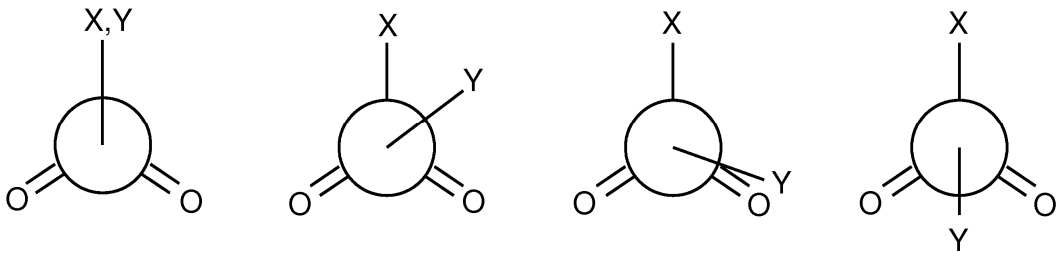

syn-periplanar (*cis*) synclinal (*gauche*) anticlinal (*anti*) anti-periplanar (*trans*)

Figure 7.1 – Newman projections of possible conformations of covalent sulfonates with the structure $XSO_2–OY$.

This chapter presents the GED structures of the sulfonate, $CF_3SO_2OCF_3$, and the thiosulfonate, $CH_3SO_2SCH_3$, shown in **Figures 7.2** and **7.3**, respectively. In both cases the electron-diffraction investigation was supplemented by theoretical calculations and the difficulty in predicting the S–O bond length has been shown to be primarily due to insufficient polarisation of the basis set on sulfur.

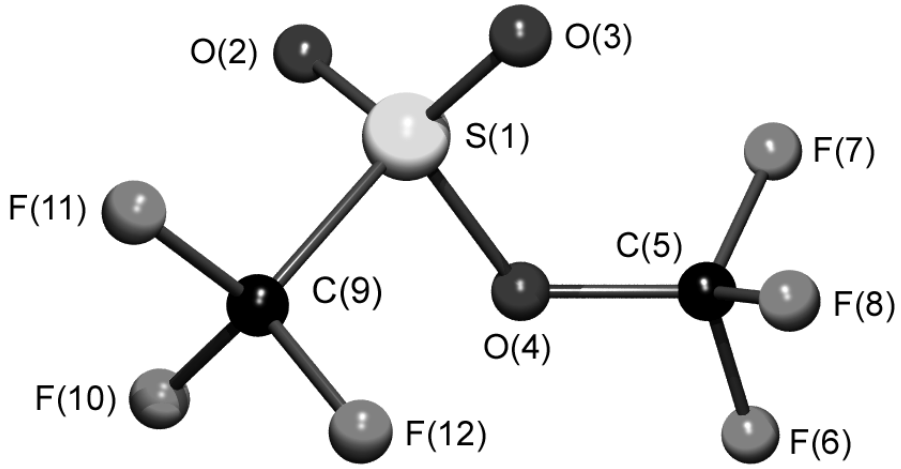

Figure 7.2 – Molecular structure of $CF_3SO_2OCF_3$ showing the atom numbering used in the GED model.

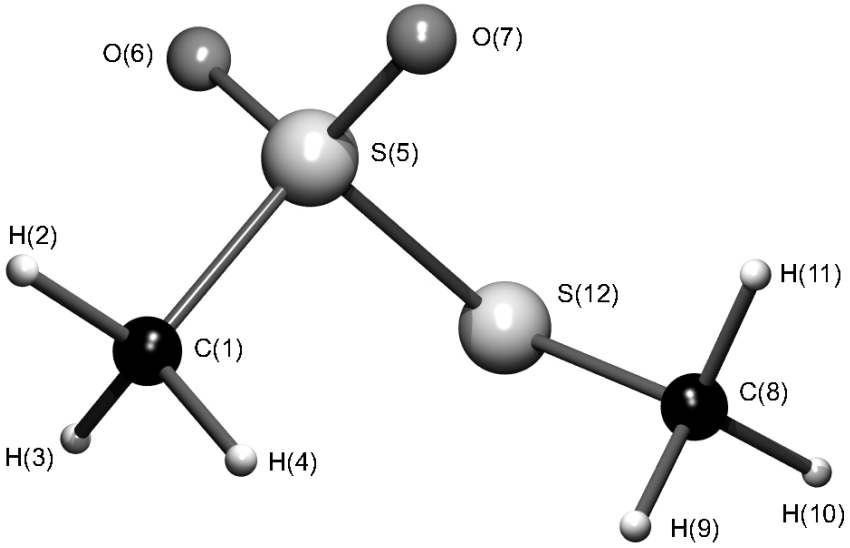

Figure 7.3 – Molecular structure of $CH_3SO_2SCH_3$ showing the atom numbering used in the GED model.

7.2. Theoretical calculations

All calculations were performed using the Gaussian03 program package,[9] with standard gradient techniques and default convergence criteria.

7.2.1. Geometry optimisations

Starting geometries were obtained using the RHF approximation with a 3-21G(d) basis set,[10,11] followed by a 6-31G(d) basis set.[12–14] Frequency calculations, carried out at the same levels, verified that minima in the potential-energy surface had been found, as they exhibited no imaginary frequencies. Electron correlation was then considered using the frozen-core MP2[15] approach with the 6-31G(d) basis set. For $CF_3SO_2OCF_3$ the effect of basis set on each theoretical structure was assessed by increasing the basis set size to approximate the valence electrons better [6-311G(d)][16] and include diffuse functions [6-311+G(d)][17] or to include additional polarisation functions [6-31G(3df)].[18] In the case of $CH_3SO_2SCH_3$ these were combined 6-311G(3df) and polarisation functions were included on hydrogen as well [6-311G(3df,3pd)].[18] In order to gauge the effect of the type of theory, hybrid-DFT calculations were performed using Becke's three-parameter hybrid exchange functional[19] (B3) combined with both the Lee-Yang-Parr gradient-corrected correlation functional (LYP)[20] and the same basis sets as for the MP2 calculations.

7.2.2. Potential energy scans

Potential-energy scans were performed in 5° steps. For $CF_3SO_2OCF_3$ the HF and MP2 approximations were used with the 6-31G(d) basis set and for $CH_3SO_2SCH_3$ B3LYP functional was also used. In addition, MP2 scans were performed for both compounds using a mixture of basis sets, with a 6-31G(3df) basis set on the sulfur atoms and the 6-31G(d) basis set on the remaining atoms.

7.2.3. Vibrational amplitudes and distance corrections for GED

Cartesian force fields were generated for $CF_3SO_2OCF_3$ and $CH_3SO_2SCH_3$ at the HF/6-31G(d) and MP2/6-31G(d) levels, respectively. These were converted into force fields described by a set of symmetry coordinates using the program SHRINK,[21] which generated starting values for the root-mean-squared amplitudes of vibration (u) and perpendicular distance corrections (k_{h1}).

7.3. Gas electron diffraction

The GED refinements were performed using the SARACEN method[22] incorporating flexible restraints. As curvilinear perpendicular distance corrections (k_{h1}) were applied during the refinement, the resulting structures were of the r_{h1} type.

7.3.1. Experimental

Samples of $CF_3SO_2OCF_3$ and $CH_3SO_2SCH_3$ were provided by Aida Ben Altabef from the Universidad Nacional de Tucumán in Argentina. Data were collected on Kodak Electron Image film using the Edinburgh GED apparatus,[23] with an accelerating voltage of *ca*. 40 kV. Nozzle-to-film distances were calculated for each compound using benzene vapour as a standard, immediately after recording the diffraction pattern for each compound. The electron-scattering patterns were converted into digital form using an Epson Expression 1680 Pro flatbed scanner with a scanning program described in reference 22. Data reduction and least-squares refinements were carried out using the ed@ed program,[25] employing the scattering factors of Ross *et al*.[26] The sample and nozzle temperatures, nozzle-to-film distances, scale factors, *s* limits, weighting points, correlation parameters and electron wavelengths are shown in **Table 7.2**. The atom numbering schemes used for the molecular models are shown in **Figures 7.2** and **7.3**.

Table 7.2 – GED data analysis parameters.[a]

Compound	$CF_3SO_2OCF_3$		$CH_3SO_2SCH_3$	
Dataset type	short	long	short	long
Nozzle-to-film distance [b]	130.5	291.5	95.6	259.1
Sample temperature	195	195	405	350
Nozzle temperature	298	298	418	375
R_G	0.070	0.061	0.083	0.077
R_D	0.043	0.025	0.060	0.040
Scale factor, k	0.691(16)	0.704(8)	0.883(12)	0.818(5)
Correlation parameter	0.471	0.496	0.315	0.457
Δs	2	1	2	1
s_{min}	90	35	86	20
s_{w1}	110	50	120	40
s_{w2}	250	110	330	130
s_{max}	270	120	380	148
Electron wavelength (pm)	6.13	6.13	6.18	6.18

[a] Units of s are nm^{-1}, nozzle-to-camera distances are in mm, electron wavelengths are in pm and temperatures are in Kelvin. [b] Determined by reference to scattering by benzene.

7.3.2. GED model and refinement for $CF_3SO_2OCF_3$

The molecular model for the GED refinement assumed overall C_1 symmetry, as predicted by the calculations. The structure of $CF_3SO_2OCF_3$ was defined in terms of 25 independent parameters, comprising 11 bond lengths and differences, 10 bond angles and differences, one tilt angle and three torsional angles, listed in Table 2. The bonded distances S–O(4), O(4)–C(5) and S–C(9), were each defined individually (p_7, p_{10} and p_{11}, respectively), whilst simple averages were taken of the six C–F bond lengths (p_1) and of the two S=O bond lengths (p_8). The difference between the average C–F distances in the CF_3 groups bonded to O(4) (group 1) and sulfur (group 2) was defined (p_2). In group 1, C–F(6) was then found by defining the difference between this and the average of C–F(7) and C–F(8) (p_3). The difference between these remaining bond lengths was then defined (p_5). Similarly, in group 2 the differences between C–F(11) and an average of the other two bonds (p_4) and C–F(12) minus C–F(10) (p_6) were defined. The difference between the two S=O double bonds (p_9) allowed these bond lengths to be defined.

The geometry around sulfur was described using three angles and two differences: the O(4)–S–C(9) angle (p_{12}), the average of O(2)–S–O(4) and O(3)–S–O(4) (p_{13}) and their difference (p_{14}), and the average of O(2)–S–C(9) and O(3)–S–C(9) (p_{15}) and their difference (p_{16}).

Fluorine-atom positions in CF_3 group 1 were described using the average of the three internal F–C–F angles (p_{19}), with the difference between F(7)–C–F(8) and the angles F(6)–C–F(7) and F(6)–C–F(8) (p_{20}), the latter two angles being assumed to be identical. The orientation of this CF_3 group with respect to sulfur was defined using the angles S–O–C (p_{17}) and O–C–F(6) (p_{18}), and the torsional angles C–S–O–C (p_{23}) and S–O–C–F(6) (p_{24}).

CF_3 group 2 was described using a single F–C–F angle (p_{22}), and orientated using a tilt angle (p_{21}). A positive tilt was defined as a reduction in the S–C–F(11) angle, with the zero point occurring when the three S–C–F angles are equal. This group was also allowed to rotate around the S–C bond, defined by the torsional angle O(4)–S–C–F(11) (p_{25}). In this case an angle of 180˚ corresponds to a staggered conformation and a larger angle moves F(11) closer to O(3).

All 25 independent parameters were refined, along with two individual (S–O and S–C) and eight groups of amplitudes of vibration, producing an R_G factor of 0.067 (R_D = 0.029). The refined parameters are displayed in **Table 7.3** along with the corresponding values predicted by MP2/6-31G(3df) calculations. The molecular-scattering intensity curves are shown in **Figure 7.4** and the radial-distribution curve is shown in **Figure 7.5**. Restraints on geometrical parameters were derived from the MP2/6-31G(3df) calculated values and those applied directly to independent or dependent parameters are listed in **Table 7.3**, whilst those applied to differences between independent parameters are shown in **Table 7.4**. A full list of interatomic distances and corresponding amplitudes of vibration is given in **Appendix 5**.

Table 7.3 – GED refined parameters for $CF_3SO_2OCF_3$, corresponding theoretical values and flexible restraints used (distances in pm and angles in degrees).[a]

	Description	Value	MP2/6-31G(3df)
	Independent parameters		
p_1	*r* C–F average	133.3(2)	131.9
p_2	*r* C–F difference 1	–0.4(1)	–0.4(1)
p_3	*r* C–F difference 2	0.4(1)	0.4(1)
p_4	*r* C–F difference 3	0.2(1)	0.2(1)
p_5	*r* C–F difference 4	0.2(1)	0.2(1)
p_6	*r* C–F difference 5	0.0(1)	0.0(1)
p_7	*r* S–O	161.5(4)	162.2
p_8	*r* S=O average	141.9(3)	141.9
p_9	*r* S=O difference	0.4(1)	0.4(1)
p_{10}	*r* C–O	139.3(7)	139.0
p_{11}	*r* C–S	181.3(4)	183.8
p_{12}	∠ O(4)–S–C	96.9(10)	97.0(10)
p_{13}	∠ O–S–O(4) average	108.0(2)	108.0
p_{14}	∠ O–S–O(4) difference	3.8(4)	4.4(5)
p_{15}	∠ C–S–O average	107.9(3)	107.6
p_{16}	∠ C–S–O difference	1.3(2)	1.3(2)
p_{17}	∠ S–O–C	121.8(4)	121.3(5)
p_{18}	∠ O–C–F(6)	104.6(4)	105.8
p_{19}	∠ F–C–F group 1 average	108.0(2)	109.3
p_{20}	∠ F–C–F group 1 difference	0.3(2)	0.4(2)
p_{21}	∠ S–C–F tilt	1.6(5)	1.6(5)
p_{22}	∠ F–C–F group 2	108.6(2)	109.8
p_{23}	ϕ C–S–O–C	119.5(18)	105.6
p_{24}	ϕ S–O–C–F(6)	195.2(9)	182.6
p_{25}	ϕ O–S–C–F(11)	177.2(10)	178.5(20)
	Dependent parameter		
d_1	∠ O(2)=S=O(3)	124.6(8)	125.1(10)

[a] Where calculated values are followed by a number in parentheses, a restraint was applied to the corresponding parameter using the calculated value. The numbers in parentheses are the uncertainties of the restraints.

Table 7.4 – Restraints on differences between independent parameters in the GED refinement (distances in pm and angles in degrees).[a]

Difference		GED	MP2/6-31G(3df)
$p_{10} - p_1$	r [C–O] – [C–F av]	6.1(8)	7.0(10)
$p_{13} - p_{15}$	∠ [O–S–O(4) av] – [C–S–O av]	0.1(2)	0.3(2)
$p_{22} - p_{19}$	∠ [F–C–F gp 2] – [F–C–F gp 1 av]	0.5(2)	0.5(2)
$p_{19} - p_{18}$	∠ [F–C–F gp 1 av] – [O–C–F(6)]	3.5(5)	3.5(5)

[a] Where calculated values are followed by a number in parentheses, a restraint was applied to the corresponding parameter using the calculated value. The numbers in parentheses are the uncertainties of the restraints.

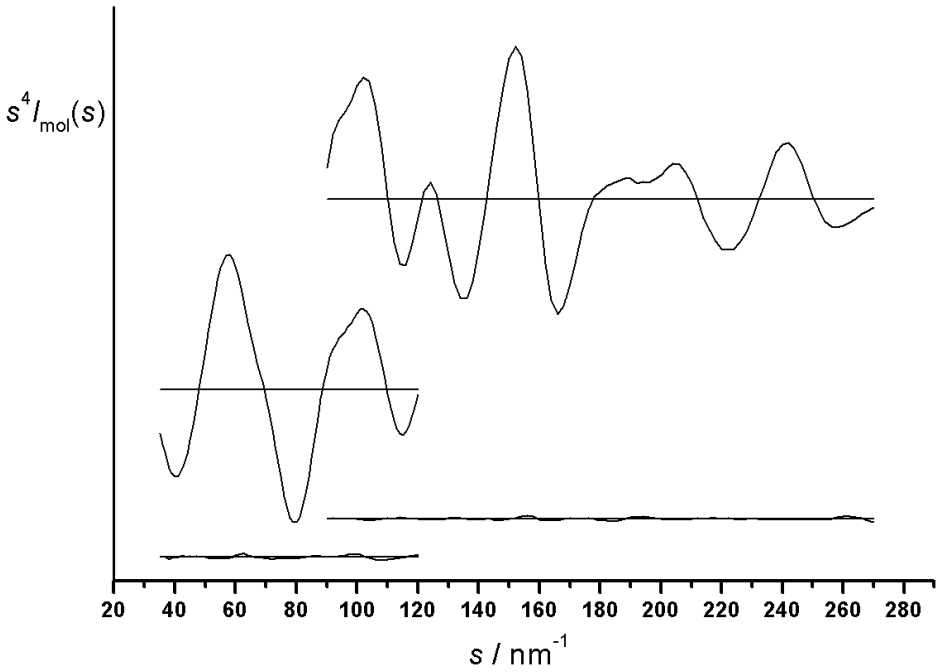

Figure 7.4 – Molecular scattering intensities for $CF_3SO_2OCF_3$.

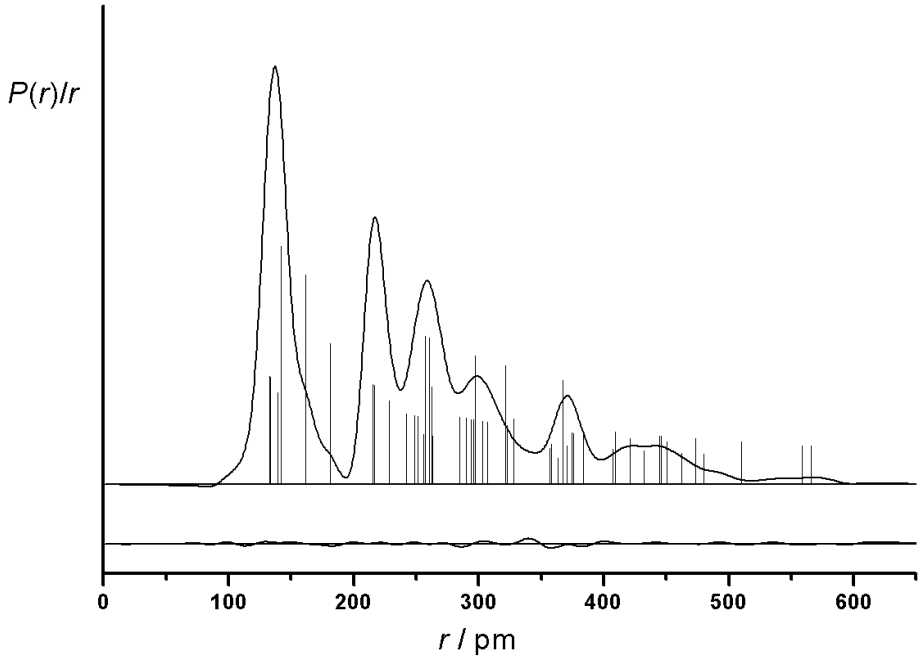

Figure 7.5 – Experimental and difference (experimental minus theoretical) weighted radial-distribution function for $CF_3SO_2OCF_3$. Molecular scattering intensities were multiplied by $s\times\exp[(-0.00002s^2)/(Z_S - f_S)(Z_F - f_F)]$ prior to Fourier inversion.

7.3.3. GED model and refinement for $CH_3SO_2SCH_3$

The molecular model for the GED refinement of $CH_3SO_2SCH_3$ was assigned overall C_1 symmetry as predicted by the *ab initio* calculations. (The atom numbering used in the model and calculations is shown in **Figure 7.3**.) The structure was defined in terms of 19 independent parameters, comprising six bond lengths and differences, eight bond angles and differences, two tilt angles and three torsional angles.

The bonded S–S distance was defined individually (p_2) and, on the basis of the *ab initio* calculations and the low scattering ability of hydrogen, the six C–H bonds were assumed to be of equal length (p_1). The S=O bond lengths were defined in terms of the average (p_5) and difference [S=O(7) minus S=O(6), p_6], as were the two C–S

bonds. [parameter p_3 is the average and p_4 is defined as C(8)–S(12) minus C(1)–S(5).]

The geometry of the sulfonyl group in relation to C(1) and S(12) was described using the S–S–C(1) angle (p_7), the average of the two S–S=O angles (p_8) in combination with their difference [S–S=O(7) minus S–S=O(6), p_9], and the average of the two C–S=O angles (p_{10}) combined with their difference [C–S=O(6) minus C–S=O(7), p_{11}].

Local C_3 symmetry was assumed for both methyl groups. Separate internal H–C–H angles were used for each methyl group. These were defined in terms of the average H-C–H angle (p_{13}) and the difference (p_{14}) between the averages for the two groups [H–C(1)–H minus H–C(8)–H]. The methyl group containing C(1) was oriented with respect to the rest of the molecule using a tilt angle (p_{15}, defined as the angle between the local C_3 axis and the C–S bond with a reduction in the S–C–H(2) angle being positive) and the S–S–C–H(2) torsion (p_{18}). The positioning of C(8) was performed using a second S–S–C angle (p_{12}) and the C–S–S–C torsion (p_{17}). Finally, hydrogen atoms 9 to 11 were positioned using a second tilt angle (p_{16}, defined as above with a reduction of the S–C–H(10) angle being positive) and the S–S–C–H(10) angle (p_{19}). As an internal H–C–H angle was used for each methyl group, these angles were unaffected by application of the torsion or tilt angles.

A second GED refinement was performed using a two-conformer model. However, the radial-distribution functions for the two conformers are so similar that the C_1 conformer alone fitted the data as well as any mixture of conformers. Therefore, only the single-conformer (C_1) refinement is presented.

All 19 independent parameters were refined, along with one individual and seven groups of amplitudes of vibration, producing an R_G factor of 0.081 (R_D = 0.048). The refined parameters are displayed in **Table 7.5** along with the corresponding values

predicted by MP2/6-311G(3df,3pd) calculations. The molecular-intensity and radial-distribution curves are shown in **Figures 7.6** and **7.7**, respectively.

Table 7.5 – GED-refined parameters for $CH_3SO_2SCH_3$ (distances in pm, angles in °)

Independent parameter	Description	GED value	MP2/6-311G(3df,3pd)[a]
p_1	*r* C-H	108.86(34)	108.63
p_2	*r* S-S	207.47(9)	206.92
p_3	*r* C-S mean	180.33(10)	178.45
p_4	*r* C(8)–S(12) minus C(1)–S(5)	3.74(47)	3.86(50)
p_5	*r* SO mean	143.45(4)	143.59
p_6	*r* S–O(7) minus S–O(6)	0.34(19)	0.31(20)
p_7	∠ S–S–C(1)	102.8(6)	104.1
p_8	∠ S–S–O mean	106.8(2)	107.0
p_9	∠ S–S–O(7) minus S–S–O(6)	5.8(3)	3.8(10)
p_{10}	∠ C–S–O mean	109.0(2)	107.7
p_{11}	∠ C–S–O(6) minus C–S–O(7)	0.8(5)	0.8(5)
p_{12}	∠ S–S–C(8)	100.3(6)	98.9
p_{13}	∠ H–C–H mean	109.1(5)	110.5(10)
p_{14}	∠ H–C(1)–H minus H–C(8)–H	0.9(5)	1.1(5)
p_{15}	∠ Me C(1) tilt	1.5(9)	1.6(10)
p_{16}	∠ Me C(8) tilt	1.9(9)	2.5(10)
p_{17}	ϕ C–S–S–C	80.1(25)	81.2
p_{18}	ϕ S–S–C–H(2)	179.6(19)	179.7(20)
p_{19}	ϕ S–S–C–H(10)	190.3(43)	191.1(50)
Dependent parameter			
d_1	∠ O–S–O	121.0(2)	121.9(4)
d_2	∠ S–S–C(1) minus S–S–C(8)	2.5(11)	5.2(20)
d_3	∠ C–S–O minus S–S–O ($p_{10} - p_8$)	2.1(3)	0.7(10)

[a] Where calculated values are followed by a number in parentheses, a restraint was applied to the corresponding parameter using the calculated value. The numbers in parentheses are the uncertainties of the restraints.

Restraints on geometrical parameters were derived from the MP2/6-311G(3df,3pd) calculated values. Those applied directly to independent or dependent parameters are listed in **Table 7.5**. The least-squares correlation matrix and a full list of interatomic distances and corresponding amplitudes of vibration is given in **Appendix 6**. The amplitude of vibration for the S–S bond was refined individually as this was the only distance comprising heavy atoms contributing to the corresponding peak in the radial-distribution curve (**Figure 7.7**). Seven groups of amplitudes, corresponding to the remaining peaks in the radial-distribution curve, were also refined. Those amplitudes corresponding to non-bonded distances were restrained with uncertainties of 10% of their calculated values, as were the amplitudes for the bonded C–S distances, which were tied to one another.

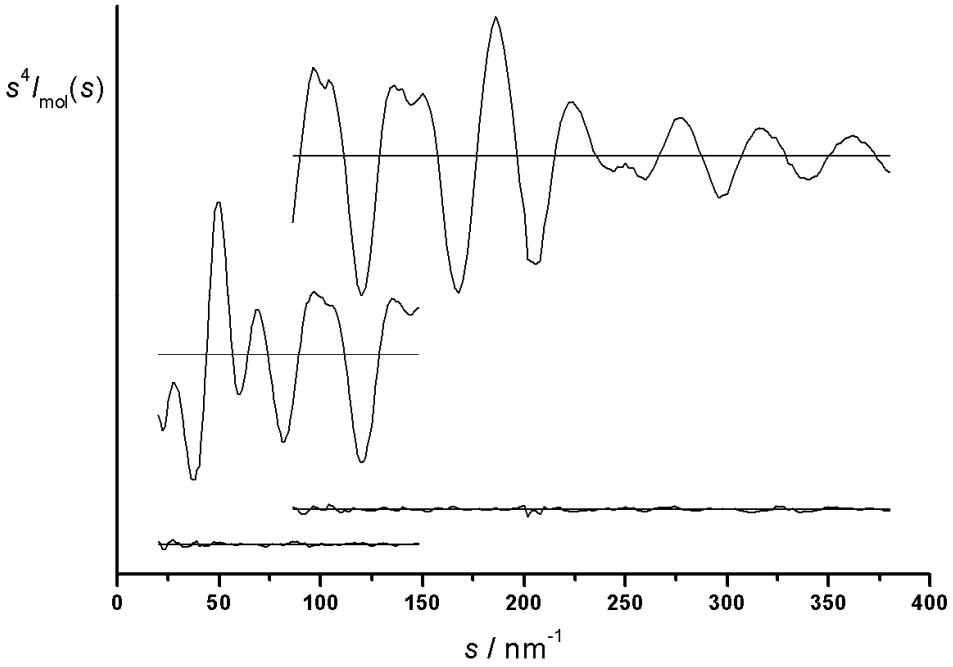

Figure 7.6 – Molecular scattering intensities for $CH_3SO_2SCH_3$.

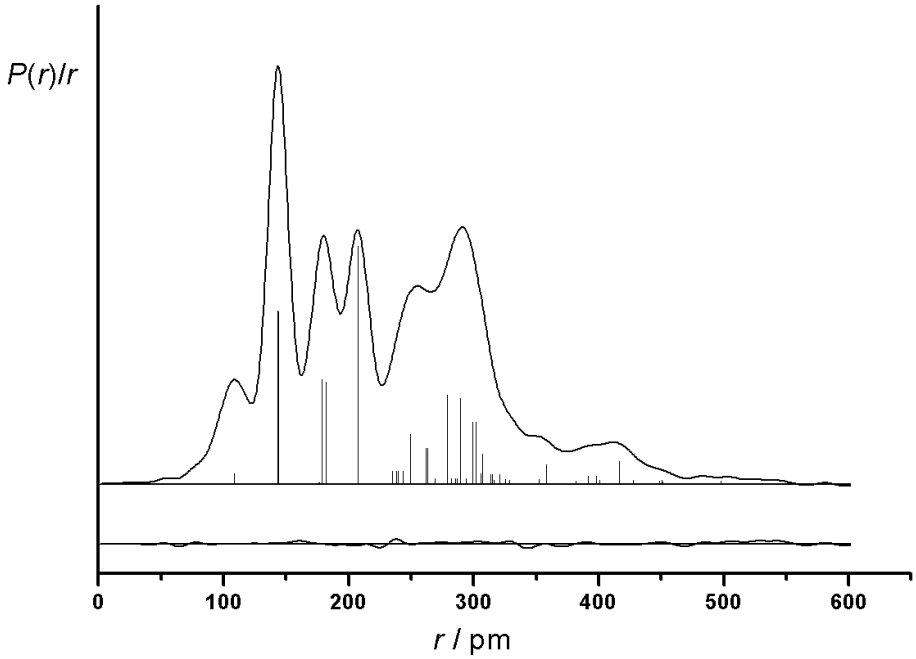

Figure 7.7 – Experimental and difference (experimental minus theoretical) weighted radial-distribution function for $CH_3SO_2SCH_3$. Molecular scattering intensities were multiplied by $s\times\exp[(-0.00002s^2)/(Z_S - f_S)^2]$ prior to Fourier inversion.

7.4. Results and discussion

7.4.1. $CF_3SO_2OCF_3$

Potential-energy scans for $CF_3SO_2OCF_3$ are shown in **Figure 7.8**. For all three calculation types, only one conformer was found, with a C–S–O–C dihedral angle of about 110°. Therefore, only this conformer was used in the GED refinement and investigated further by *ab initio* calculations.

The C–S–O–C torsional angle was found to be 119.5(18)˚ by GED compared to *ca.* 105 to 112˚ by various theoretical methods, shown in **Table 7.6**. However, considering the flatness of the potential-energy curve this discrepancy does not

represent a significant energy penalty. In addition, the estimated standard deviation of this value does not give a good estimate of its uncertainty, as the refinement can be performed by fixing this angle at any arbitrary value between 100 and 150˚.

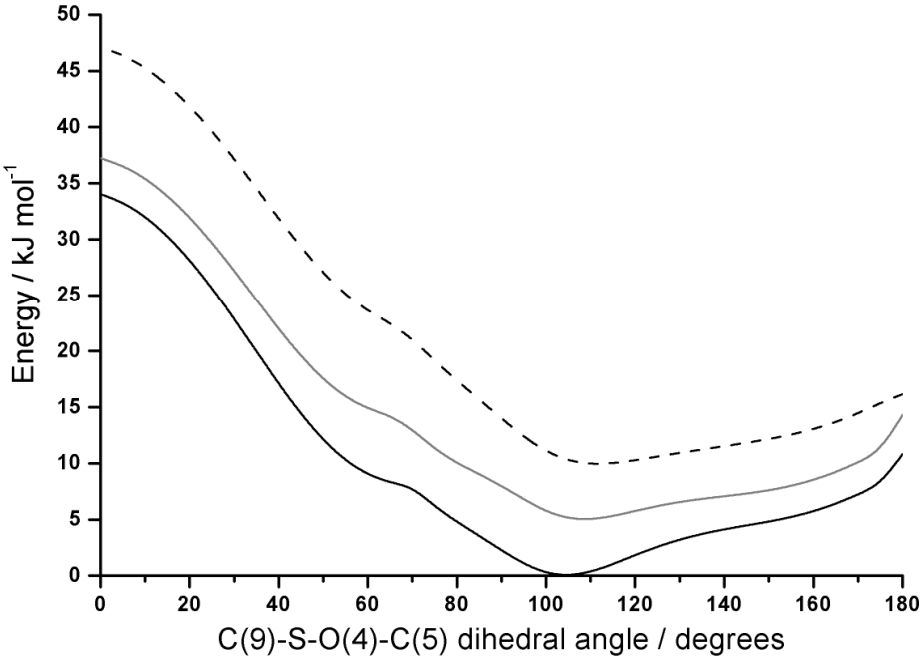

Figure 7.8 – Potential-energy curve for the C–S–O–C dihedral angle in $CF_3SO_2OCF_3$ calculated at HF/6-31G(d) (dashed), MP2/6-31G(d) (grey) and MP2 with 6-31G(d) basis on all atoms except S, for which a 6-31G(3df) basis set was used (black).

The average bond lengths for each type of internuclear distance in the GED refinement are presented in **Table 7.6** alongside the corresponding values calculated using a variety of methods. The largest discrepancy between the bond lengths in the GED structure and those predicted by MP2/6-31G(3df), on which the restraints were based, is the S–C bond length, found to be 2.5 pm shorter experimentally. In the GED study of the related compound, $CF_3SO_2OCH_3$,[4] the S–C bond length was found to be 183.8(2) pm. It was also calculated at the HF/3-21G(d) and B3LYP/6-31G(d) levels to be 176.9 and 187.1 pm, respectively, indicating that the S–C distance in

Table 7.6 – Selected GED (r_{h1}) and *ab initio* (r_e) *g*eometric parameters for $CF_3SO_2OCF_3$.[a]

	GED	HF / 6-31G(d)	MP2 / 6-31G(d)	6-311+G(d)	[b]	6-31G(3df)	B3LYP / 6-31G(3df)
r C–F average	133.3(2)	130.2	133.3	132.5	133.5	131.9	132.6
r S–O	161.5(4)	160.3	167.7	167.1	163.0	162.2	163.6
r S=O average	141.9(3)	140.9	144.7	143.4	143.0	141.9	142.0
r C–O	139.3(7)	137.4	139.3	138.5	140.0	139.0	139.5
r C–S	181.3(4)	182.1	184.5	186.3	183.0	183.8	187.4
ϕ C–S–O–C	119.5(18)	111.2	108.4	110.7	104.4	105.6	105.8
Energy [c]	–	-1294.37965	-1296.33296	-1296.89381	-1296.40638	-1297.08949	-1299.16761

[a] Distances are in pm and angles are in degrees.

[b] 6-31G(3df) basis on S, 6-31G(d) basis on C, O and F.

[c] Electronic energy in Hartrees, not corrected for zero-point vibrational energy.

$CF_3SO_2OCF_3$ may be highly dependent on the level of theory. However, the series of calculations in **Table 7.6** indicate that these theoretical values were probably extreme examples rather typical ones.

Surprisingly, the HF/6-31G(d) S–C distance was closest to that determined by GED. Inclusion of correlation energy using MP2 theory makes the agreement poorer and adopting the larger 6-311+G(d) basis makes it worse still. However, if the basis set size is increased by adding extra polarisation functions by way of a 6-31G(3df) basis set, the agreement improves and adoption of this basis set on only sulfur is sufficient for a good agreement between theory and experiment. The accurate prediction by HF/6-31G(d) therefore appears to be due to a cancellation of errors introduced by the lack of correlation energy and a basis-set deficiency on sulfur. The B3LYP/6-31G(3df) value is also given in **Table 7.6** for comparison. This method overestimates this bond length by 6.1 pm, with respect to the GED value, and is 3.6 pm longer than the MP2 value using the same basis set.

The S–O bond length, which for similar compounds is generally poorly defined by theory (as highlighted in **Section 7.1**), follows a similar trend. In this case, however, the GED value is only 0.7 pm shorter than the value predicted by the MP2/6-31G(3df) calculation and although the HF/6-31G(d) calculation again predicts a reasonable distance, it underestimates it by about 1 pm. The S–O bond is even more sensitive to method and basis set than the S–C distance. It increases by over 7 pm when MP2 theory is introduced in place of HF when the 6-31G(d) basis set is used. In contrast to the S–C distance, the S–O bond length is changed little by introduction of the larger 6-311+G(d) basis set, but as was the case for the S–C distance, additional polarisation functions on sulfur are essential for an accurate S–O value. Finally, the B3LYP functional predicts a reasonable S–O distance, but is still 1.4 pm farther from the experimental value than the MP2 calculation with the 6-31G(3df) basis set.

7.4.2. $CH_3SO_2SCH_3$

The bonded distances obtained from the GED refinement are compared with those calculated by theory in **Table 7.7**. As was found for $CF_3SO_2OCF_3$, the RHF/6-31G(d) values are remarkably close to the GED values and, for most bonded distances, the inclusion of electron correlation energy using MP2 or B3LYP methods makes the agreement substantially worse. The C–S(5) distance, analogous to the C–S distance in $CF_3SO_2OCF_3$ (the distance least well predicted by theory), does not show much variation between methods and basis sets and is reasonably well predicted by all combinations.

The S–S distance analogous to the S–O single bond in $CF_3SO_2OCF_3$ does, however, show a similar strong dependence on the method and basis set. In combination with the 6-31G(d) basis set, HF underestimates the S–S bond length by about 1 pm, whereas the MP2 and B3LYP methods overestimate it by about 2.5 and 7 pm, respectively. Again, a standard increase of the basis set size to 6-311G(d) has little effect, but inclusion of multiple polarisation functions using the 6-311G(3df,3pd) basis brings it back in line with the experimental geometry. As was found for $CF_3SO_2OCF_3$, the whole molecule does not require such a large basis set and a reliable structure can be obtained using the 6-311G(d) basis on all the atoms other than sulfur, for which the larger polarised basis set is required.

As a final note on the bond lengths in these compounds, the S=O distances are also sensitive to the method and basis set, albeit to a lesser extent. They are marginally underestimated by HF/6-31(d), by no more than 1 pm, but inclusion of electron correlation energy in the calculation lengthens the theoretical S=O distances by 3 to 4 pm, with little difference between the MP2 and B3LYP methods. In contrast to the single bonds to sulfur, adoption of a larger basis set brings these distances closer to the experimental values and, when the 3df polarisation functions are also included on sulfur, reliable theoretical values can be obtained.

Table 7.7 – Selected GED (r_{h1}) and *ab initio* (r_e) *g*eometric parameters for $CH_3SO_2SCH_3$ (distances in pm, angles in °).

	GED	RHF 6-31G(d)	B3LYP 6-31G(d)	MP2 6-31G(d)	6-311G(d)	[a]	6-311G(3df,3pd)	6-311G(3df,3pd)[b]
r C–S(5)	178.5(3)	177.4	180.9	178.4	178.2	177.2	176.5	176.0
r C–S(12)	182.2(3)	181.7	183.2	181.4	180.9	181.1	180.4	180.6
r S=O(6)	143.3(1)	143.0	146.5	146.3	145.0	143.3	143.4	143.8
r S=O(7)	143.6(1)	143.3	146.9	146.8	145.4	143.6	143.7	143.8
r S–S	207.5(1)	206.5	214.4	210.1	211.3	207.2	206.9	208.8
r C–H mean	108.9(3)	108.1	109.3	109.1	109.0	109.1	108.6	108.6
ϕ C–S–S–C	80.1(25)	82.5	86.3	83.5	83.2	82.4	81.2	180.0
Energy [c]	–	–1023.88881	–1026.58761	–1024.78060	–1024.93463	–1025.09562	–1025.28636	–1025.28327

[a] 6-311G(3df) basis on S, 6-311G(d) basis on C, H and O.

[b] C_s conformer.

[c] Units of energy are Hartrees. Not corrected for zero-point energy.

Potential-energy scans of the C–S–S–C torsion are shown in **Figure 7.9**. These show good agreement between the MP2 and B3LYP methods, both identifying two minima, mirror images, with C–S(12) approximately *gauche* with respect to the C–S(5) bond. The HF scan also predicted the *gauche* conformer to be the most stable, but predicted a third, barely stable conformer with C_s symmetry, approximately 6 kJ mol^{-1} higher in energy than those with C_1 symmetry. A possible origin of this C_s local minimum is the shortening of the S–S bond length predicted by HF with respect to the values arising from MP2 and B3LYP, which would increase the repulsive eclipsing interactions when C–S–S–C = 0, 120 and 240°.

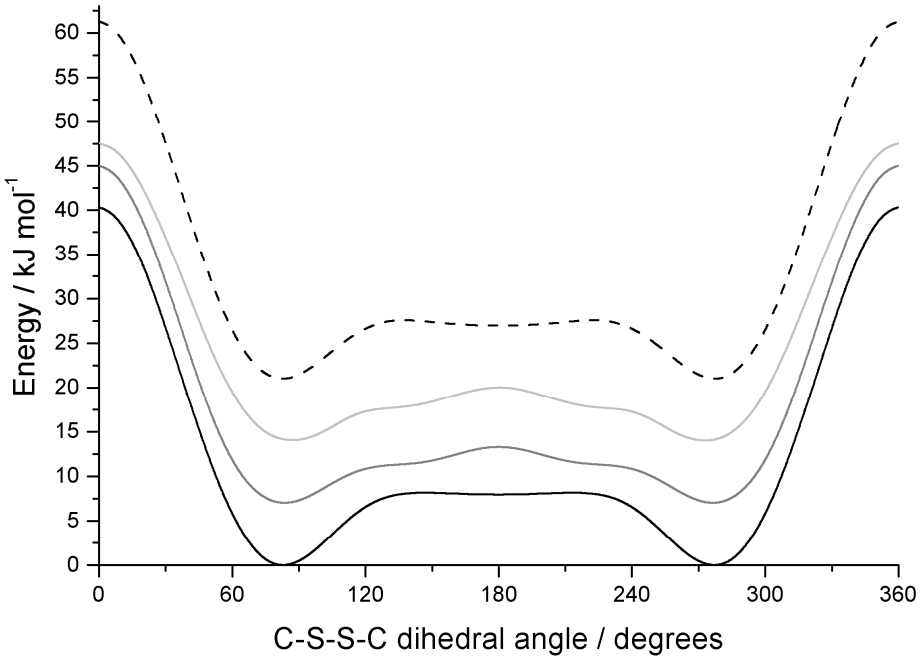

Figure 7.9 – Torsional potential about the S–S bond in $CH_3SO_2SCH_3$ calculated in 5° increments using HF/6-31G(d) (dashed), B3LYP/6-31G(d) (light grey), MP2/6-31G(d) (dark grey), and MP2 with a 6-31G(d) basis set on all atoms except sulfur, for which a 6-31G(3df) basis set was used (black).

As mentioned above, the S–S bond length is better predicted by HF/6-31G(d) than by MP2 or B3LYP with the same basis set, which was attributed to a cancellation of errors introduced by the basis-set deficiency on sulfur and the omission of correlation energy by HF. A second MP2 scan was therefore performed using a 6-31G(3df) basis

set on sulfur (lowest curve in **Figure 7.9**) and revealed a very flat potential-energy curve in the C–S–S–C range 140–220°, with a shallow local minimum at 180°. The optimized geometry of this structure was calculated and frequency calculations at the same level revealed only real frequencies, strengthening the argument for the presence of a metastable C_s-symmetric conformer.

The difference in energy between the optimized equilibrium geometries of the C_1 and C_s conformers was calculated at this level to be 8.0 kJ mol^{-1}. However, the corresponding free energy difference at the GED experimental temperature (*ca.* 400 K) was calculated to be only 1.3 kJ mol^{-1}, corresponding to a Boltzmann population of *ca.* 25%. An attempt was made to confirm the presence of this conformer experimentally by adding a C_s conformer to the GED model, but because of the similarities of the radial-distribution functions of the two conformers, no useful information was obtained.

7.5. Conclusions

The molecular structures of $CF_3SO_2OCF_3$ and $CH_3SO_2SCH_3$ were obtained by GED using models containing single conformers, with the C–S–O–C and C–S–S–C angles refining to 119.5(18)° and 80.1(25)°, respectively. As was found in the GED investigation of FSO_2OF and FSO_2OCl,[3] these structures were in good agreement with those obtained by HF theory using a 6-31G(d) basis set. However, improvement of the theoretical treatment using MP2 theory made the agreement between the experimental and calculated structures significantly worse and the B3LYP method yielded very poor geometrical parameters. Use of the larger 6-311G(d) basis set did not improve the agreement, but addition of additional polarisation functions on just the sulfur atoms using the 6-31G(3df) or 6-311G(3df) bases produced theoretical structures close to the GED ones.

7.6. References

1. I. Hargittai, R. Seip, C. O. Nair and J. E. Boggs, *J. Mol. Struct.* (1977), **39**, 1.
2. I. Hargittai, G. Schultz and M. Colonits, *J. Chem. Soc., Dalton Trans.* (1977), 1299.
3. F. Aubke, B. Casper, H. S. P. Müller, H. Oberhammer and H. Willner, *J. Mol. Struct.* (1995), **346**, 111.
4. F. Trautner, A. Ben Altabef, L. E. Fernandez, E. L. Varetti and H. Oberhammer, *Inorg. Chem.* (1999), **38**, 3051.
5. M. F. Erben, C. O. D. Védova, R. Boese, H. Willner, C. Leibold and H. Oberhammer, *Inorg. Chem.* (2003), **42**, 7297.
6. C. Leibold, H. Oberhammer, T. D. Thomas, L. J. Saethre, R. Winter and G. L. Gard, *Inorg. Chem.* (2004), **43**, 3942.
7. C. O. D. Védova, A. J. Downs, V. P. Novikov, H. Oberhammer, S. Parsons, R. M. Romano and A. Zawadski, *Inorg. Chem.* (2004), **43**, 4064.
8. F. Trautner, C. O. D. Védova, R. M. Romano and H. Oberhammer, *J. Mol. Struct.* (2006), **784**, 272.
9. Gaussian 03, Revision B.03, M. J. Frisch, G. W. Trucks, H. B. Schlegel, G. E. Scuseria, M. A. Robb, J. R. Cheeseman, J. A. Montgomery, Jr., T. Vreven, K. N. Kudin, J. C. Burant, J. M. Millam, S. S. Iyengar, J. Tomasi, V. Barone, B. Mennucci, M. Cossi, G. Scalmani, N. Rega, G. A. Petersson, H. Nakatsuji, M. Hada, M. Ehara, K. Toyota, R. Fukuda, J. Hasegawa, M. Ishida, T. Nakajima, Y. Honda, O. Kitao, H. Nakai, M. Klene, X. Li, J. E. Knox, H. P. Hratchian, J. B. Cross, C. Adamo, J. Jaramillo, R. Gomperts, R. E. Stratmann, O. Yazyev, A. J. Austin, R. Cammi, C. Pomelli, J. W. Ochterski, P. Y. Ayala, K. Morokuma, G. A. Voth, P. Salvador, J. J. Dannenberg, V. G. Zakrzewski, S. Dapprich, A. D. Daniels, M. C. Strain, O. Farkas, D. K. Malick, A. D. Rabuck, K. Raghavachari, J. B. Foresman, J. V. Ortiz, Q. Cui, A. G. Baboul, S. Clifford, J. Cioslowski, B. B. Stefanov, G. Liu, A. Liashenko, P. Piskorz, I. Komaromi, R. L. Martin, D. J. Fox, T. Keith, M. A. Al-Laham, C. Y. Peng, A. Nanayakkara, M. Challacombe, P. M. W. Gill, B. Johnson, W. Chen, M. W. Wong, C. Gonzalez and J. A. Pople, Gaussian, Inc., Wallingford CT, (2003).
10. J. S, Binkley, J. A. Pople and W. J. Hehre, *J. Am. Chem. Soc.* (1980), **102**, 939.
11. W. J. Pietro, M. M. Francl, W. J. Hehre, D. J. DeFrees, J. A. Pople and J. S. Binkley, *J. Am. Chem. Soc.* (1982), **104**, 5039.
12. W. H. Hehre, R. Ditchfield and J. A. Pople, *J. Chem. Phys.* (1972), **56**, 2257.
13. P. C. Hariharan and J. A. Pople, *Theor. Chim. Acta* (1973), **28**, 213.
14. M. S. Gordon, *Chem. Phys. Lett.* (1980), **76**, 163.
15. C. Møller and M. S. Plesset, *Phys. Rev.* (1934), **46**, 618.

16. A. D. McLean and G. S. Chandler, *J. Chem. Phys.* (1980), **72**, 5639.

17. T. Clark, J. Chandrasekhar, G. W. Spitznagel and P. v R. Schleyer, *J. Comp. Chem.* (1983), **4**, 294.

18. M. J. Frisch, J. A. Pople and J. S. Binkley, *J. Chem. Phys.* (1984), **80**, 3265.

19. A. D. Becke, *J. Chem. Phys.* (1993), **98**, 5648.

20. C. Lee, W. Yang, R. G. Parr, *Phys. Rev. B* (1988), **37**, 785.

21. V. A. Sipachev, *J. Mol. Struct.* (*THEOCHEM*) (1985), **121**, 143.

22. (a) A. J. Blake, P. T. Brain, H. McNab, J. Miller, C. A. Morrison, S. Parsons, D. W. H. Rankin, H. E. Robertson and B. A. Smart, *J. Phys. Chem.* (1996), **100**, 12280. (b) N. W. Mitzel and D. W. H. Rankin, *J. Chem. Soc., Dalton Trans.* (2003), 3650.

23. C. M. Huntley, G. S. Laurenson and D. W. H. Rankin, *J. Chem. Soc., Dalton Trans.* (1980), 954.

24. H. Fleischer, D. A. Wann, S. L. Hinchley, K. B. Borisenko, J. R. Lewis, R. J. Mawhorter, H. E. Robertson and D. W. H. Rankin, *Dalton Trans.* (2005), 3221.

25. S. L. Hinchley, H. E. Robertson, K. B. Borisenko, A. R. Turner, B. F. Johnston, D. W. H. Rankin, M. Ahmadian, J. N. Jones and A. H. Cowley, *Dalton Trans.* (2004), 2469.

26. A. W. Ross, M. Fink and R. Hilderbrandt, *International Tables for Crystallography*, (Ed.: Wilson, A. J. C. Kluwer Academic Publishers, Dordrecht, Boston, and London, Vol. C, p. 245, (1992).

Appendix 1

A program for manipulating images produced by the CCD camera

```
program image
implicit none
real r1,r2,c
integer i,j,k
integer recl
integer(2) img(1024,1024)


inquire(iolength=recl) img(1,:)

! read image from file
open(50,file='in.raw',access='DIRECT',form='UNFORMATTED',recl=recl)
do i=1,1024
  read(50,rec=i) img(i,:)
end do
close(50)

!******** convert signed to unsigned integer **************
do i=1,1024
  do j=1,1024
    k=img(i,j)
    if (k.lt.0) k=k+65536

            c=k

!*** calculate distance from diffraction centre, r2 ******
    r2=sqrt((512.5-i)**2+(512.5-j)**2)
```

```
!******************** Multiply by r2^3 *********************
   c=c*0.000001*(r2**3)

!********* find distance from image centre ***************
   r1=sqrt((512.2-i)**2+(512.5-j)**2)

!***** correct for filter *********************************
   c=0.025*c*exp(2*2.3025*(1.-(r1/524.0)))

!******************** Convert reals back to integers ******
            if (c.gt.65535.0) c=65535.0

            k=nint(c)

!******** convert back to signed integer **************
   if (k.gt.32767) k=k-65536
   img(i,j)=k
  end do
end do



! write image to file
open(50,file='out.raw',access='DIRECT',form='UNFORMATTED',recl=recl)
do i=1,1024
  write(50,rec=i) img(i,:)
end do
close(50)

end program
```

Appendix 2

A program for simulating data for a finite beam size

Explanation

This program uses a simplified approach for generating intensity curves for a finite beam size and an error in the centring procedure. The basic approach is to integrate over the probabilities for all possible errors in the assumed *s*-value (*s′*) due to the width of the electron beam, σ, up to a certain value. Similarly, the integration is performed for all the errors in the assumed *s*-value (*s″*) due to an error in the diffraction pattern centre. It uses the equation below, where the integrals are replaced by summations depending on the value of Δs in the input file (Itot.in).

$$I(s)_{simulated} = \iint \frac{I(s+s'+s'')_{theoretical}}{\sin\left(\cos^{-1}\left[\frac{s''}{centre\ error}\right]\right)} \times \exp\left(\frac{-s'^2}{2\sigma^2}\right) ds'\,ds''$$

The exponential term accounts for the beam size, whilst the trigonometric part accounts for a centring error. This equation assumes that the radius on the camera face is proportional to the corresponding value of the scattering vector, *s*, which is approximately correct for small angles. In addition, the problem has been simplified to a one-dimensional problem, whereas a thorough approach would require consideration of a two-dimensional diffraction pattern.

Program

```
program finite_beam
implicit none
real a,b,c,d,e,f,g,s,smin,sminy,pi,rbeam,sbeam,ebeam,elambda,deltas
real, dimension(4000) :: x
```

```
real, dimension(4000) :: y
integer i,j,k,l,m,n

pi=acos(-1.0)

!---------------------------- Input parameters ---------------------------------

!**** Nozzle-to-camera dist
b=205.5

!******** Standard deviation of beam / mm *****
rbeam=0.1

!******** Error in centre / mm *******
a=0.1

!**** Number of i points for integration over beam ****
n=29

!**** number of data points in file 'in.dat'****
m=150

!**** starting s value in 'in.dat' / angstroms-1 **********************
smin=0.2

!**** delta s in 'xxxx.in' file / angstroms-1 ****
deltas=0.2

!**** electron wavelength / angstroms ***
elambda=0.06125



!--------------------------------- Calcluations -------------------------------------

! Calculate s value corresponding to beam size at a nozzle-to-camera distance of b
sbeam=4.0*pi*sin(0.5*atan(rbeam/b))/elambda
```

```
! Calculate value of s corresponding to error in centre
c=4*pi*sin(0.5*atan(a/b))/elambda

! Calculate number of j points for integration over centre
l=1
2*int(c/deltas)+1

! Calculate s min for y
sminy=smin+0.5*deltas*(n-1)+deltas*int(c/deltas)

!------------------------------- Program Start -------------------------------------

!**** Open input intesity file
OPEN(unit=10,file='Itot.in')

!**** Calculate modified intensities
Do i=1,m
READ(10,*) x(i)
Enddo
CLOSE(10)

first: Do i=1,(m-l-n+2)
! s-value corresponding to i in x(i) = smin + (i-1)*detas
  second: Do j=1,l
! displacement of beam due to error in centre
    f=deltas*(j-1-(l-1)*0.5)

    third: Do k=1,n
! displacement of beam due to finite width
              ebeam=deltas*(k-1-0.5*(n-1))
              y(i)=y(i)+x(i+j+k-2)*exp(-ebeam**2/(2*sbeam**2))/(sin(acos(f/c)))

            End do third
  End do second

  s=(i-1)*deltas+sminy
```

```
  y(i)=0.00003*y(i)*s**4/(l*rbeam)

End do first


!---------------------------------- Output Data ----------------------------------

! Open the output file
OPEN(unit=20,FILE='out.dat',status='unknown',access='sequential',action='write')
  WRITE(20,FMT='(F6.4)') sminy
DO i=1,(m-l-n+2)
  WRITE(20,FMT='(F19.9)') y(i)
END DO

! Close the output file
CLOSE(20)

end program
```

Appendix 3

Supplementary data for the GED refinement of *arachno*-6,9-$C_2B_8H_{14}$

Table A3.1 – Least-squares correlation matrix.[a]

	p_2	p_4	p_5	p_6	p_7	p_{10}	p_{16}	u_{108}	k_2
p_1	67	84	64		–74		–86		
p_2					–62				
p_4			66	54	–53		–98		
p_5					–81		–73		
p_6								–54	
p_7							64		
p_8						57			
u_2								51	58

[a] All elements are multiplied by 100 and only off-diagonal elements with absolute values ≥ 50% are included. k_2 is the scale factor for the short nozzle-to-camera distance.

Table A3.2 Selected distances (r_a/pm), amplitudes of vibration (u_{h1}/pm) and perpendicular corrections (k_{h1}/pm) from the GED refinement and calculations (RHF/6-31G*).

	Atom pair	r_a	u_{h1} (GED)	k_{h1}	u_{h1} (calculated)
u_{33}	C(9)-H(22)	109.8(6)	8.8(tied to u_{25})	0.3	7.4
u_{25}	C(6)-H(21)	109.8(6)	8.8(4)	0.3	7.4
u_{32}	C(9)-H(19)	109.8(6)	8.7(tied to u_{25})	0.4	7.3
u_{24}	C(6)-H(16)	109.8(6)	8.7(tied to u_{25})	0.4	7.3
u_{15}	B(3)-H(13)	119.7(3)	9.6(tied to u_{25})	0.4	8.1
u_6	B(1)-H(11)	119.7(3)	9.6(tied to u_{25})	0.4	8.1
u_{26}	B(7)-H(17)	119.7(3)	9.6(tied to u_{25})	0.4	8.1
u_{34}	B(10)-H(20)	119.7(3)	9.6(tied to u_{25})	0.4	8.1
u_{29}	B(8)-H(18)	119.7(3)	9.6(tied to u_{25})	0.4	8.1
u_{21}	B(5)-H(15)	119.7(3)	9.6(tied to u_{25})	0.4	8.1
u_{11}	B(2)-H(12)	119.7(3)	9.6(tied to u_{25})	0.4	8.1
u_{19}	B(4)-H(14)	119.7(3)	9.6(tied to u_{25})	0.4	8.1

u_{27}	B(7)-H(24)	132.6(5)	12.1(tied to u_{25})	1.0	10.2
u_{22}	B(5)-H(23)	132.6(5)	12.1(tied to u_{25})	1.0	10.2
u_{30}	B(8)-H(24)	132.7(5)	12.1(tied to u_{25})	1.0	10.2
u_{35}	B(10)-H(23)	132.7(5)	12.1(tied to u_{25})	1.0	10.2
u_{9}	B(2)-C(6)	167.0(4)	6.9(2)	0.3	6.7
u_{17}	B(4)-C(9)	167.0(4)	6.9(tied to u_{9})	0.3	6.7
u_{23}	C(6)-B(7)	174.9(2)	8.2(tied to u_{9})	0.2	8.0
u_{28}	B(8)-C(9)	174.9(2)	8.2(tied to u_{9})	0.2	8.0
u_{20}	B(5)-C(6)	174.9(2)	8.2(tied to u_{9})	0.2	8.0
u_{31}	C(9)-B(10)	174.9(2)	8.2(tied to u_{9})	0.2	8.0
u_{12}	B(3)-B(4)	175.2(2)	6.6(tied to u_{9})	0.3	6.4
u_{3}	B(1)-B(4)	175.2(2)	6.6(tied to u_{9})	0.3	6.4
u_{7}	B(2)-B(3)	175.2(2)	6.6(tied to u_{9})	0.3	6.4
u_{1}	B(1)-B(2)	175.2(2)	6.6(tied to u_{9})	0.3	6.4
u_{18}	B(4)-B(10)	178.6(3)	7.0(tied to u_{9})	0.3	6.8
u_{16}	B(4)-B(8)	178.6(3)	7.0(tied to u_{9})	0.3	6.8
u_{10}	B(2)-B(7)	178.6(3)	7.0(tied to u_{9})	0.3	6.8
u_{8}	B(2)-B(5)	178.6(3)	7.0(tied to u_{9})	0.3	6.8
u_{5}	B(1)-B(10)	180.0(4)	7.4(tied to u_{9})	0.2	7.2
u_{14}	B(3)-B(8)	180.0(4)	7.4(tied to u_{9})	0.2	7.2
u_{13}	B(3)-B(7)	180.0(4)	7.4(tied to u_{9})	0.2	7.2
u_{4}	B(1)-B(5)	180.0(4)	7.4(tied to u_{9})	0.2	7.2
u_{2}	B(1)-B(3)	182.2(4)	7.1(tied to u_{9})	0.4	6.9
u_{134}	B(7)...B(8)	187.5(4)	8.1(tied to u_{9})	-0.2	7.8
u_{106}	B(5)...B(10)	187.5(4)	8.1(tied to u_{9})	-0.2	7.8
u_{116}	B(5)...H(21)	219.7(7)	11.9(tied to u_{170})	-0.3	12.8
u_{146}	B(7)...H(21)	219.7(7)	11.9(tied to u_{170})	-0.3	12.8
u_{184}	B(10)...H(22)	219.7(7)	11.9(tied to u_{170})	-0.3	12.8
u_{160}	B(8)...H(22)	219.7(7)	11.9(tied to u_{170})	-0.2	12.8
u_{61}	B(2)...H(16)	228.5(9)	10.8(tied to u_{170})	-0.3	11.6
u_{97}	B(4)...H(19)	228.5(9)	10.8(tied to u_{170})	-0.3	11.6
u_{133}	C(6)...H(24)	233.1(8)	12.1(tied to u_{170})	0.2	13.0
u_{132}	C(6)...H(23)	233.1(8)	12.1(tied to u_{170})	0.2	13.0
u_{173}	C(9)...H(24)	233.1(8)	12.1(tied to u_{170})	0.2	13.0
u_{172}	C(9)...H(23)	233.1(8)	12.1(tied to u_{170})	0.2	13.0
u_{123}	C(6)...H(12)	238.7(10)	10.8(tied to u_{170})	-0.2	11.6

u_{165}	C(9)...H(14)	238.7(10)	10.8(tied to u_{170})	-0.2	11.6
u_{142}	B(7)...H(16)	244.4(6)	11.2(tied to u_{170})	-0.3	12.1
u_{111}	B(5)...H(16)	244.4(6)	11.2(tied to u_{170})	-0.3	12.1
u_{182}	B(10)...H(19)	244.4(6)	11.2(tied to u_{170})	-0.3	12.1
u_{157}	B(8)...H(19)	244.4(6)	11.2(tied to u_{170})	-0.3	12.1
u_{86}	B(3)...H(24)	247.4(10)	10.0(tied to u_{170})	0.6	10.8
u_{51}	B(1)...H(23)	247.4(10)	10.0(tied to u_{170})	0.6	10.8
u_{177}	B(10)...H(14)	256.8(5)	11.6(tied to u_{170})	-0.2	12.5
u_{153}	B(8)...H(14)	256.8(5)	11.6(tied to u_{170})	-0.2	12.5
u_{108}	B(5)...H(12)	256.8(5)	11.6(tied to u_{170})	-0.2	12.5
u_{138}	B(7)...H(12)	256.8(5)	11.6(tied to u_{170})	-0.2	12.5
u_{170}	C(9)...H(20)	256.9(9)	11.3(4)	-0.3	12.1
u_{127}	C(6)...H(17)	256.9(9)	11.3(tied to u_{170})	-0.3	12.1
u_{126}	C(6)...H(15)	256.9(9)	11.3(tied to u_{170})	-0.3	12.1
u_{169}	C(9)...H(18)	256.9(9)	11.3(tied to u_{170})	-0.3	12.1
u_{92}	B(4)...H(13)	257.9(5)	11.1(tied to u_{170})	-0.2	12.0
u_{90}	B(4)...H(11)	257.9(5)	11.1(tied to u_{170})	-0.2	12.0
u_{58}	B(2)...H(13)	257.9(5)	11.1(tied to u_{170})	-0.2	12.0
u_{57}	B(2)...H(11)	257.9(5)	11.1(tied to u_{170})	-0.2	12.0
u_{96}	B(4)...H(18)	258.9(9)	11.4(tied to u_{170})	-0.4	12.3
u_{98}	B(4)...H(20)	258.9(9)	11.4(tied to u_{170})	-0.4	12.3
u_{62}	B(2)...H(17)	259.0(9)	11.4(tied to u_{170})	-0.4	12.3
u_{60}	B(2)...H(15)	259.0(9)	11.4(tied to u_{170})	-0.3	12.3
u_{66}	B(2)...H(21)	260.3(8)	10.3(tied to u_{170})	-0.9	11.1
u_{100}	B(4)...H(22)	260.3(8)	10.3(tied to u_{170})	-0.8	11.1
u_{48}	B(1)...H(20)	260.7(7)	11.6(tied to u_{170})	-0.5	12.5
u_{80}	B(3)...H(18)	260.7(7)	11.6(tied to u_{170})	-0.5	12.5
u_{79}	B(3)...H(17)	260.7(7)	11.6(tied to u_{170})	-0.5	12.5
u_{43}	B(1)...H(15)	260.7(7)	11.6(tied to u_{170})	-0.5	12.5
u_{76}	B(3)...H(14)	262.7(6)	10.7(tied to u_{170})	-0.2	11.5
u_{42}	B(1)...H(14)	262.7(6)	10.7(tied to u_{170})	-0.2	11.5
u_{75}	B(3)...H(12)	262.7(6)	10.7(tied to u_{170})	-0.2	11.5
u_{40}	B(1)...H(12)	262.7(6)	10.7(tied to u_{170})	-0.2	11.5
u_{74}	B(3)...H(11)	263.3(7)	11.4(tied to u_{170})	-0.1	12.2
u_{41}	B(1)...H(13)	263.3(7)	11.4(tied to u_{170})	-0.1	12.2
u_{152}	B(8)...H(13)	263.6(8)	11.4(tied to u_{170})	-0.3	12.3

u_{174}	B(10)...H(11)	263.7(8)	11.4(tied to u_{170})	-0.3	12.3
u_{139}	B(7)...H(13)	263.7(8)	11.4(tied to u_{170})	-0.3	12.3
u_{107}	B(5)...H(11)	263.7(8)	11.4(tied to u_{170})	-0.3	12.3
u_{171}	C(9)...H(21)	265.7(24)	17.9(tied to u_{170})	0.3	19.3
u_{131}	C(6)...H(22)	265.8(24)	17.9(tied to u_{170})	0.3	19.3
u_{115}	B(5)...H(20)	273.1(10)	11.7(tied to u_{170})	-0.8	12.6
u_{156}	B(8)...H(17)	273.1(10)	11.7(tied to u_{170})	-0.8	12.6
u_{143}	B(7)...H(18)	273.1(10)	11.7(tied to u_{170})	-0.8	12.6
u_{178}	B(10)...H(15)	273.1(10)	11.7(tied to u_{170})	-0.8	12.6
u_{53}	B(2)...B(4)	280.8(8)	7.4(tied to u_{71})	0.0	6.8
u_{71}	B(3)...C(6)	282.9(7)	7.9(2)	0.0	7.3
u_{36}	B(1)...C(6)	282.9(7)	7.9(tied to u_{71})	0.0	7.3
u_{72}	B(3)...C(9)	282.9(7)	7.9(tied to u_{71})	0.0	7.2
u_{39}	B(1)...C(9)	282.9(7)	7.9(tied to u_{71})	0.0	7.3
u_{69}	B(2)...H(24)	287.1(7)	13.5(tied to u_{71})	0.2	12.4
u_{68}	B(2)...H(23)	287.1(7)	13.5(tied to u_{71})	0.2	12.4
u_{101}	B(4)...H(23)	287.1(7)	13.5(tied to u_{71})	0.2	12.4
u_{102}	B(4)...H(24)	287.1(7)	13.5(tied to u_{71})	0.2	12.4
u_{159}	B(8)...H(21)	288.8(11)	18.3(tied to u_{71})	-0.1	16.8
u_{183}	B(10)...H(21)	288.8(11)	18.3(tied to u_{71})	-0.1	16.8
u_{117}	B(5)...H(22)	288.9(11)	18.3(tied to u_{71})	-0.1	16.8
u_{147}	B(7)...H(22)	288.9(11)	18.3(tied to u_{71})	-0.1	16.8
u_{54}	B(2)...B(8)	290.7(5)	8.2(tied to u_{71})	-0.1	7.6
u_{56}	B(2)...B(10)	290.7(5)	8.2(tied to u_{71})	-0.1	7.6
u_{87}	B(4)...B(5)	290.7(5)	8.2(tied to u_{71})	-0.1	7.6
u_{89}	B(4)...B(7)	290.7(5)	8.2(tied to u_{71})	-0.1	7.6
u_{149}	B(8)...B(10)	291.4(6)	8.2(tied to u_{71})	0.1	7.5
u_{103}	B(5)...B(7)	291.5(6)	8.2(tied to u_{71})	0.1	7.5
u_{38}	B(1)...B(8)	292.4(4)	7.9(tied to u_{71})	0.2	7.2
u_{73}	B(3)...B(10)	292.4(4)	7.9(tied to u_{71})	0.2	7.2
u_{70}	B(3)...B(5)	292.4(4)	7.9(tied to u_{71})	0.2	7.2
u_{37}	B(1)...B(7)	292.4(4)	7.9(tied to u_{71})	0.2	7.2
u_{121}	C(6)...B(10)	298.2(5)	9.5(tied to u_{71})	-0.4	8.7
u_{119}	C(6)...B(8)	298.2(5)	9.5(tied to u_{71})	-0.4	8.7
u_{135}	B(7)...C(9)	298.3(5)	9.5(tied to u_{71})	-0.4	8.7
u_{105}	B(5)...C(9)	298.3(5)	9.5(tied to u_{71})	-0.4	8.7

u_{120}	C(6)...C(9)	311.2(18)	12.1(tied to u_{71})	-0.6	11.2
u_{83}	B(3)...H(21)	334.4(13)	14.9(tied to u_{55})	-0.7	13.8
u_{49}	B(1)...H(21)	334.4(13)	14.9(tied to u_{55})	-0.7	13.8
u_{84}	B(3)...H(22)	334.5(13)	14.9(tied to u_{55})	-0.6	13.8
u_{50}	B(1)...H(22)	334.5(13)	14.9(tied to u_{55})	-0.6	13.8
u_{55}	B(2)...C(9)	339.5(9)	9.0(4)	-0.4	8.4
u_{88}	B(4)...C(6)	339.5(9)	9.0(tied to u_{55})	-0.4	8.4
u_{161}	B(8)...H(23)	343.4(8)	15.9(tied to u_{55})	-0.1	14.7
u_{185}	B(10)...H(24)	343.4(8)	15.9(tied to u_{55})	-0.1	14.7
u_{148}	B(7)...H(23)	343.4(8)	15.9(tied to u_{55})	-0.1	14.7
u_{118}	B(5)...H(24)	343.4(8)	15.9(tied to u_{55})	-0.1	14.7
u_{136}	B(7)...B(10)	346.5(6)	8.6(tied to u_{55})	-0.2	8.0
u_{104}	B(5)...B(8)	346.5(6)	8.6(tied to u_{55})	-0.2	8.0
u_{99}	B(4)...H(21)	347.1(15)	18.2(tied to u_{55})	-0.5	16.9
u_{67}	B(2)...H(22)	347.2(15)	18.2(tied to u_{55})	-0.4	16.9
u_{85}	B(3)...H(23)	351.9(9)	13.8(tied to u_{55})	0.2	12.8
u_{52}	B(1)...H(24)	352.0(9)	13.8(tied to u_{55})	0.2	12.8
u_{78}	B(3)...H(16)	369.8(8)	12.1(tied to u_{55})	-0.8	11.2
u_{44}	B(1)...H(16)	369.8(8)	12.1(tied to u_{55})	-0.8	11.2
u_{81}	B(3)...H(19)	369.8(8)	12.1(tied to u_{55})	-0.8	11.2
u_{47}	B(1)...H(19)	369.8(8)	12.1(tied to u_{55})	-0.8	11.2
u_{124}	C(6)...H(13)	387.1(8)	12.7(tied to u_{122})	-0.8	11.4
u_{122}	C(6)...H(11)	387.1(8)	12.7(4)	-0.8	11.4
u_{162}	C(9)...H(11)	387.1(8)	12.7(tied to u_{122})	-0.8	11.4
u_{164}	C(9)...H(13)	387.1(8)	12.7(tied to u_{122})	-0.8	11.4
u_{91}	B(4)...H(12)	390.4(9)	12.0(tied to u_{122})	-0.8	10.7
u_{59}	B(2)...H(14)	390.4(9)	12.0(tied to u_{122})	-0.8	10.7
u_{158}	B(8)...H(20)	394.9(8)	12.7(tied to u_{122})	-0.9	11.4
u_{181}	B(10)...H(18)	394.9(8)	12.7(tied to u_{122})	-0.9	11.4
u_{112}	B(5)...H(17)	395.0(8)	12.7(tied to u_{122})	-0.9	11.4
u_{141}	B(7)...H(15)	395.0(8)	12.7(tied to u_{122})	-0.9	11.4
u_{82}	B(3)...H(20)	395.7(6)	12.7(tied to u_{122})	-0.8	11.4
u_{46}	B(1)...H(18)	395.7(6)	12.7(tied to u_{122})	-0.8	11.4
u_{45}	B(1)...H(17)	395.7(6)	12.7(tied to u_{122})	-0.8	11.4
u_{77}	B(3)...H(15)	395.7(6)	12.7(tied to u_{122})	-0.8	11.4
u_{65}	B(2)...H(20)	396.6(6)	12.8(tied to u_{122})	-1.1	11.5

u_{63}	B(2)...H(18)	396.6(6)	12.8(tied to u_{122})	-1.1	11.5
u_{95}	B(4)...H(17)	396.7(6)	12.8(tied to u_{122})	-1.1	11.5
u_{93}	B(4)...H(15)	396.7(6)	12.8(tied to u_{122})	-1.1	11.5
u_{155}	B(8)...H(16)	396.9(8)	13.0(tied to u_{122})	-1.4	11.6
u_{179}	B(10)...H(16)	396.9(8)	13.0(tied to u_{122})	-1.4	11.6
u_{144}	B(7)...H(19)	396.9(8)	13.0(tied to u_{122})	-1.3	11.6
u_{114}	B(5)...H(19)	396.9(8)	13.0(tied to u_{122})	-1.3	11.6
u_{176}	B(10)...H(13)	396.9(6)	12.7(tied to u_{122})	-0.7	11.4
u_{150}	B(8)...H(11)	396.9(6)	12.7(tied to u_{122})	-0.7	11.4
u_{137}	B(7)...H(11)	396.9(6)	12.7(tied to u_{122})	-0.6	11.4
u_{109}	B(5)...H(13)	397.0(6)	12.7(tied to u_{122})	-0.6	11.4
u_{175}	B(10)...H(12)	397.7(5)	12.8(tied to u_{122})	-1.0	11.5
u_{151}	B(8)...H(12)	397.7(5)	12.8(tied to u_{122})	-1.0	11.5
u_{140}	B(7)...H(14)	397.7(5)	12.8(tied to u_{122})	-1.0	11.5
u_{110}	B(5)...H(14)	397.7(5)	12.8(tied to u_{122})	-1.0	11.5
u_{130}	C(6)...H(20)	407.6(8)	13.3(tied to u_{122})	-1.3	11.9
u_{128}	C(6)...H(18)	407.6(8)	13.3(tied to u_{122})	-1.3	11.9
u_{166}	C(9)...H(15)	407.6(8)	13.3(tied to u_{122})	-1.3	11.9
u_{168}	C(9)...H(17)	407.6(8)	13.3(tied to u_{122})	-1.3	11.9
u_{167}	C(9)...H(16)	417.6(20)	15.3(tied to u_{122})	-1.6	13.7
u_{129}	C(6)...H(19)	417.6(20)	15.3(tied to u_{122})	-1.6	13.7
u_{94}	B(4)...H(16)	445.8(11)	11.4(tied to u_{125})	-1.4	10.7
u_{64}	B(2)...H(19)	445.8(11)	11.4(tied to u_{125})	-1.4	10.7
u_{125}	C(6)...H(14)	458.4(10)	12.0(9)	-1.4	11.3
u_{163}	C(9)...H(12)	458.4(10)	12.0(tied to u_{125})	-1.3	11.3
u_{154}	B(8)...H(15)	465.2(6)	11.7(tied to u_{125})	-1.3	11.0
u_{145}	B(7)...H(20)	465.2(6)	11.7(tied to u_{125})	-1.3	11.0
u_{180}	B(10)...H(17)	465.2(6)	11.7(tied to u_{125})	-1.3	11.0
u_{113}	B(5)...H(18)	465.2(6)	11.7(tied to u_{125})	-1.3	11.0

Appendix 4

Supplementary data for the GED refinement of *arachno*-6,9-CSB_8H_{12}

Table A4.1 – Least-squares correlation matrix.[a]

	p_{18}	p_{22}	u_{34}	u_{95}	u_{143}	u_{156}	k_1	k_2
p_8			–77	–55				
p_{13}	–52	–59						
u_{34}				50			59	51
u_{65}						53		
u_{95}					61			
k_1								60

[a] All elements are scaled by a factor of 100, and only off-diagonal elements with values ≥ 50% are included. k_1 and k_2 are scale factors.

Table A4.2 Interatomic distances (r_a) and amplitudes of vibration (u_{h1}) (all values in picometres).

	Atom pair	r_a	u_{h1} (GED)	u_{h1} (RHF/6-31G*)	k_{h1}
u_{25}	C(6)–H(16)	109.8(5)	7.1(3)	7.3	0.4
u_{26}	C(6)–H(20)	110.3(5)	7.1(tied to u_{25})	7.4	0.4
u_{19}	B(4)–H(14)	119.9(2)	7.7(tied to u_{25})	8.0	0.4
u_{28}	B(7)–H(17)	119.9(2)	7.7(tied to u_{25})	8.1	0.4
u_{15}	B(3)–H(13)	119.9(2)	7.8(tied to u_{25})	8.1	0.4
u_6	B(1)–H(11)	119.9(2)	7.8(tied to u_{25})	8.1	0.4
u_{22}	B(5)–H(15)	119.9(2)	7.7(tied to u_{25})	8.1	0.4
u_{31}	B(8)–H(18)	119.9(2)	7.7(tied to u_{25})	8.1	0.4
u_{11}	B(2)–H(12)	119.9(2)	7.7(tied to u_{25})	8.0	0.4
u_{34}	B(10)–H(19)	119.9(2)	7.7(tied to u_{25})	8.1	0.4
u_{23}	B(5)–H(21)	130.8(5)	9.4(tied to u_{25})	9.7	0.9
u_{29}	B(7)–H(22)	130.9(5)	9.4(tied to u_{25})	9.7	1.0
u_{32}	B(8)–H(22)	135.8(5)	10.1(tied to u_{25})	10.5	1.1
u_{35}	B(10)–H(21)	135.9(5)	10.1(tied to u_{25})	10.5	1.2

u_9	B(2)–C(6)	165.9(3)	6.5(tied to u_{33})	6.5	0.2
u_{20}	B(5)–C(6)	173.9(2)	7.6(tied to u_{33})	7.7	0.1
u_{24}	C(6)–B(7)	174.0(2)	7.6(tied to u_{33})	7.7	0.2
u_7	B(2)–B(3)	175.7(2)	6.4(tied to u_{33})	6.4	0.3
u_1	B(1)–B(2)	176.0(2)	6.4(tied to u_{33})	6.4	0.5
u_3	B(1)–B(4)	176.9(2)	6.6(tied to u_{33})	6.7	0.2
u_{12}	B(3)–B(4)	177.1(2)	6.6(tied to u_{33})	6.7	0.4
u_8	B(2)–B(5)	178.1(2)	6.6(tied to u_{33})	6.7	0.4
u_{10}	B(2)–B(7)	178.1(2)	6.6(tied to u_{33})	6.7	0.4
u_5	B(1)–B(10)	178.5(2)	6.9(tied to u_{33})	6.9	–0.1
u_{14}	B(3)–B(8)	178.9(2)	6.9(tied to u_{33})	6.9	0.4
u_2	B(1)–B(3)	180.8(2)	6.7(tied to u_{33})	6.8	0.4
u_{13}	B(3)–B(7)	182.1(2)	7.2(tied to u_{33})	7.3	0.1
u_4	B(1)–B(5)	182.3(2)	7.2(tied to u_{33})	7.3	0.2
u_{21}	B(5)–B(10)	185.0(3)	7.6(tied to u_{33})	7.6	–0.1
u_{27}	B(7)–B(8)	185.0(3)	7.6(tied to u_{33})	7.6	0.0
u_{16}	B(4)–B(8)	190.7(3)	8.3(tied to u_{33})	8.4	0.3
u_{18}	B(4)–B(10)	190.9(3)	8.4(tied to u_{33})	8.4	0.6
u_{33}	S(9)–B(10)	194.2(3)	6.7(2)	6.8	–0.2
u_{30}	B(8)–S(9)	194.3(3)	6.7(tied to u_{33})	6.8	–0.1
u_{17}	B(4)–S(9)	194.5(4)	8.7(tied to u_{33})	6.6	0.1
u_{106}	B(5)...H(20)	215.2(6)	13.8(tied to u_{154})	12.5	0.0
u_{131}	B(7)...H(20)	215.3(6)	13.8(tied to u_{154})	12.5	0.1
u_{59}	B(2)...H(16)	229.7(8)	12.8(tied to u_{154})	11.6	–0.2
u_{119}	C(6)...H(21)	234.6(13)	14.3(tied to u_{154})	12.9	0.6
u_{120}	C(6)...H(22)	234.6(13)	14.3(tied to u_{154})	12.9	0.7
u_{112}	C(6)...H(12)	237.8(7)	12.8(tied to u_{154})	11.6	–0.2
u_{102}	B(5)...H(16)	243.9(5)	13.2(tied to u_{154})	11.9	–0.3
u_{128}	B(7)...H(16)	244.0(5)	13.2(tied to u_{154})	11.9	–0.2
u_{49}	B(1)...H(21)	250.3(7)	11.9(tied to u_{154})	10.8	0.5
u_{80}	B(3)...H(22)	250.4(7)	11.9(tied to u_{154})	10.8	0.6
u_{84}	B(4)...H(11)	254.8(6)	13.7(tied to u_{154})	12.4	–0.3
u_{86}	B(4)...H(13)	254.9(6)	13.6(tied to u_{154})	12.3	–0.2
u_{63}	B(2)...H(20)	256.0(7)	12.2(tied to u_{154})	11.0	–0.4
u_{99}	B(5)...H(12)	256.1(4)	13.7(tied to u_{154})	12.4	–0.1
u_{124}	B(7)...H(12)	256.2(4)	13.7(tied to u_{154})	12.4	0.0

u_{115}	C(6)...H(15)	256.3(7)	13.3(tied to u_{154})	12.0	–0.5
u_{58}	B(2)...H(15)	256.3(8)	13.7(tied to u_{154})	12.4	–0.3
u_{116}	C(6)...H(17)	256.4(7)	13.3(tied to u_{154})	12.0	–0.3
u_{60}	B(2)...H(17)	256.4(8)	13.6(tied to u_{154})	12.3	–0.2
u_{56}	B(2)...H(13)	256.8(5)	13.3(tied to u_{154})	12.0	–0.3
u_{55}	B(2)...H(11)	257.0(5)	13.3(tied to u_{154})	12.0	–0.1
u_{154}	S(9)...H(21)	259.9(12)	14.5(3)	13.1	0.5
u_{155}	S(9)...H(22)	260.0(12)	14.5(tied to u_{154})	13.1	0.7
u_{75}	B(3)...H(17)	260.3(3)	13.9(tied to u_{154})	12.6	–0.4
u_{47}	B(1)...H(19)	260.3(6)	13.5(tied to u_{154})	12.3	–0.5
u_{43}	B(1)...H(15)	260.4(3)	13.9(tied to u_{154})	12.6	–0.3
u_{76}	B(3)...H(18)	260.8(6)	13.5(tied to u_{154})	12.2	0.0
u_{42}	B(1)...H(14)	261.2(6)	13.1(tied to u_{154})	11.9	–0.2
u_{72}	B(3)...H(14)	261.4(6)	13.1(tied to u_{154})	11.9	–0.1
u_{70}	B(3)...H(11)	262.0(3)	13.4(tied to u_{154})	12.1	–0.1
u_{41}	B(1)...H(13)	262.1(3)	13.3(tied to u_{154})	12.1	–0.1
u_{71}	B(3)...H(12)	262.3(5)	12.8(tied to u_{154})	11.6	–0.2
u_{156}	B(10)...H(11)	262.6(4)	13.5(tied to u_{154})	12.2	–0.5
u_{40}	B(1)...H(12)	262.6(5)	12.8(tied to u_{154})	11.6	0.1
u_{136}	B(8)...H(13)	263.0(4)	13.5(tied to u_{154})	12.2	–0.1
u_{125}	B(7)...H(13)	264.1(5)	13.7(tied to u_{154})	12.4	–0.4
u_{98}	B(5)...H(11)	264.2(5)	13.7(tied to u_{154})	12.4	–0.3
u_{152}	S(9)...H(19)	264.4(10)	13.4(tied to u_{154})	12.1	–0.7
u_{151}	S(9)...H(18)	264.5(10)	13.4(tied to u_{154})	12.1	–0.6
u_{90}	B(4)...H(18)	267.4(10)	13.7(tied to u_{67})	13.3	–0.2
u_{91}	B(4)...H(19)	267.7(10)	13.7(tied to u_{67})	13.3	0.1
u_{147}	S(9)...H(14)	269.2(7)	12.0(tied to u_{67})	11.6	–0.3
u_{105}	B(5)...H(19)	269.8(10)	12.8(tied to u_{67})	12.4	–0.7
u_{129}	B(7)...H(18)	269.9(10)	12.8(tied to u_{67})	12.4	–0.7
u_{160}	B(10)...H(15)	270.3(9)	13.0(tied to u_{67})	12.6	–0.7
u_{140}	B(8)...H(17)	270.3(9)	13.0(tied to u_{67})	12.5	–0.7
u_{137}	B(8)...H(14)	276.6(5)	14.3(tied to u_{67})	13.8	–0.2
u_{159}	B(10)...H(14)	276.8(5)	14.3(tied to u_{67})	13.8	0.0
u_{153}	S(9)...H(20)	281.4(17)	22.9(tied to u_{67})	22.2	1.2
u_{142}	B(8)...H(20)	281.9(11)	17.8(tied to u_{67})	17.2	0.5
u_{164}	B(10)...H(20)	282.0(11)	17.8(tied to u_{67})	17.2	0.6

u_{67}	B(3)...C(6)	283.6(4)	7.4(2)	7.2	–0.1
u_{36}	B(1)...C(6)	283.7(4)	7.5(tied to u_{67})	7.2	0.0
u_{65}	B(2)...H(22)	287.9(8)	12.5(tied to u_{67})	12.1	0.5
u_{64}	B(2)...H(21)	287.9(8)	12.5(tied to u_{67})	12.1	0.5
u_{54}	B(2)...B(10)	288.4(3)	7.7(tied to u_{67})	7.4	0.0
u_{52}	B(2)...B(8)	288.4(3)	7.7(tied to u_{67})	7.4	0.0
u_{51}	B(2)...B(4)	289.0(4)	7.2(tied to u_{67})	7.0	0.3
u_{95}	B(5)...B(7)	290.6(6)	7.8(tied to u_{67})	7.6	0.0
u_{38}	B(1)...B(8)	292.0(2)	7.6(tied to u_{67})	7.4	–0.1
u_{69}	B(3)...B(10)	292.1(2)	7.6(tied to u_{67})	7.4	0.1
u_{66}	B(3)...B(5)	292.8(3)	7.5(tied to u_{67})	7.3	0.1
u_{37}	B(1)...B(7)	292.8(3)	7.5(tied to u_{67})	7.3	0.2
u_{133}	B(8)...B(10)	295.2(5)	8.2(tied to u_{67})	8.0	–0.3
u_{108}	C(6)...B(8)	297.0(6)	9.1(tied to u_{67})	8.8	–0.4
u_{110}	C(6)...B(10)	297.1(6)	9.1(tied to u_{67})	8.8	–0.3
u_{83}	B(4)...B(7)	302.7(3)	7.5(tied to u_{109})	8.2	0.1
u_{81}	B(4)...B(5)	302.8(3)	7.5(tied to u_{109})	8.2	0.2
u_{39}	B(1)...S(9)	306.1(3)	6.7(tied to u_{109})	7.3	–0.6
u_{68}	B(3)...S(9)	306.6(3)	6.7(tied to u_{109})	7.3	–0.2
u_{94}	B(4)...H(22)	306.9(8)	12.3(tied to u_{109})	13.5	0.7
u_{93}	B(4)...H(21)	307.1(8)	12.3(tied to u_{109})	13.5	0.9
u_{97}	B(5)...S(9)	324.4(3)	7.8(tied to u_{109})	8.5	–0.6
u_{121}	B(7)...S(9)	324.6(3)	7.8(tied to u_{109})	8.5	–0.4
u_{48}	B(1)...H(20)	329.5(10)	13.1(tied to u_{109})	14.3	–0.1
u_{78}	B(3)...H(20)	329.5(10)	13.1(tied to u_{109})	14.3	–0.1
u_{109}	C(6)...S(9)	339.6(11)	11.5(6)	12.6	–0.6
u_{96}	B(5)...B(8)	346.4(4)	7.4(tied to u_{109})	8.1	–0.4
u_{122}	B(7)...B(10)	346.5(4)	7.4(tied to u_{109})	8.1	–0.3
u_{107}	B(5)...H(22)	347.6(16)	13.7(tied to u_{109})	15.0	0.2
u_{132}	B(7)...H(21)	347.7(16)	13.7(tied to u_{109})	15.0	0.3
u_{143}	B(8)...H(21)	351.9(16)	14.2(tied to u_{109})	15.5	0.2
u_{165}	B(10)...H(22)	351.9(16)	14.2(tied to u_{109})	15.5	0.2
u_{82}	B(4)...C(6)	354.0(8)	9.8(tied to u_{53})	9.1	0.0
u_{92}	B(4)...H(20)	356.1(14)	19.9(tied to u_{53})	18.6	0.7
u_{50}	B(1)...H(22)	356.6(10)	13.9(tied to u_{53})	13.0	0.3
u_{79}	B(3)...H(21)	356.7(10)	13.9(tied to u_{53})	12.9	0.5

u_{53}	B(2)...S(9)	368.0(5)	8.9(5)	8.3	–0.4
u_{74}	B(3)...H(16)	372.0(7)	11.8(tied to u_{53})	11.0	–0.9
u_{44}	B(1)...H(16)	372.2(7)	11.8(tied to u_{53})	11.0	–0.7
u_{113}	C(6)...H(13)	386.2(6)	12.7(tied to u_{144})	11.4	–1.0
u_{111}	C(6)...H(11)	386.3(6)	12.7(tied to u_{144})	11.4	–0.9
u_{127}	B(7)...H(15)	393.4(7)	12.8(tied to u_{144})	11.5	–0.9
u_{103}	B(5)...H(17)	393.5(7)	12.8(tied to u_{144})	11.5	–0.9
u_{57}	B(2)...H(14)	393.6(6)	12.4(tied to u_{144})	11.1	–0.5
u_{73}	B(3)...H(15)	394.0(4)	13.0(tied to u_{144})	11.6	–0.8
u_{45}	B(1)...H(17)	394.2(4)	12.9(tied to u_{144})	11.6	–0.7
u_{62}	B(2)...H(19)	394.8(6)	12.6(tied to u_{144})	11.4	–0.8
u_{157}	B(10)...H(12)	394.8(4)	12.7(tied to u_{144})	11.4	–0.8
u_{61}	B(2)...H(18)	394.8(6)	12.6(tied to u_{144})	11.4	–0.7
u_{135}	B(8)...H(12)	394.9(4)	12.7(tied to u_{144})	11.4	–0.7
u_{139}	B(8)...H(16)	395.1(8)	13.1(tied to u_{144})	11.7	–1.3
u_{161}	B(10)...H(16)	395.1(8)	13.1(tied to u_{144})	11.8	–1.3
u_{85}	B(4)...H(12)	395.7(6)	12.3(tied to u_{144})	11.0	–0.5
u_{46}	B(1)...H(18)	396.5(5)	12.7(tied to u_{144})	11.4	–0.8
u_{77}	B(3)...H(19)	396.6(5)	12.7(tied to u_{144})	11.4	–0.6
u_{100}	B(5)...H(13)	396.8(4)	12.7(tied to u_{144})	11.4	–0.8
u_{123}	B(7)...H(11)	396.9(4)	12.7(tied to u_{144})	11.4	–0.7
u_{134}	B(8)...H(11)	397.6(3)	12.6(tied to u_{144})	11.3	–0.9
u_{158}	B(10)...H(13)	397.7(3)	12.6(tied to u_{144})	11.3	–0.7
u_{163}	B(10)...H(18)	400.0(8)	12.8(tied to u_{144})	11.5	–1.2
u_{141}	B(8)...H(19)	400.1(8)	12.8(tied to u_{144})	11.5	–1.1
u_{117}	C(6)...H(18)	405.3(9)	13.1(tied to u_{144})	11.8	–1.4
u_{118}	C(6)...H(19)	405.4(9)	13.1(tied to u_{144})	11.8	–1.4
u_{89}	B(4)...H(17)	405.6(5)	13.4(tied to u_{144})	12.0	–0.9
u_{87}	B(4)...H(15)	405.7(5)	13.4(tied to u_{144})	12.0	–0.8
u_{144}	S(9)...H(11)	408.2(5)	12.7(3)	11.5	–1.4
u_{146}	S(9)...H(13)	408.6(5)	12.7(tied to u_{144})	11.5	–1.0
u_{126}	B(7)...H(14)	409.0(4)	13.4(tied to u_{144})	12.1	–0.8
u_{101}	B(5)...H(14)	409.1(4)	13.4(tied to u_{144})	12.0	–0.7
u_{148}	S(9)...H(15)	432.6(6)	9.3(6)	11.7	–1.7
u_{150}	S(9)...H(17)	432.8(6)	9.4(tied to u_{148})	11.7	–1.5
u_{149}	S(9)...H(16)	444.3(14)	12.4(tied to u_{148})	15.5	–1.7

u_{88}	B(4)...H(16)	460.2(9)	12.4(tied to u_{145})	11.1	–1.1
u_{138}	B(8)...H(15)	464.6(4)	12.3(tied to u_{145})	11.0	–1.5
u_{162}	B(10)...H(17)	464.7(4)	12.3(tied to u_{145})	11.0	–1.4
u_{104}	B(5)...H(18)	465.1(4)	12.3(tied to u_{145})	11.0	–1.5
u_{130}	B(7)…H(19)	465.2(4)	12.3(tied to u_{145})	11.0	–1.4
u_{114}	C(6)...H(14)	472.3(8)	13.1(tied to u_{145})	11.7	–1.1
u_{145}	S(9)...H(12)	486.9(6)	12.5(8)	11.2	–1.4

Appendix 5

Supplementary data for the GED refinement of

Table A5.1 Least-squares correlation matrix.[a]

	p_8	p_{10}	p_{11}	p_{12}	p_{15}	p_{19}	p_{22}	p_{23}	p_{24}	u_8	u_{12}	u_{25}	u_{37}	k_2
p_1	–60	–78	–52			–78	–72			67	–50			
p_7				–53								–53		
p_8							57			–75			54	
p_{10}						66					56			
p_{11}				–55			68					–51		
p_{12}								–76				63		
p_{13}					67									
p_{15}														
p_{19}							50			–54				
p_{23}									–61			–53		
u_8														54
u_{62}														71

[a] All elements are scaled by a factor of 100, and only off-diagonal elements with values ≥ 50% are included. k_2 is the scale factor for the short nozzle-to-film distance.

Table A5.2 Interatomic distances (r_a), amplitudes of vibration (u_{h1}) and corrections (k_{h1}) (all values in pm).

	Atom pair	r_a	u_{h1}	k_{h1}	RHF/6-31G*
u_6	C(5)–F(6)	132.7(2)	4.5(tied to u_1)	0.1	4.1
u_7	C(5)–F(7)	133.0(2)	4.5(tied to u_1)	0.1	4.1
u_8	C(5)–F(8)	133.2(2)	4.5(tied to u_1)	0.1	4.1
u_9	C(9)–F(10)	133.3(2)	4.5(tied to u_1)	0.1	4.1
u_{11}	C(9)–F(12)	133.3(2)	4.5(tied to u_1)	0.1	4.1
u_{10}	C(9)–F(11)	133.5(2)	4.5(tied to u_1)	0.1	4.1
u_5	O(4)–C(5)	139.3(7)	4.9(tied to u_1)	0.1	4.5
u_1	S(1)–O(2)	141.6(3)	3.6(3)	0.1	3.3
u_2	S(1)–O(3)	142.0(3)	3.6(tied to u_1)	0.1	3.3
u_3	S(1)–O(4)	161.5(4)	4.4(3)	0.1	4.2
u_4	S(1)–C(9)	181.2(4)	5.2(4)	0.1	4.5

u_{55}	F(7)...F(8)	215.1(3)	4.4(2)	–0.1	5.1
u_{38}	O(4)...F(6)	215.1(8)	4.5(tied to u_{55})	–0.1	5.2
u_{49}	F(6)...F(7)	215.1(2)	4.4(tied to u_{55})	–0.1	5.1
u_{50}	F(6)...F(8)	215.3(2)	4.4(tied to u_{55})	–0.1	5.1
u_{65}	F(10)...F(12)	216.4(2)	4.5(tied to u_{55})	–0.1	5.1
u_{64}	F(10)...F(11)	216.6(2)	4.5(tied to u_{55})	–0.1	5.1
u_{66}	F(11)...F(12)	216.6(2)	4.5(tied to u_{55})	–0.1	5.1
u_{39}	O(4)...F(7)	228.3(4)	4.6(tied to u_{55})	–0.1	5.3
u_{40}	O(4)...F(8)	228.4(4)	4.6(tied to u_{55})	–0.1	5.3
u_{20}	O(2)...O(4)	242.3(8)	8.2(tied to u_{17})	0.0	6.0
u_{29}	O(3)...O(4)	248.5(6)	8.0(tied to u_{17})	0.0	5.9
u_{19}	O(2)...O(3)	250.9(12)	6.9(tied to u_{17})	–0.1	5.1
u_{41}	O(4)...C(9)	256.2(17)	10.4(tied to u_{17})	–0.2	7.7
u_{17}	S(1)...F(11)	257.2(7)	8.5(3)	–0.1	6.2
u_{18}	S(1)...F(12)	260.6(5)	8.2(tied to u_{17})	–0.1	6.0
u_{16}	S(1)...F(10)	260.6(5)	8.2(tied to u_{17})	–0.1	6.0
u_{25}	O(2)...C(9)	260.8(7)	9.2(tied to u_{17})	0.0	6.8
u_{33}	O(3)...F(8)	262.4(15)	22.8(tied to u_{17})	1.6	16.8
u_{12}	S(1)...C(5)	262.6(7)	7.4(tied to u_{17})	–0.2	5.5
u_{34}	O(3)...C(9)	263.1(7)	9.2(tied to u_{17})	–0.1	6.8
u_{42}	O(4)...F(10)	284.5(22)	19.5(tied to u_{17})	0.0	14.3
u_{30}	O(3)...C(5)	284.6(9)	9.8(tied to u_{15})	0.9	9.3
u_{44}	O(4)...F(12)	290.3(26)	20.1(tied to u_{17})	0.0	14.8
u_{26}	O(2)...F(10)	294.0(13)	12.6(tied to u_{15})	0.3	12.0
u_{37}	O(3)...F(12)	295.7(10)	12.8(tied to u_{15})	0.2	12.2
u_{15}	S(1)...F(8)	297.0(10)	10.8(6)	0.1	10.3
u_{27}	O(2)...F(11)	303.4(15)	13.8(tied to u_{15})	0.0	13.2
u_{36}	O(3)...F(11)	307.0(12)	13.9(tied to u_{15})	0.1	13.3
u_{14}	S(1)...F(7)	321.5(10)	11.7(tied to u_{15})	–0.2	11.2
u_{32}	O(3)...F(7)	322.7(21)	17.8(tied to u_{15})	1.6	17.0
u_{63}	F(8)...F(12)	328.1(37)	30.3(tied to u_{15})	3.3	28.9
u_{21}	O(2)...C(5)	357.0(10)	11.0(tied to u_{13})	–1.2	8.3
u_{48}	C(5)...F(12)	358.0(21)	19.4(tied to u_{15})	0.6	18.5
u_{45}	C(5)...C(9)	363.6(13)	14.7(tied to u_{13})	–0.8	11.1
u_{13}	S(1)...F(6)	367.4(7)	7.1(4)	–1.0	5.4
u_{60}	F(8)...C(9)	370.4(27)	28.9(tied to u_{13})	0.4	21.9
u_{28}	O(2)...F(12)	374.2(6)	8.2(tied to u_{13})	–1.0	6.2
u_{43}	O(4)...F(11)	374.8(14)	9.1(tied to u_{13})	–1.2	6.9
u_{35}	O(3)...F(10)	375.9(6)	8.2(tied to u_{13})	–1.0	6.2
u_{23}	O(2)...F(7)	384.0(22)	24.9(tied to u_{13})	–1.1	18.8
u_{46}	C(5)...F(10)	407.1(17)	24.9(tied to u_{13})	–1.8	18.8

u_{54}	F(6)...F(12)	409.0(29)	31.9(tied to u_{13})	–0.1	24.1
u_{31}	O(3)...F(6)	409.5(7)	4.8(tied to u_{52})	–0.2	8.8
u_{24}	O(2)...F(8)	421.2(7)	4.8(tied to u_{52})	–1.4	8.9
u_{51}	F(6)...C(9)	432.0(15)	7.4(tied to u_{52})	–1.5	13.7
u_{52}	F(6)...F(10)	444.7(20)	12.8(12)	–2.1	23.7
u_{61}	F(8)...F(10)	446.0(29)	15.4(tied to u_{52})	–1.6	28.6
u_{22}	O(2)...F(6)	450.8(11)	13.0(tied to u_{59})	–2.1	9.4
u_{56}	F(7)...C(9)	462.5(12)	15.0(tied to u_{59})	–1.7	10.9
u_{62}	F(8)...F(11)	473.3(26)	31.5(tied to u_{59})	–0.5	22.9
u_{59}	F(7)...F(12)	473.5(20)	25.6(29)	–1.0	18.6
u_{47}	C(5)...F(11)	479.9(11)	15.1(tied to u_{59})	–1.8	11.0
u_{57}	F(7)...F(10)	509.9(21)	19.7(tied to u_{59})	–3.0	14.4
u_{53}	F(6)...F(11)	558.9(14)	19.9(13)	–3.1	12.6
u_{58}	F(7)...F(11)	566.1(12)	21.3(tied to u_{53})	–2.2	13.4

Appendix 6

Supplementary data for the GED refinement of $CH_3SO_2SCH_3$

Table A6.1 Least-squares correlation matrix.[a]

	p_{10}	p_{12}	p_{17}	u_7	u_{29}	u_{57}	k_2
p_4				-52			
p_7	-70	-87				-52	
p_8			-51		53	77	
p_9		-63					
p_{10}		59					
p_{12}			-64				
p_{17}						-61	
u_{15}							82

[a] All elements are scaled by a factor of 100, and only off-diagonal elements with values ≥ 50% are included. k_2 is the scale factor for the short nozzle-to-film distance.

Table A6.2 Interatomic distances (r_a), amplitudes of vibration (u_{h1}) and perpendicular distance corrections (k_{h1}) (in units of pm).

	Atom pair	r_a	u_{h1} (GED)	u_{h1} (MP2/6-31G(d)	k_{h1}
u_9	C(8)–H(10)	108.6(3)	8.5(tied to u_1)	7.6	0.4
u_1	C(1)–H(2)	108.6(3)	8.4(3)	7.5	0.4
u_3	C(1)–H(4)	108.6(3)	8.4(tied to u_1)	7.5	0.4
u_2	C(1)–H(3)	108.6(3)	8.4(tied to u_1)	7.5	0.4
u_8	C(8)–H(9)	108.6(3)	8.5(tied to u_1)	7.6	0.4
u_{10}	C(8)–H(11)	108.6(3)	8.4(tied to u_1)	7.5	0.4
u_5	S(5)–O(6)	143.2(1)	4.3(1)	3.5	0.1
u_6	S(5)–O(7)	143.6(1)	4.3(tied to u_5)	3.6	0.1
u_{62}	H(9)...H(11)	175.8(9)	12.1(fixed)	12.1	–0.3
u_{61}	H(9)...H(10)	175.8(9)	12.2(fixed)	12.2	–0.2
u_{64}	H(10)...H(11)	175.9(9)	12.3(fixed)	12.3	–0.1
u_{20}	H(2)...H(4)	177.0(9)	12.2(fixed)	12.2	–0.1
u_{19}	H(2)...H(3)	177.0(9)	12.2(fixed)	12.2	–0.1
u_{29}	H(3)...H(4)	177.0(9)	12.1(fixed)	12.1	–0.1
u_4	C(1)–S(5)	178.4(3)	5.9(1)	4.9	0.1
u_{11}	C(8)–S(12)	182.1(3)	6.0(tied to u_4)	5.1	0.1

u_{7}	S(5)–S(12)	207.4(1)	6.3(1)	5.2	0.1
u_{21}	H(2)...S(5)	235.1(15)	10.4(tied to u_{50})	11.2	–0.3
u_{38}	H(4)...S(5)	238.2(9)	10.2(tied to u_{50})	11.0	–0.3
u_{30}	H(3)...S(5)	238.2(9)	10.2(tied to u_{50})	11.0	–0.3
u_{65}	H(10)...S(12)	239.5(15)	10.4(tied to u_{50})	11.3	0.1
u_{66}	H(11)...S(12)	243.3(9)	10.0(tied to u_{50})	10.8	–0.1
u_{63}	H(9)...S(12)	243.4(9)	9.9(tied to u_{50})	10.7	0.1
u_{50}	O(6)...O(7)	249.5(3)	5.3(3)	5.7	–0.1
u_{42}	H(4)...H(9)	261.0(70)	50.3(fixed)	50.3	13.2
u_{13}	C(1)...O(7)	262.1(5)	6.8(tied to u_{50})	7.4	0.0
u_{12}	C(1)...O(6)	263.1(5)	6.8(tied to u_{50})	7.4	0.0
u_{59}	O(7)...H(11)	269.1(48)	30.8(fixed)	30.8	12.1
u_{55}	O(6)...S(12)	278.8(4)	8.0(4)	8.2	0.0
u_{31}	H(3)...O(6)	282.1(18)	16.7(fixed)	16.7	0.2
u_{40}	H(4)...O(7)	285.5(18)	16.8(fixed)	16.8	0.2
u_{23}	H(2)...O(7)	287.0(24)	17.4(fixed)	17.4	–0.1
u_{60}	O(7)...S(12)	289.2(3)	7.1(tied to u_{55})	7.4	–0.1
u_{22}	H(2)...O(6)	293.7(23)	17.6(fixed)	17.6	–0.1
u_{46}	S(5)...C(8)	299.1(12)	8.7(tied to u_{55})	9.0	–0.2
u_{18}	C(1)...S(12)	301.7(12)	8.6(tied to u_{55})	8.9	–0.2
u_{49}	S(5)...H(11)	305.5(46)	26.5(fixed)	26.5	3.7
u_{56}	O(7)...C(8)	307.2(15)	16.1(tied to u_{55})	16.7	1.4
u_{45}	H(4)...S(12)	313.9(27)	19.8(fixed)	19.8	0.0
u_{37}	H(3)...S(12)	314.9(27)	19.4(fixed)	19.4	0.1
u_{41}	H(4)...C(8)	316.1(55)	33.3(fixed)	33.3	2.0
u_{47}	S(5)...H(9)	320.8(49)	33.4(fixed)	33.4	–0.4
u_{57}	O(7)...H(9)	325.4(81)	51.0(fixed)	51.0	–1.9
u_{15}	C(1)...H(9)	328.5(61)	41.9(fixed)	41.9	5.5
u_{44}	H(4)...H(11)	338.7(117)	59.6(fixed)	59.6	–1.7
u_{32}	H(3)...O(7)	352.0(8)	10.2(fixed)	10.2	–1.6
u_{39}	H(4)...O(6)	352.2(8)	10.2(fixed)	10.2	–1.6
u_{14}	C(1)...C(8)	358.0(40)	23.8(18)	22.6	–0.7
u_{34}	H(3)...H(9)	372.3(77)	44.8(fixed)	44.8	3.9
u_{17}	C(1)...H(11)	382.0(91)	46.4(fixed)	46.4	–2.1
u_{48}	S(5)...H(10)	391.5(15)	12.8(fixed)	12.8	–5.7
u_{28}	H(2)...S(12)	397.7(11)	10.9(fixed)	10.9	–2.0
u_{33}	H(3)...C(8)	400.6(54)	30.3(fixed)	30.3	–2.5
u_{58}	O(7)...H(10)	400.9(23)	21.7(fixed)	21.7	–5.8
u_{43}	H(4)...H(10)	405.2(50)	37.1(fixed)	37.1	–6.7
u_{25}	H(2)...H(9)	415.7(62)	46.8(fixed)	46.8	2.3
u_{51}	O(6)...C(8)	416.4(8)	9.9(6)	9.0	–1.9

u_{54}	O(6)...H(11)	427.6(28)	22.1(fixed)	22.1	1.8
u_{36}	H(3)...H(11)	446.3(86)	45.6(fixed)	45.6	–5.9
u_{24}	H(2)...C(8)	448.7(39)	23.6(fixed)	23.6	–2.6
u_{52}	O(6)...H(9)	450.5(40)	27.2(fixed)	27.2	–3.5
u_{16}	C(1)...H(10)	451.0(35)	24.5(fixed)	24.5	–8.1
u_{27}	H(2)...H(11)	457.7(95)	48.0(fixed)	48.0	–1.8
u_{35}	H(3)...H(10)	482.3(53)	33.2(fixed)	33.2	–8.2
u_{53}	O(6)...H(10)	497.6(15)	15.6(fixed)	15.6	–5.7
u_{26}	H(2)...H(10)	544.8(35)	24.9(fixed)	24.9	–11.0

Appendix 7

List of publications

1. Molecular structures of *arachno*-decaborane derivatives 6,9-$X_2B_8H_{10}$ (X = CH2, NH, Se) including a gas-phase electron-diffraction study of 6,9-$C_2B_8H_{14}$. D. Hynk, M. Bühl, J. Holub, S. A. Hayes, D. A. Wann, I. D. Mackie, K. B. Borisenko, H. E. Robertson and D. W. H. Rankin, *Inorg. Chem.* (2006), **45**, 6014.

2. Molecular structures of *arachno*-heteroboranes with decaborane frameworks: two C_s-symmetrical azacarba- and carbathiaboranes. D. Hynk, J. Holub, S. A. Hayes, M. F. Robinson, D. A. Wann, H. E. Robertson and D. W. H. Rankin, *Inorg. Chem.* (2006), **45**, 8442.

3. Gas-phase structure and vibrational properties of trifluoromethyl trifluoromethanesulfonate, $CF_3SO_2OCF_3$. M. E. Tuttolomondo, P. E. Arganaraz, E. L. Varetti, S. A. Hayes, D. A. Wann, H. E. Robertson, D. W. H. Rankin and A. Ben Altabef. *Eur. J. Inorg. Chem.* (2007), 1381.

4. Gas-phase structure, rotational barrier and vibrational properties of methyl methanethiosulfonate, $CH_3SO_2OCH_3$: an experimental and computational study. M. E. Tuttolomondo, A. Navarro, T. P. Ruiz, E. Varetti, S. A. Hayes, D. A. Wann, H. E. Robertson, D. W. H. Rankin and A. Ben Altabef. *J. Phys. Chem. A* (2007), **111**, 9952.